Development of a Diamond-based Scanning Probe Spin Sensor Operating at Low Temperature in Ultra High Vacuum

Von der Fakultät 8 Mathematik und Physik der Universität Stuttgart
zur Erlangung der Würde eines Doktors der Naturwissenschaften
(Dr. rer. nat.) genehmigte Abhandlung

Vorgelegt von

Eike Oliver Schäfer-Nolte

aus Bielefeld

Hauptberichter: Prof. Dr. J. Wrachtrup
Mitberichter: Prof. Dr. K. Kern

Tag der mündlichen Prüfung: 28.05.2014

3. Physikalisches Institut der Universität Stuttgart

2014

Contents

Summary

This thesis describes the development of a scanning probe microscope for the detection of single spins with nanoscale spatial resolution. The central element of this instrument is the nitrogen-vacancy (NV-) center in diamond, a color center that can be employed as a highly-precise magnetic field sensor [1]. Using this center as an atomic-size scanning probe enables imaging of weak magnetic fields on the nanoscale [2, 3]. The sensitivity of the NV center is sufficient to detect individual electron and even nuclear spins via magnetic dipolar interactions. The quantum mechanical spin state of these target spins can be manipulated by resonant radio frequency or microwave pulses and subsequently read out via the NV center, which facilitates electron spin resonance (ESR) and nuclear magnetic resonance (NMR) spectroscopy on the single molecule level [4, 5].

These spin resonance techniques are a widely used analytical tool in physics, chemistry, and medicine [6, 7]. Due to the sensitivity of common induction-based detectors, conventional instruments are limited to measurements on molecular ensembles, where typical sensitivities correspond to $10^{14} - 10^{16}$ detectable nuclear spins or $10^{12} - 10^{14}$ electron spins. For the same reason also the achievable spatial resolution in magnetic resonance imaging is typically limited to 1 mm^3. A technique for single spin detection would expand the applicability of these methods and facilitate unprecedented experiments with single molecules. Examples might be the three dimensional tomography of single proteins for structure determination or the observation of molecular dynamics during chemical reactions.

The NV center as a magnetic field sensor

Magnetometry utilizing the NV center has attracted much attention in recent years since it bears the potential for detecting hitherto inaccessible magnetic signals at the nanoscale. The unique physical properties facilitating this application have been investigated by various groups [8, 9]; the color center consists of a substitutional nitrogen atom and an adjacent vacancy in the diamond lattice formed by carbon atoms. In the negatively charged state, which is the relevant state for magnetometry applications, the

optical ground state is a spin triplet ($S = 1$) with a zero-field splitting of 2.87 GHz between the $m_S = 0$ and $m_S = \pm 1$ levels. Transitions between the spin states can be induced by resonant microwave fields. Optical pumping with green light transfers the system to an excited state that decays via photon emission with a wavelength of 650 - 750 nm. The observed fluorescence intensity depends on the spin state of the NV center; for the $m_S = \pm 1$ states, there is an increased probability to decay via a competing non-radiative relaxation channel involving a metastable singlet state, therefore the fluorescence intensity of the ± 1 manifold is decreased by roughly 30 % compared to the $m_S = 0$ subsystem. Moreover, this additional decay channel effectively transfers population into the $m_S = 0$ state, resulting in an efficient spin polarization by optical cycling. These two effects enable optically detected magnetic resonance (ODMR) measurements on single NV centers.

In an external magnetic field, arising for example from nearby spins, there is a Zeeman shift of the spin states in the optical ground state. This can be observed by appropriate ODMR protocols and therewith the local magnetic field can be determined. Due to the long spin coherence time of the NV center (up to several milliseconds in high purity diamond) such measurements can be carried out with a very high precision by applying quantum-metrological sensing techniques. Besides the extraordinary sensitivity and the high spatial resolution, another advantage of NV magnetometry is the wide frequency range over which time dependent magnetic fields can be detected. Depending on the utilized ODMR protocol the spectral sensitivity can be varied from the GHz range down to below 1 Hz, which enables the use of the NV center as a quantum spectrometer for fluctuating magnetic fields.

Previous demonstrations and aim of the new instrument

The predicted potential of NV magnetic sensing has spawned great efforts towards the realization of single spin spectroscopy. Working towards this goal, the detection of metal-organic compounds [10, 11], organic radicals [12, 13], and proton spins in organic molecules [14, 15] has been demonstrated. These first steps relied on the detection of spin ensembles without capitalizing on the potentially very high spatial resolution of the sensing technique. This can be exploited by the integration of the NV sensor into a scanning probe architecture, which has been demonstrated in several proof-of-principle experiments [16–18]. All previous realizations of molecular sensing and scanning probe magnetometry have been performed under ambient conditions. The instrument developed in this thesis enables such experiments for the first time at low temperatures down to 5 K and in an ultra-high vacuum (UHV) environment with a base pressure on the

order of $\sim 10^{-10}$ mbar.

Measurements under these conditions are technically very challenging, but enable extremely sensitive measurements on precisely controlled sample systems. Low temperature measurements are beneficial since spin lifetimes of potential targets are often increased by orders of magnitude compared to room temperature, enabling the application of sophisticated sensing protocols. Furthermore, scanning probe microscopes operating at low temperatures typically feature enhanced spatial resolution and stability due to reduced thermal drift and suppressed molecular motion. UHV conditions, on the other hand, facilitate a clean and controllable sample preparation that enables investigations of isolated molecules without detrimental effects from contaminations. Thus, operation in a cryogenic UHV environment is not only expected to boost the sensitivity and resolution of the NV scanning probe magnetometer, but it will also extend its applicability to a variety of molecular systems that cannot be studied under ambient conditions.

Assembly of the NV scanning probe magnetometer

The instrument developed for this purpose consists of a combined atomic force (AFM) and confocal microscope (CFM) mounted in an UHV system with a liquid helium cryostat. The central element is the microscope head containing the sample, the AFM scanner, the CFM front lens, high frequency waveguides and the required nanopositioners. It is situated in vacuum and mounted to the cold plate of a liquid helium reservoir. Apart from the front lens, all optical elements of the confocal microscope are situated outside the vacuum setup to facilitate simple alignment. To avoid transmission losses and autofluorescence related to the use of optical fibers, we realized a free-beam access to the microscope head via high-quality viewports in the vacuum chamber and the cryostat radiation shields. Pulsed high frequency fields for spin manipulation are generated by radio frequency and microwave sources and guided to the sample via impedance matched transmission lines in the vacuum setup.

Crucial for the sensitivity of the NV magnetometer is the signal quality of the detected NV fluorescence. To achieve a high photon count rate with maximum spin contrast, an optical access with high numeric aperture and efficient aberration correction is required, which is especially challenging at low temperature. Other criteria which had to be considered in the instrument design are the mechanical stability, which is crucial for scanning probe microscopy with sub-nanometer resolution, and the achieved cooling power, since sample heating by laser and high frequency excitation had to be minimized. For an efficient use also a reliable mechanism for sample and tip exchange without breaking the vacuum or warming up the system is important.

The instrument developed in consideration of these criteria was extensively tested to characterize and optimize its performance. To this end various ODMR measurements on single NV centers at low temperature were carried out, verifying the performance of the optical and microwave setup. The atomic force microscope was benchmarked by imaging atomic steps on a gold surface at low temperature. By combination of both techniques, also imaging of magnetic fields on the nanoscale could be demonstrated. To access the sample temperature in the optical focus and quantify heating effects of the laser and high frequency irradiation, we utilized a novel method for determining the temperature based on optical spectroscopy. These measurements indicate a negligible effect from laser irradiation, but considerable heating when applying strong microwave excitation.

Probing the spin dynamics of ferritin proteins

As a first application of the NV scanning probe magnetometer to study molecular systems we investigated the temperature dependent magnetization dynamics of ferritin proteins. These biomolecules possess a mineral core with a magnetic moment of approximately 100 - 300 μ_B, which fluctuates thermally activated between two preferential orientations [19, 20]. The characteristic frequency of these fluctuations varies by orders of magnitude between room temperature and 5 K, such that for the detection of these dynamics at different temperatures different experimental techniques are commonly employed. Widely used for ferritin studies at low temperature are SQUID-magnetometry, Mößbauer spectroscopy and ESR spectroscopy [20–22]. These techniques can detect the ferritin spin dynamics only in a limited frequency range and are restricted by their sensitivity to ensemble measurements. We demonstrate that by utilizing appropriate ODMR protocols the detection bandwidth of NV magnetometry can be tuned to cover a wide frequency range of magnetic field fluctuations. Moreover, the sensitivity is sufficient to detect signals from individual ferritin molecules. By these measurements the anisotropy barriers of the core can be determined, which were on the order of 25 meV for the investigated ferritin sample.

Outlook

The demonstrated performance and sensitivity of the system should enable the detection of single electron spins via double resonance techniques. Currently various paramagnetic molecular species are explored as potential target systems, where especially the photostability is an important criterion. By further optimizing the measurement setup, particularly regarding the optical read out of the NV spin and the sample preparation,

the sensitivity should be considerably enhanced, such that in future even nuclear spin system could be investigated. This would greatly extend the applicability of this technique, since most molecules host spin-bearing nuclei and their photostability is generally of less concern.

Zusammenfassung

In dieser Arbeit wird die Entwicklung eines Rastersondenmikroskops zur Detektion einzelner Spins mit einer Ortsauflösung auf der Nanometer-Skala beschrieben. Zentrales Element dieses Instruments ist das NV-Zentrum in Diamant, ein Kristalldefekt der als atomar kleiner, hochempfindlicher Magnetfeld-Sensor genutzt werden kann [1]. Wird dieser Sensor mit Hilfe eines Rasterkraft-Mikroskops in einigen Nanometern Abstand über eine Probe bewegt, können lokale Magnetfelder mit sehr hoher Genauigkeit abgebildet werden [2, 3]. Die Empfindlichkeit des NV-Zentrums ist dabei hoch genug, um einzelne Elektronen- oder sogar Kernspins in der Probe über magnetische Dipol-Wechselwirkungen zu detektieren. Der quantenmechanische Zustand dieser Spins kann durch resonante Radiofrequenz- oder Mikrowellenpulse manipuliert und anschließend über das NV-Zentrum ausgelesen werden, wodurch Elektronenspinresonanz (ESR)- und Kernspinresonanz (NMR)- Spektroskopie an einzelnen Molekülen möglich wird [4, 5].

Diese Spinresonanz-Methoden stellen heutzutage ein unverzichtbares Analyseverfahren in Physik, Chemie und Medizin dar [6, 7]. Durch die Empfindlichkeit der meist Induktions-basierten Detektoren sind konventionelle Instrumente auf Messungen an großen Spin-Ensembles limitiert, wobei typische Empfindlichkeiten bei $10^{14} - 10^{16}$ detektierbaren Kernspins bzw. $10^{12} - 10^{14}$ Elektronenspins liegen. Dadurch wird auch die erreichbare Ortsauflösung in der Kernspinresonanztomographie auf typischerweise 1 mm^3 begrenzt. Ein Verfahren zur Einzelspin-Detektion würde die Anwendungsmöglichkeiten dieser Methoden deutlich erweitern und bisher unmögliche Experimente an einzelnen Molekülen erlauben. Beispielhaft seien hier die dreidimensionale Tomographie von einzelnen Proteinen zur Strukturaufklärung oder die Beobachtung molekularer Dynamik während chemischer Reaktionen genannt.

Das NV-Zentrum als Magnetfeld-Sensor

Magnetometrie basierend auf dem NV-Zentrum stellt einen neuartigen Ansatz dar, um bisher unmessbar schwache magnetische Signale auf der Nanometer-Skala zu detektieren. Dazu wird die einzigartige Kombination physikalischer Eigenschaften dieses Kristallde-

fekts ausgenutzt, die in den letzten Jahren von verschieden Gruppen intensiv untersucht worden sind [8, 9]. Das NV-Zentrum besteht aus einem substitutionellen Stickstoffatom und einer benachbarten Fehlstelle im von Kohlenstoffatomen gebildeten Kristallgitter von Diamant. Im für Magnetometrie-Anwendungen relevanten, negativ geladenen Zustand wird der optische Grundzustand von einem Spin-Triplett (S=1) gebildet, das eine Nullfeld-Aufspaltung zwischen den $m_S = 0$ und $m_S = \pm 1$ Niveaus von 2.87 GHz besitzt. Übergänge zwischen den Spin-Niveaus können durch resonante Mikrowellen-Felder angeregt werden. Durch optisches Pumpen mit grünem Licht kann ein Übergang in einen angeregten Zustand induziert werden, der unter Lichtemission im Bereich von 650 - 750 nm relaxiert. Die beobachtbare Fluoreszenz-Intensität für ein einzelnes NV-Zentrum hängt dabei vom Spinzustand ab; durch einen zusätzlichen, nicht-strahlenden Relaxations-Mechanismus über Singulett-Zustände ist die Intensität für ein im $m_S = \pm 1$ Zustand polarisiertes NV-Zentrum ungefähr 30% niedriger als im $m_S = 0$ Zustand. Da dieser zweite Relaxations-Kanal das NV-Zentrum außerdem mit hoher Wahrscheinlichkeit in den $m_S = 0$ Zustand überführt, kann durch optisches Pumpen eine sehr hohe Spinpolarisation erreicht werden. Diese Kombination aus optischem Auslesen und Polarisieren des Spin-Zustandes ermöglicht optisch-detektierte Magnetresonanz (ODMR) Messungen an einzelnen NV-Zentren durch geeignete Sequenzen von Mikrowellen- und Laseranregung.

Befindet sich das NV-Zentrum in einem Magnetfeld, beispielsweise erzeugt durch benachbarte Spins, ändert sich durch den Zeeman-Effekt die Energieaufspaltung der Spin-Niveaus im optischen Grundzustand. Dies kann durch geeignete ODMR-Protokolle beobachtet und damit das lokale Magnetfeld bestimmt werden. Durch die sehr langen Kohärenzzeiten des NV-Spins (einige Millisekunden in hochreinen Proben) können diese lokalen Magnetfelder mittels quanten-metrologischer Messmethoden äußerst präzise bestimmt werden. Neben der außerordentlichen Empfindlichkeit und der hohen Ortsauflösung ist eine weitere Stärke der NV-basierten Magnetometrie der weite Frequenzbereich über den zeitabhängige Magnetfelder detektiert werden können. Je nach ODMR-Protokoll kann die spektrale Empfindlichkeit vom GHz-Bereich bis zu einigen Hz variiert werden, wodurch das NV-Zentrum als Quanten-Spektrometer für fluktuierende Magnetfelder genutzt werden kann.

Bisherige Realisierungen und Ziel des neuen Instruments

Das Potential des NV-Zentrums als Magnetfeld-Sensor hat vielfältige Anstrengungen zur Realisierung von Einzelspin-Spektroskopie ausgelöst. Dabei wurde unter anderem die Detektion von paramagnetischen metall-organischen Verbindungen [10, 11], organi-

scher Radikale [12, 13] und Protonen-Spins in organischen Molekülen [14, 15] demonstriert. Diese ersten Schritte basierten auf der Detektion von Spin-Ensembles ohne die potentiell sehr hohe Ortsauflösung des NV-Zentrums auszunutzen. Dies kann durch die Integration des NV-Sensors in ein Rastersondenmikroskop erreicht werden, wie es ebenfalls von verschiedenen Gruppen bereits prinzipiell demonstriert wurde [16–18]. Alle bisherigen Realisierungen sowohl von Molekül-Detektion als auch von ortsaufgelöster Rastersonden-Magnetometrie wurden bei Raumtemperatur unter Normaldruck durchgeführt. Das in dieser Arbeit entwickelte Instruments ermöglicht solche Messungen erstmals bei tiefen Temperaturen (~ 5 K) und im Ultrahoch-Vakuum (UHV, $\sim 10^{-10}$ mbar).

Experimente unter solchen extremen Bedingungen bedeuten zwar einen großen technischen Aufwand, erlauben aber auch äußerst präzise Messungen an genau kontrollierbaren Probensystemen. Tiefe Temperaturen bieten den großen Vorteil von typischerweise stark verlängerten Spin-Lebensdauern [23], was die Voraussetzung für die Anwendbarkeit vieler ODMR-Protokolle und für eine hohe Messgenauigkeit darstellt. Darüber hinaus erreicht Rastersonden-Mikroskopie an Molekülen bei tiefen Temperaturen typischerweise eine deutlich höhere Ortsauflösung und Stabilität, da thermischer Drift und die Eigenbewegung der Moleküle deutlich reduziert sind. Experimente im Ultrahoch-Vakuum wiederum profitieren von der Möglichkeit der extrem sauberen und kontrollierten Probenpräparation, was Messungen an einzelnen Molekülen ohne den Einfluss von Kontaminationen erlaubt. Durch diese Vorteile sollte nicht nur die erreichbare Messgenauigkeit der NV-Rastersonden-Magnetometrie deutlich gesteigert werden, sondern auch die Anwendbarkeit auf eine Vielzahl von molekularen Systemen erweitert werden.

Aufbau des NV-Rastersonden-Magnetometer

Das zu diesem Zweck entwickelte Instrument besteht aus einem kombiniertem Rasterkraft- (atomic force microscope, AFM) und optischen Konfokalmikroskop (confocal microscope, CFM), integriert in ein UHV-System mit Helium-Kryostaten. Die zentrale Baugruppe ist der Mikroskop-Kopf, der die Probe, die AFM-Spitze mit dem zugehörigen Scanner, die CFM-Frontlinse, Hochfrequenz-Wellenleiter und die benötigten Nanopositionierer enthält. Er befindet sich im Vakuum und ist an der Bodenplatte eines Flüssig-Helium Reservoirs montiert. Bis auf die Frontlinse befinden sich die optischen Elemente des Konfokalmikroskops außerhalb der Vakuumanlage, um eine einfache Justage zu gewährleisten. Zur Vermeidung von störenden Einflüssen von Glasfasern (Verluste und Eigenfluoreszenz) wurde ein optischer Freistrahl-Zugang zum Mikroskop-Kopf durch vergütete Fenster in der Vakuumkammer und den Kryostat-Strahlungsschilden realisiert. Eine Hochfrequenz-Pulselektronik generiert die zur Spin-Manipulation benötigten

Mikrowellen- und Radiofrequenz-Felder, die über Impedanz-angepasste Zuleitungen in die Vakuumanlage eingekoppelt und bis zur Probe geführt werden.

Entscheidend für die Empfindlichkeit des NV-Magnetometers ist die Signalqualität der detektierten NV Fluoreszenz. Um eine hohe Photonen-Zählrate mit maximalem Spin-Kontrast zu erhalten, ist ein optischer Zugang mit hoher numerischer Apertur und guter Aberrationskorrektur erforderlich, was besonders bei tiefer Temperatur eine Herausforderung darstellt. Weitere wichtige Kriterien für die Entwicklung des Instruments sind die mechanische Stabilität, die für Rasterkraftmikroskopie mit sub-Nanometer Auflösung entscheidend ist, und die erreichte Kühlleistung, um ein Aufheizen der Probe besonders durch Laser- und Hochfrequenz-Anregung zu vermeiden. Für eine effiziente Nutzung des Systems ist außerdem ein zuverlässiger Mechanismus für den Proben- und Spitzenwechsel ausschlaggebend, der ohne Belüftung der Vakuumanlage oder Aufwärmen des Systems durchgeführt werden kann.

Das unter diesen Gesichtspunkten entwickelte Prototyp-System wurde verschiedenen Tests unterzogen, um die Leistungsfähigkeit sowohl der einzelnen Komponenten als auch des Gesamtsystems zu charakterisieren und zu optimieren. Dazu wurden verschiedene ODMR-Messungen an einzelnen NV-Zentren bei tiefer Temperatur durchgeführt, sowie die topographische Abbildung atomarer Stufenkanten einer Goldoberfläche mittels Rasterkraftmikroskopie demonstriert. Durch die Kombination beider Techniken konnte außerdem die Abbildung von magnetischen Feldern auf der Nanometer-Skala gezeigt werden. Messungen der Probentemperatur durch optische Spektroskopie ergaben, das Heizeffekte durch die Laseranregung vernachlässigbar sind, während starke Mikrowelleneinstrahlung zu einem deutlichen Temperaturanstieg führen kann.

Untersuchung der Spin Dynamik von Ferritin Proteinen

Als erste Anwendung des NV-Rastersonden-Magnetometers zur Charakterisierung molekularer Spin-Systeme wird die temperaturabhängige Magnetisierungsdynamik von Ferritin Proteinen untersucht. Diese Biomoleküle besitzen einen mineralischen Kern mit einem magnetischen Moment von etwa 100 - 300 μ_B, das thermisch aktiviert zwischen zwei Vorzugs-Orientierungen fluktuiert [19, 20]. Die charakteristische Frequenz dieser Fluktuationen ändert sich um mehrere Größenordnung zwischen Raumtemperatur und 5 K, so dass üblicherweise je nach Temperaturbereich verschiedene experimentelle Techniken herangezogen werden um diese Dynamik zu detektieren. Häufig benutzt werden SQUID-Magnetometrie, Mößbauer-Spektroskopie und ESR-Spektroskopie [20–22]. Diese Methoden können die Ferritin Spin-Dynamik nur in einem begrenzten Frequenzbereich detektieren und sind außerdem durch ihre Empfindlichkeit limitiert auf Messungen an

molekularen Ensembles. Wir demonstrieren, dass mittels geeigneter ODMR-Protokolle die Detektionsbandbreite der NV-Magnetometrie so gewählt werden kann, dass ein weiter Frequenzbereich abgedeckt werden kann. Zudem ist die Empfindlichkeit hoch genug, um Signale von einzelnen Ferritin Molekülen zu detektieren. Damit können dann unter anderem die Anisotropie-Barrieren der Ferritin-Kerne bestimmt werden, die für die untersuchte Probe in der Größenordnung von 25 meV liegen.

Ausblick

Die bisher demonstrierte Leistungsfähigkeit und Empfindlichkeit des Systems sollte bereits die Detektion einzelner Elektronenspins über Doppelresonanzverfahren ermöglichen. Derzeitig werden verschiedene Molekül-Spezies auf ihre Eignung für derartige Experimente untersucht, wobei besonders die Photostabilität ein wichtiges Kriterium darstellt. Durch weitere instrumentelle Verbesserungen, insbesondere in Bezug auf das optische Auslesen des NV-Spins und die Probenpräparation, sollte die Empfindlichkeit noch deutlich gesteigert werden können, so dass mittelfristig auch Kernspin-Systeme untersucht werden können. Dies würde die Anwendbarkeit noch einmal deutlich erweitern, da detektierbare Kernspins in den meisten Molekülen vorkommen und auch deren Photostabilität deutlich unkritischer ist.

Chapter 1

Introduction

Investigating magnetism and spins at the nano- and atomic scale is a key challenge for understanding fundamental physical properties of matter as well as for applications in various fields ranging from electronic data processing over chemical analysis to medical diagnostics.

In the field of information technology, nanoscale magnetism plays an important role in present-day data storage devices where the magnetic bit size is approaching 10 nm. Moreover, the electron spin degree of freedom is employed in the emerging field of spintronics for novel device functionalities with the potential advantages of non-volatility, increased data processing speed, decreased power consumption and higher integration densities [24–26]. By exploiting the quantum properties of spins, also quantum computers based on spin qbits might be realized in the future [27, 28]. For the development of these technologies, the capability for sensitive spin detection with high spatial resolution is crucial.

Spin resonance techniques are widely use as analytical tools in chemistry as they can provide unique information on molecular properties. Since the resonance signal for a given (electron or nuclear) spin species depends sensitively on the configuration of nearby spins and the surrounding electronic orbitals, structural properties like bonding types and distances between atoms can be probed alongside vibrational or rotational dynamics [6,7]. Although these techniques yield information on atomic length scales, the measurement relies on bulk samples containing large numbers of the probed molecules (typically 10^{15} for nuclear magnetic resonance, 10^{12} for electron spin resonance) due to the limited sensitivity of common induction-based detectors. Thus, only ensemble-averaged data on molecular properties can be obtained in this way. Extending the spin resonance spectroscopy to magnetic resonance tomography by the application of strong magnetic field gradients enables three dimensional imaging of spin densities, which is

extensively used in medical diagnostics to visualize internal structures of the body. Due to the low detector sensitivity the spatial resolution is limited to a voxel size on the order of 10 μm^3 in optimized setups [29](1 mm^3 for common clinical MRI machines). Introducing new techniques for nanoscale spin detection in the field of magnetic resonance spectroscopy and imaging will increase their sensitivity and spatial resolution and enable unprecedented experiments. For example, it might enable the observation of single molecule dynamics like protein folding or the action of catalysts in chemical reactions, or magnetic resonance imaging of single cells.

A variety of techniques for magnetic field sensing at the micro- and nanoscale has been developed over the last decades [30]. A good figure of merit for such sensors is the magnetic moment sensitivity, which is in essence the smallest number of spins it can detect [31]. Since the magnetic dipole field of a spin drops off with $1/r^3$, a spin sensor must be small and has to be brought very close to the sample. Figure 1.1 compares the magnetic field sensitivity and typical sensor-sample distances for different detector types. The diagonal lines represent a constant value of magnetic moment sensitivity.

Micro-fabricated Hall-sensors mounted to scanning systems have demonstrated sensitivities down to $10^{-9}\,\mathrm{T}/\sqrt{\mathrm{Hz}}$. Since the sensor-sample distance is in the μm-range, this corresponds to a magnetic moment sensitivity above 10^3 electron spins. In general, scaling down the active area of a Hall-sensor decreases its magnetic field sensitivity [32], such that further improvements of this technique in terms of magnetic moment sensitivity are difficult.

Superconducting quantum interference devices (SQUIDs) based on the Josephson-effect provide extremely high magnetic field sensitivities on the order of $10^{-15}\,\mathrm{T}/\sqrt{\mathrm{Hz}}$ [44] and much effort has been spent on integrating the sensor into scanning devices for nanoscale magnetometry [33–36]. However, most devices are based on planar technology and the corresponding large in-plane size makes it difficult to bring the sensor in sufficient proximity to the sample. Additionally, the required miniaturization of the devices reduces the field sensitivity [45]. However, scanning SQUID microscopy with single electron spin sensitivity around 0.6 $\mu_B/\sqrt{\mathrm{Hz}}$ has recently been demonstrated [37].

Magnetic resonance force microscopy (MRFM), based on the mechanical detection of the force between the target spins and a magnetic tip on an ultra-soft cantilever, has demonstrated the detection of a single electron spin [39] and small ensembles (on the order of 10^2) of proton spins in biological samples with ∼10 nm spatial resolution [46]. However, this technique requires very low temperatures (∼300 mK) and a tedious fabrication of optimized cantilevers and magnetic tips, which will make further progress in sensitivity very challenging.

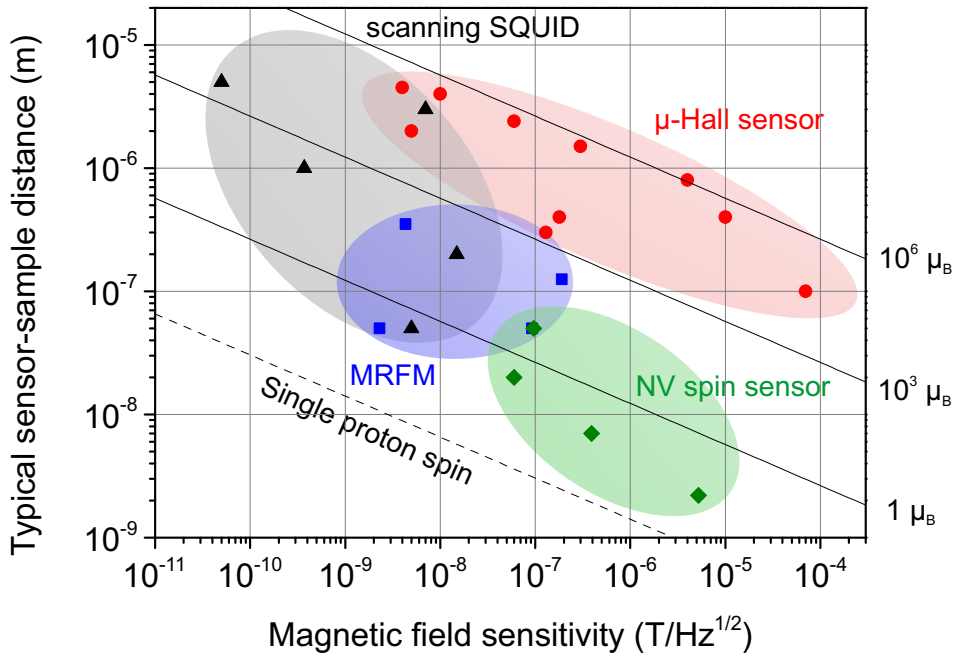

Figure 1.1: Comparison of different magnetic field sensing techniques developed for micro- and nanoscale magnetometry (adapted from reference [31]). The data points represent experimentally demonstrated magnetic field sensitivities for μ-Hall sensors [32], scanning SQUID sensors [33–37], magnetic resonance force microscopy [38–41] and NV spin sensors [14, 15, 42, 43] as a function of sensor-sample distance. The key for nanoscale spin sensing is the combination of short sensor-sample separations with high magnetic field sensitivity, thus the best magnetic moment sensitivity correspond to the the lower left region of the graph. Diagonal lines indicate the threshold for the detection of 10^6, 10^3, or 1 electron spin (dipole moment $\sim 1\mu_B$) or of a single proton spin within 1s.

A relatively new class of spin sensors that has attracted much attention within the last years are nitrogen-vacancy (NV) centers in diamond. These color centers feature spin-dependent fluorescence and narrow linewidths of the spin transitions which enables a precise determination of the local magnetic field via optically detected magnetic resonance (ODMR) on an individual NV center [1, 31]. By monitoring changes in the longitudinal relaxation process or the coherence properties of the NV spin in response to extrinsic target spins in its immediate environment, individual spins in nanoscale detection volumes can be probed. Recent proof-of-principle experiments employing such NV sensor spins close to the diamond surface demonstrated the detection of ensembles of molecular electron spins [12, 13] and nuclear spins [14, 15]. As can be seen in figure 1.1,

the NV centers provide in comparison to the above mentioned techniques the highest magnetic moment sensitivity due to the atomic size of the sensor and correspondingly a short achievable sensor-sample separation. The minimum distance is given by the distance of the NV center to the diamond surface, which can be below 5 nm.

To make full use of the atomic size and high sensitivity of the NV sensor it can be integrated into a scanning probe architecture. In this work the development of an atomic force microscope (AFM) combined with an ODMR-setup for NV-magnetometry on the nanoscale is described. The underlying concept is shown in figure 1.2: the NV center is placed at the tip apex of an AFM and scanned over the sample surface, its spin state is read out by recording its fluorescence under optical excitation. By positioning the NV probe close to target spins on the sample, a controlled coupling can be realized. The application of radio frequency (RF) fields enables coherent manipulation of the NV and target spins and therewith the use of sophisticated detection schemes developed for spin resonance spectroscopy. The NV center scanning probe can be realized either by grafting a diamond nanocrystal containing a NV center to a standard AFM tip [16, 17, 47, 48], or by employing diamond nanopillars fabricated by e-beam lithography as scanning tip [43, 49]. Alternatively, the NV sensor spin can be situated in a bulk diamond serving as sample, while the molecule containing the target spin is attached to the tip.

The predicted potential for single spin sensing on molecular length scales has spawned great efforts towards developing NV center based scanning probe spin microscopes [16, 17, 49]. However, all previous experimental demonstrations have been performed under ambient conditions. The unique feature of the instrument developed in this work is the capability for experiments at low temperature (∼5 K) and in ultra high vacuum (UHV, $p < 10^{-9}$ mbar). Measurements under these conditions are technically very challenging, but offer a number of important advantages: UHV enables the study of individual molecules in a well-controlled environment without contaminations. Low temperature measurements are beneficial since molecular electron spin lifetimes are typically increased by orders of magnitude compared to room temperature [23, 50, 51], enabling the application of sophisticated EPR-protocols. Thus, the operation of a NV-based scanning probe spin microscope in a cryogenic UHV environment is expected to extend its applicability to a variety of molecular systems that cannot be studied in existing setups under ambient conditions. Additionally, scanning probe microscopes operating at low temperatures have demonstrated superior long-term stability due to reduced thermal drifts [52], enabling a higher spatial resolution and longer data acquisition times resulting an enhanced sensitivity.

This thesis summarizes our efforts to develop a low temperature UHV setup for

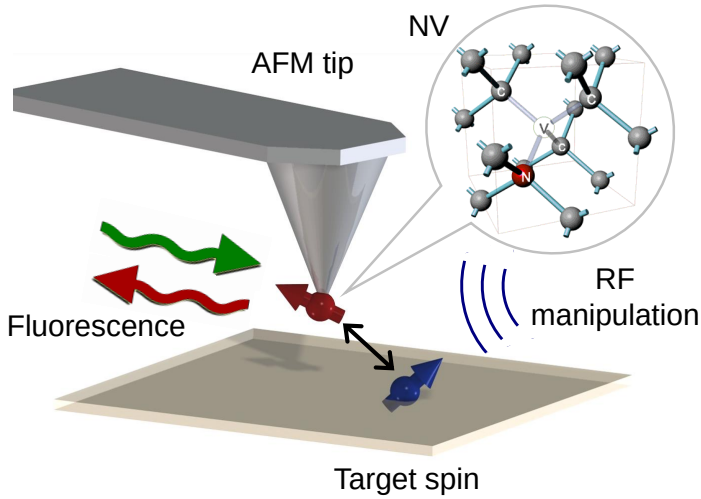

Figure 1.2: Scheme of a scanning probe spin sensor based on the NV center in diamond. The NV probe spin is scanned over the sample with the AFM tip and can be coupled to a target spin. The spin-state readout of the NV center is achieved via its fluorescence, while radio frequency pulses enable coherent control of NV and target spin.

highly precise magnetic resonance imaging and spectroscopy on the nanoscale. Chapter 2 recaps the physical properties of the NV center, the basics of optically detected magnetic resonance techniques and methods for NV-based magnetometry and spin sensing. In chapter 3 the design of the experimental apparatus consisting of the microscope head, optical setup, high frequency facilities, the cryostat and the vacuum system is presented. The performance of the individual sub-systems is verified by benchmark measurements discussed in chapter 4. Here we also present the first demonstration of NV-based magnetic resonance imaging of nanoscale magnetic fields at low temperature. In chapter 5 we apply NV magnetic sensing to investigate the magnetization dynamics of ferritin proteins at various temperatures. By tracking the temperature dependent spin relaxation processes of these molecules over a wide frequency range, we demonstrate that NV magnetometry outperforms established techniques in terms of sensitivity and detection bandwidth. The thesis concludes by outlining prospects for further improvements of the instruments performance and future experiments.

Chapter 2

NV-based Magnetometry and Spin Sensing

The NV center in diamond has attracted an increasing amount of attention within the last years due to its unique properties, including optical spin polarization, optical spin read out, and long spin coherence time. These properties make it a promising candidate for applications like solid-state quantum computing [27, 53] and nanoscale magnetic field sensing [54]. In this chapter the fundamentals of NV-based magnetometry will be presented. The first section summarizes the electronic, optical, and spin properties of the NV center that are the basis for magnetic sensing applications. Section 2.2 briefly introduces optically detected magnetic resonance techniques and their application to NV centers. Particular important is here the concept of spin echo spectroscopy and dynamic decoupling, which is discussed in section 2.2.3. The third section summarizes different approaches for NV-based magnetometry and spin sensing, addressing also the detection bandwidth and sensitivity of the respective sensing protocols.

2.1 Properties of the NV-center

The NV center has been extensively studied in recent years with regard to its electronic structure and optical and spin properties. A detailed review can be found in reference [9]. Here the most important aspects will be presented.

2.1.1 Structure

Diamond is formed by carbon atoms in a face-centered cubic (fcc) lattice structure with two-atomic base (lattice constant 3.57 Å). The four valence electrons of the sp^3-hybridized carbon form covalent bonds to the neighboring atoms with a bond length of

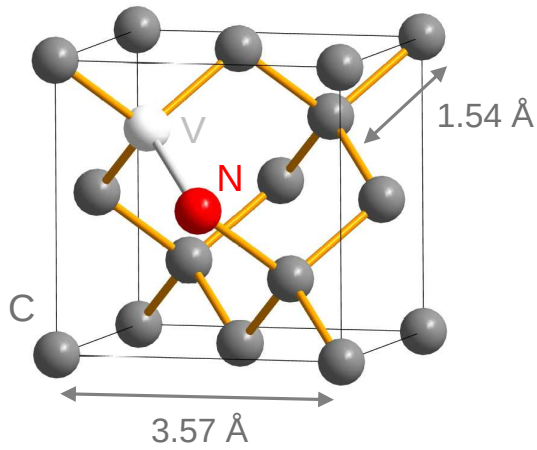

Figure 2.1: Diamond unit cell with NV defect; gray spheres represent carbon atoms, red nitrogen and white the vacancy.

1.54 Å. The strong bonds give rise to the extraordinary hardness and thermal conductivity of diamond. The large band gap of 5.48 eV makes diamond electrically insulating and optically transparent deep into the UV.

Among the many known impurities in diamond the nitrogen-vacancy center is one of the best studied due to its intriguing optical and spin properties. It is formed by a substitutional nitrogen atom and a carbon vacancy on an adjacent lattice site, a model of the diamond unit cell and the NV center is shown in figure 2.1. The center reveals a C_{3v}-symmetry with the symmetry axis given by the vector between the nitrogen atom and the vacancy. The tetrahedral geometry allows four different NV center orientations, corresponding to the four equivalent $\langle 111 \rangle$ directions of the diamond lattice. In the neutral charge state of the NV center (NV^0), the three electrons in the dangling bonds from the neighboring carbon atoms and the two electrons contributed by the nitrogen atom form a 5 electron system with an electron spin S=1/2. Depending on the position of the Fermi level in the diamond the NV center can capture an additional electron from the environment (presumably from a N-donor [55]) and form the negatively charged NV^-, possessing six electrons and a spin S=1. Both charge states are commonly observed; switching between the two has been demonstrated by modifying the diamond surface potential [56, 57] and by selective optical excitation at $\lambda > 575$ nm [58]. Since only the negatively charged state is used for magnetometry, the following discussion deals exclusively with the properties of the NV^- while the "-"-sign in the notation is omitted.

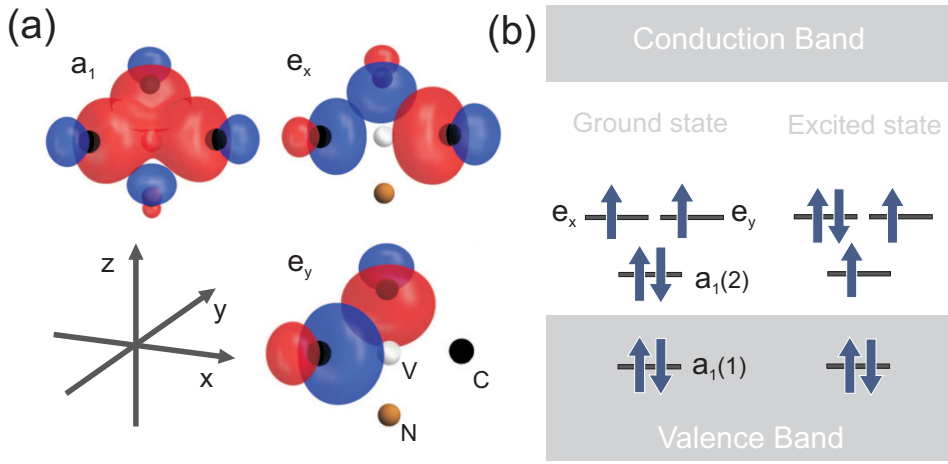

Figure 2.2: Electronic structure of the NV ground state and the first excited state. Image adapted from [62]

2.1.2 Electronic and Optical Properties

The electronic structure of the NV center can be described using a linear combination of the three single-electron molecular orbitals depicted in figure 2.2 (a) [59–61]. Based on group theory the electron configuration shown in figure 2.2 (b) for the electronic ground state and the first excited state can be derived [62]. In the ground state $^3A_2$ the lower two states $a_1(1)$ and $a_1(2)$ are fully occupied, while the degenerate e_x and e_y orbitals are populated by two unpaired electrons. The two electrons form a spin triplet (S=1). In the first excited state, which lies 1.945 eV above the ground state, one electron is promoted from the orbital $a_1(2)$ to the orbital $e_{x,y}$ resulting in the triplet state ^3E. The spin-spin interaction between the two unpaired spins gives rise to a zero-field splitting (ZFS) of the spin triplets [63], which is described in section 2.1.3. The splitting between the $m = 0$ state and the degenerated $m = \pm 1$ states is 2.87 GHz for the ground state and 1.42 GHz for the excited state, respectively [59, 64]. The structure of the singlet system (S=0) is still under debate, but is generally agreed that it involves ^1E and $^1A_1$ states with energies between the ground and excited state of the triplet system [9, 61]. Figure 2.3 (a) summarizes the described level structure.

The solid arrows in 2.3 indicate radiative transitions via electric dipole moment interactions. Between $^3A_2$ and ^3E spin-conserving optical transitions with a zero-phonon line (ZPL) of 637nm can be induced. There are two possible transition dipoles associated

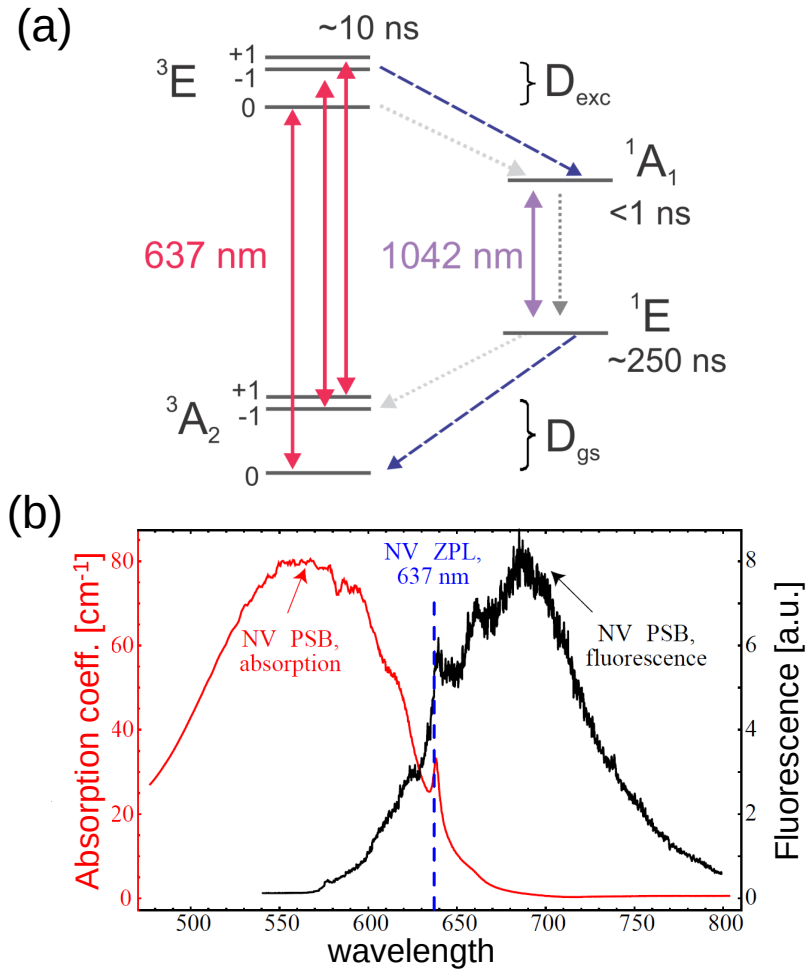

Figure 2.3: (a) Simplified energy levels (b) Room temperature absorption and emission spectra, taken from Ref. [66]

with the excitation of one electron from $a_1(2)$ to either e_x or e_y which are perpendicular to the NV axis and to each other. Therefore excitation with a laser beam propagating parallel to the NV axis is most efficient. The absorption and emission spectra depicted in fig 2.3 reveal broad phonon sidebands (PSB) that can be explained by the Franck-Condon principle: changes of the electronic states by optical transitions change the inter-atomic distances and therefore excite lattice vibrations. *Ab initio* calculations confirm that the e^2 and a_1e configurations corresponding to the $^3A_2$ and ^3E states have significantly different nuclear coordinates [65]. Therefore only 4% of the photons are emitted into the ZPL, whilst the remaining photons relax into the phonon sideband covering a range from 637 nm up to 750 nm. The strong phonon broadening allows an efficient off-resonant excitation of the NV by light in a wavelength range of 500-600 nm.

At low temperature the optical transitions are narrower (in the MHz-range) than

the spacing of the sublevels in the ground and excited state, which enables resonant excitation of transitions between selected spin and orbital sublevels [67–69]. In low temperature experiments the fine structure of the excited state ^3E has to be taken into account: the state is an orbital doublet, in which degeneracy is lifted when the NV symmetry is broken by transverse strain or electric fields. The degenerate ^3E states split then into two orbital branches E_x and E_y, each one formed by three spin states. An additional shift of the energy levels is induced by spin-orbit interactions. At room temperature this fine structure is not observed due to phonon mediated orbital averaging over the fine structure levels [64, 70].

The singlet system is still not fully understood, but a radiative transition with a ZPL of 1042 nm has been detected [71, 72].

Besides the spin-conserving radiative decay there is also a non-radiative relaxation channel from the ^3E state into the singlet system. This inter-system crossing (ISC), depicted by the dashed arrows in figure 2.3, is induced by spin-orbit interaction. The strong spin state dependence of the ISC leads to the unique properties of the NV center, namely optical spin polarization and optical spin readout: For the $m = 0$ sublevels of the ^3E state ISC is strongly suppressed, resulting in a predominantly radiative decay. For the $m = \pm 1$ states the ISC rate is comparable to the radiative decay rate. NV centers which undergo ISC then decay to the long-lived singlet state (labeled ^1E in figure 2.3 (a)), from which they cross over predominantly to the m=0 sublevel of the $^3A_2$ ground state. Since the ISC-decay does not contribute to the 637nm fluorescence, the photon emission rate for the m=0 subsystem is higher than for the ± 1 manifold. The fluorescence contrast can be as high as 30% and is limited by the branching ratios between $m = 0$ and $m = \pm 1$ into and out of the singlet system [73].

The fact that ISC effectively transfers population from $m = \pm 1$ to $m = 0$ leads to an efficient spin polarization by optical cycling. While in thermal equilibrium at temperatures above ~ 1 K the ground state spin sublevels are nearly equally populated (since $D \ll k_B T$, D= 2.87 GHz $\equiv$12 μeV), optical excitation with sufficient intensity results in an accumulation of more than 90% of the total population in the $m = 0$ state [74–76]. This corresponds to spin temperature below 100 mK.

The spin dependent fluorescence and the optical spin polarization are fundamental for optically detected magnetic resonance of NV centers, which will be described in more detail in section 2.2.

Axial ZFS parameter	D_z	2.87	GHz
Transverse ZFS parameter	E	0-10	MHz
g-factor	g_s	2.003	-
Axial hyperfine constant ^{14}N	$A_\parallel$	-2.1	MHz
Transverse hyperfine constant ^{14}N	$A_\perp$	-2.7	MHz
Nuclear quadrupole interaction ^{14}N	P	-5	MHz
Axial hyperfine constant ^{15}N	$A_\parallel$	+3.0	MHz
Transverse hyperfine constant ^{15}N	$A_\perp$	+3.7	MHz

Table 2.1: Parameter used in the Spin Hamiltonian 2.1; values for the hyperfine interaction are taken from reference [77].

2.1.3 Spin Properties

As described in the previous section the ground state is a spin triplet without spin-orbit interaction. Therefore the electron spin is mainly influenced by spin-spin and Zeeman interactions. In a coordinate system with the z-axis along the the NV axis the spin Hamiltonian can be written as [6]:

$$\begin{aligned} \hat{H} &= \hat{H}_{ZFS} + \hat{H}_{EZ} + \hat{H}_{HF} \\ &= (D_z \hat{S}_z^2 + E(\hat{S}_x^2 - \hat{S}_y^2) \\ &\quad + g_s \mu_B \hat{\vec{B}} \cdot \hat{\vec{S}} \\ &\quad + (A_\parallel \hat{S}_z \hat{I}_z + A_\perp (\hat{S}_x \hat{I}_x + \hat{S}_y \hat{I}_y) + P \hat{I}_z^2) \end{aligned} \tag{2.1}$$

The nuclear Zeeman interaction and the nuclear quadrupole interaction are disregarded in this Hamiltonian since these effects are negligible in the experiments discussed in this thesis. The parameters used in the equation are summarized in table 2.1. In the following the various contributions to the Hamiltonian are discussed in more detail.

Zero-field splitting

The first term in 2.1 denotes the zero-field splitting arising from the interaction of the two unpaired electron spins; the two spins are strongly coupled and described by the electron spin operator $\vec{S}$. ZFS occurs only for non-spherical spin densities [6]. For the NV center the main deviation from the spherical symmetry takes place along the NV axis, as can be seen in the molecular orbitals depicted in figure 2.2. Therefore the ZFS affects mainly the S_z component of the spin; $S_{x,y}$ are only influenced when the axial

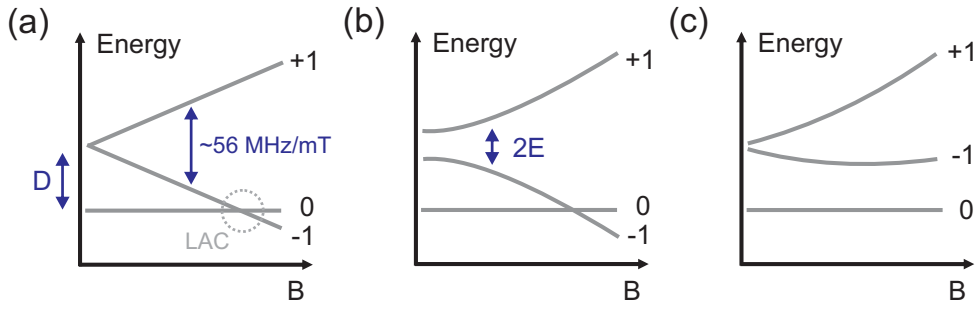

Figure 2.4: Ground state spin levels for various magnetic fields (a) $\vec{B} \parallel \vec{z}$ (b) $\vec{B} \parallel \vec{z}$ with $E \neq 0$ (c) $\vec{B} \nparallel \vec{z}$

symmetry is broken by transversal strain or electric fields. Typical values for E are in the kHz-MHz range and thus significantly lower than D=2.87 GHz.

Zeeman interaction

The second term in 2.1 accounts for the Zeeman interaction of the electron spin with an external magnetic field $\vec{B}$. If $\vec{B}$ is aligned with the z-axis (i.e. the NV-axis) the interaction causes a linear splitting of the $m = \pm 1$ states with ~ 56 MHz/mT, as shown in figure 2.4. For $B \approx 102$ mT there is a level anti-crossing (LAC) where the ZFS is compensated by the Zeeman-shift and strong level mixing occurs [78]. The situation is more complicated if the B-field orientation does not coincide with the NV-axis. For small fields, i.e. $\gamma B \ll D$, the spin quantization axis is given by the NV-axis and the magnetic field can be treated as a small perturbation. For larger fields the quantization axis does not coincide with the NV-axis and therefore m_S is not a good quantum number anymore. The m_S spin states as described in section 2.1.2 are strongly mixed into new eigenstates, resulting in a breakdown of the spin-dependent contrast mechanism in the fluorescence emission and the optical spin polarization. Tetienne *et. al.* demonstrated that for magnetic fields perpendicular to the NV-axis the contrast is already significantly reduced for $B_\perp \approx 10$ mT [79]. The shift of the $m = \pm 1$ levels is not linear in B for misaligned fields; depending on the angle between B and the NV-axis, an asymmetric shift as qualitatively depicted in figure 2.4 (c) is observed.

In most experiments presented in this work the transverse magnetic field is negligible, thus in the following $\vec{B}$ is assumed to be parallel to the NV axis if not otherwise stated.

Hyperfine interaction

The third term in equation 2.1 describes the hyperfine interaction between the electron spin and the nitrogen nuclear spin $\hat{I}$. The nitrogen nucleus associated with the NV

center is either a ^{14}N or ^{15}N isotope; ^{14}N with $I = 1$ is 99.6% natural abundant, ^{15}N with $I = 1/2$ is often used for NV centers generated by ion implantation to distinguish them from native NV centers [80]. For ^{14}N the nuclear quadrupole interaction has to be taken into account, i.e. the interaction between the non-spherical charge distribution of the nucleus with the electric field gradient caused by the asymmetric electron density. Spin-spin and quadrupolar interaction split the $m_s = 0 \leftrightarrow m_s = \pm 1$ transition into a triplet with line spacing $\sim 2.3MHz$. For ^{15}N there is no quadrupolar interaction (since $I = 1/2$) and the spin-spin interaction results in a doublet with splitting $\sim 3.1MHz$ [80]. Since the diamond lattice is predominantly composed of the spinless carbon isotope ^{12}C (98.9% natural abundance) hyperfine coupling to other nuclei can be disregarded in first approximation.

Spin relaxation times

The static spin Hamiltonian given in equation 2.1 does not account for dynamics of the spin system induced by interactions with the environment, e.g. lattice vibrations or magnetic and electric field noise. These effects induce a relaxation of polarization and coherence of the spin system and are typically characterized by two important time scales, the longitudinal relaxation time T_1 and the transverse relaxation time T_2 [6].

In longitudinal relaxation processes the spin quantum number m_S and thus the energy of the spin changes; this energy exchange with the environment involves phonon-mediated mechanisms such as Raman and Orbach processes as well as cross relaxation via dipole-dipole interaction. Although phonon-mediated processes in diamond are relatively weak due to the low spin-orbit interaction and a low phonon density of states, these processes dominate at room temperature in high-purity samples and limit T_1 to a few miliseconds [81–83]. At low temperature, phonon-induced relaxation mechanism are suppressed and T_1 is limited by cross relaxation. T_1 at low temperature depends strongly on the sample purity and can reach 100 s at 5 K in high-purity crystals [83].

Transverse relaxation describes the loss of phase coherence of a spin state. For the NV center, T_2 is dominated by spectral diffusion due to the fluctuations of the local fields arising predominantly from spin-spin interactions [84]:

$$\frac{1}{T_2} \cong \left(\frac{1}{T_2}\right)_{\substack{C^{13} \\ \text{flip-flop}}} + \left(\frac{1}{T_2}\right)_{\substack{\text{nitrogen} \\ \text{impurity}}} + \left(\frac{1}{T_2}\right)_{\substack{\text{paramag.} \\ \text{defect}}} + \left(\frac{1}{T_2}\right)_{\substack{\text{spin-lattice} \\ \text{relaxation}}} \tag{2.2}$$

Depending on the purity of the diamond crystal, field fluctuation induced by the C^{13} nuclear spin bath ($I = 1/2$, 1.1 % naturally abundant) or by electron spins related to nitrogen impurities (known as P_1 centers, S=1/2) or other paramagnetic species

(especially at the diamond surface) can be dominating. The contribution of the last term is usually small even at room temperature due to the low (phonon-induced) longitudinal relaxation rate. Typical T_2 values range from milliseconds for isotopically pure diamond (reduced content of ^{13}C nuclei) [85] down to a few microseconds in N-rich bulk diamonds [82, 86] or diamond nanocrystals [87–89].

The dependence of the longitudinal and transverse relaxation rates on magnetic field fluctuations in the environment can be employed for magnetometry and spin sensing applications. T_1 and T_2 based approaches for spin detection are discussed in more detail in section 2.3.

2.1.4 Fabrication Techniques

Although the NV-center can be found in natural diamond and is an abundant impurity in N-rich artificial diamond, most applications rely on deliberately created centers with a controlled density and distance to the diamond surface. Especially for NV-based magnetometry controlled and precise fabrication techniques are crucial since a high magnetic moment sensitivity requires NV centers close to the surface with long coherence times (see section 2.3.2). A common approach, which is used for most of the samples studied in this work, is the implantation of nitrogen ions into high-purity diamonds grown by chemical vapour deposition [90]. Typical implantation energies are in the keV - MeV range, resulting in a penetration depth into the crystal of nano- to micrometers. The nitrogen ions create vacancies along their penetration path and finally take up substitutional lattice sites. In a subsequent annealing step above 700°C the vacancies become mobile and can form NV-centers with the implanted nitrogen atoms [80,91]. The yield (NV center per implanted nitrogen ion) depends on the implantation energy and is on the order of 1% [92]. The NV-density can be controlled by the nitrogen dose of the implantation, the NV depth depends on the implantation energy. Shallow NV-centers suitable for spin sensing applications can be achieved by implantation energies around 2.5 keV, resulting in a depth of approximately 5 nm below the diamond surface [42].

NV centers produced by ion implantation show in general considerably reduced coherence times compared to native defects (i.e. NV centers formed during crystal growth), presumably due to the presence of paramagnetic defects arising from residual radiation damage [84]. This can be circumvented in the so-called delta-doping approach, where a thin nitrogen-enriched layer is incorporated during the epitaxial diamond growth. Subsequent electron irradiation and annealing yields NV-centers in a defined depth close to the diamond surface with relatively long coherence times [93, 94]. Nevertheless, the generation of shallow NV centers with optimized coherence properties is a topic of ongo-

ing research and much effort is spent on reducing the implantation- and surface-related defect concentration [42, 84, 95, 96].

2.2 Optically Detected Magnetic Resonance

The basis for optically detected magnetic resonance of the NV center is the spin-dependent fluorescence intensity and the optical spin polarization described in section 2.1.2. The ODMR-signal reflects the change in the population of spin states induced by microwave irradiation and is sensitive enough for single spin experiments. This is in contrast to conventional EPR, where the transverse magnetization of a large spin ensemble is detected. However, many pulse sequences and detection schemes developed for conventional EPR can be used in ODMR-experiments with small modifications.

2.2.1 ODMR Basics

ODMR experiments with NV centers can be divided into continuous wave (cw) measurements and pulsed experiments. While cw-ODMR provides a means to measure the energy levels of the NV spin system, pulsed experiments additionally grant access to the time domain and therefore the study of spin dynamics.

Continuous-wave experiments

The simplest method of ODMR spectroscopy on a NV center is to apply simultaneously microwave and optical excitation and to measure the fluorescence intensity in the phonon sideband as a function of microwave frequency. For off-resonant microwave irradiation the system is optically polarized to $m = 0$ and undergoes predominantly radiative transitions from ^3E to $^3A_2$. If the microwave is on resonance with one of the ground state spin transitions, a part of the population is transferred to the $m = \pm 1$ manifold resulting in reduced fluorescence due to the competing ISC decay channel. Typical ODMR spectra of single NV centers are shown in figure 2.5 for various magnetic fields strength and two different sample systems, i.e. a high purity bulk diamond and a nanodiamond. The B-field dependence reflects the Zeeman interaction for axial and transverse magnetic field, which is sketched in figure 2.4. Typical for nanodiamonds is the presence of strain resulting in a transverse zero-field splitting ($E \neq 0$).

The line width in ODMR-spectra is fundamentally limited by the inhomogeneous spin coherence time T_2^* (see the next section 2.2.2 for the difference between T_2^* and T_2). Since nanodiamonds typically contain many magnetic impurities and defects, T_2^*

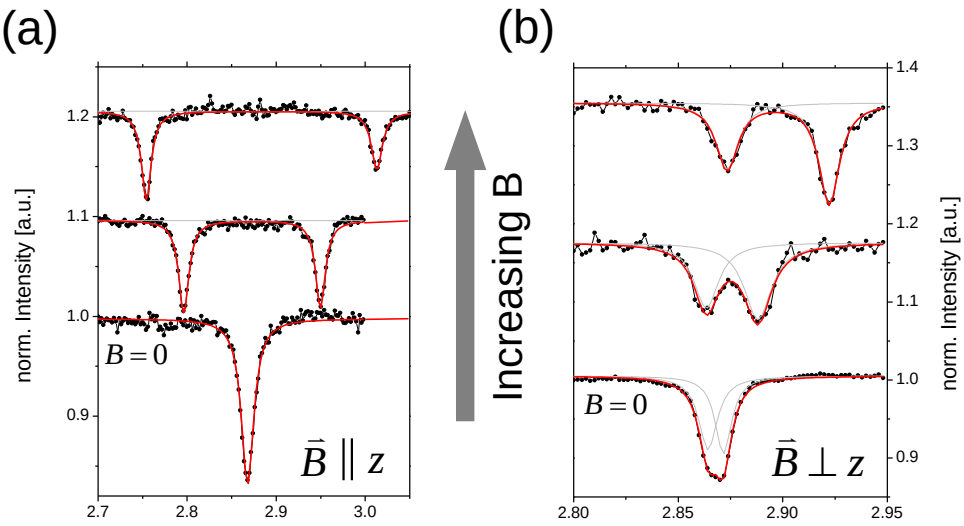

Figure 2.5: Typical cw ODMR spectra (a) bulk diamond, $\vec{B} \parallel \vec{z}$ (b) nanodiamond, $\vec{B} \nparallel \vec{z}$

is usually much shorter than in pure bulk samples, and thus the line width in figure 2.5 is significantly broader. In cw experiments the intrinsic (T_2^*-limited) line width is often superimposed by power broadening effects of the laser and microwave irradiation [97]. This power broadening prevents the observation of the hyperfine structure in figure 2.5 (a). It can be circumvented by reducing the laser and microwave power, at the cost of a reduced signal intensity and spin contrast, or by performing pulsed spectroscopy.

Pulsed ODMR

Pulsed ODMR experiments consist of an initial laser pulse for spin polarization, a series of resonant microwave pulses for spin manipulation, and a laser pulse for spin readout via the florescence intensity. The pulse sequence scheme is depicted in figure 2.6 (a). To read out the spin state at the end of the sequence with a high fidelity, it is crucial to detect the first fluorescence photons after laser switch on before the NV center is repolarized into $|m = 0\rangle$. The time dependence of the fluorescence is depicted in figure 2.6 for the initial spin states $|m = 0\rangle$ and $|m = \pm 1\rangle$. For longer illumination ($t > 500$ ns) both curves reveal the same steady state intensity, which is determined by the ratios of the different transition rates of the ISC. If the initial state is $|m = 0\rangle$ a higher PL intensity is initially observed which drops to the steady state intensity since some population is trapped in the metastable singlet state owing to residual ISC. For an initial state $|m = \pm 1\rangle$ the PL signal rapidly decays to a low level due to fast ISC to the singlet state. Since the singlet state preferentially decays to the $|m = 0\rangle$ ground state the low PL level then recovers toward the steady-state value within the metastable state lifetime

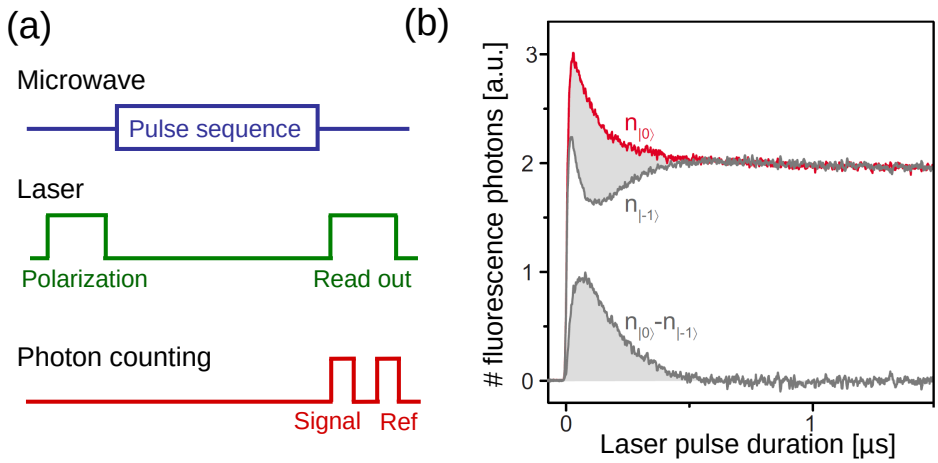

Figure 2.6: (a) Sequence for pulsed ODMR measurements (b) Time dependent fluorescence emission of the $|m = 0\rangle$ (red) and the $|m = \pm 1\rangle$ (gray) state; taken from [98]

($\sim$ 250 ns). The difference between both curves represent the signal photons used for spin state readout.

As can be seen in 2.6, these signal photons can be detected only in a time window of about 300 ns after the laser is switched on. With a typical photon count rate from a single NV in a room temperature experiment of 100 kcts/s on average only 0.03 photons are detected in this interval. With a spin contrast of 30% less than 0.01 photons contribute to the spin state read out. Therefore it is necessary to average over many runs of an experimental measurement sequence to obtain data with a sufficient signal-to-noise ratio. Due to the small number of signal photons the measurement noise in pulsed experiments is usually dominated by photon shot noise.

The microwave pulse sequence applied between the polarization and readout laser pulse depends on the spin properties that are to be studied. The sequences used for T_2-measurements and spin sensing will be discussed in the following sections. In the simplest case the sequence consists only of a single microwave pulse. If the pulse length is chosen appropriately, a spectrum similar to those depicted in 2.5 can be acquired without power broadening effects [97]. A second even more important advantage of the sequential microwave and laser irradiation is that it allows coherent spin manipulation. While the microwave alone leads to a coherent evolution of the NV spin state, this coherence is destroyed in a cw experiment by the probabilistic excitation and emission processes induced by the laser. Since in a pulsed experiment the spin manipulation and evolution happens in the absence of laser illumination, the coherent nature of the

spin dynamics is maintained. This facilitates the advanced coherent control techniques described in the following sections.

2.2.2 Coherent Spin Manipulation and Spin Echoes

Rabi Oscillations

In a small magnetic field, the $m = 0$ to $m = -1$ spin transition of the NV center forms an effective two-level system. Driving this transition with resonant microwave excitation induces population oscillations between the spin sublevels. These so-called Rabi oscillations can be observed by performing pulsed ODMR with varying length of the resonant microwave pulses. Figure 2.7 (b) shows a typical Rabi signal from a single NV center along with the schematic pulse sequence. The spin dynamics under resonant microwave excitation can be visualized in a Bloch sphere as depicted in figure 2.7 (a). In the Bloch sphere, the eigenstates $|0\rangle$ and $|-1\rangle$ of the system coincide with North and South pole of the sphere; the superposition states

$$\Psi_{sp} = \frac{1}{\sqrt{2}}(|-1\rangle + e^{i\varphi}|0\rangle) \tag{2.3}$$

lie on the equator, where the phases $\varphi = 0$ and $\varphi = \frac{\pi}{2}$ correspond to the x- and y-direction, respectively. A driving field polarized in x with frequency ω and strength B_1 is represented in a Bloch sphere in the rotating frame (coordinate system which rotates with ω around the z-axis) as a constant field pointing in x-direction, which causes a Larmor precession of the spin with $\Omega_1 = \gamma B_1$. Therefore the population oscillates with this frequency between the two eigenstates (i.e. the poles of the Bloch sphere). The fluorescence signal S acquired at the end of the pulse sequence corresponds to a projection of the state vector onto the $|m = 0\rangle$ eigenstate, $S \propto |\langle\Psi|0\rangle|^2$. The probability to find the system in this state at time t is

$$P_{|0\rangle} = \left(\frac{\Omega_1}{2\Omega_R}\right)^2 \sin^2(\Omega_R t/2) \tag{2.4}$$

Here, $\Omega_R = \sqrt{\Omega_1^2 + \Delta^2}$ is the Rabi-frequency, and $\Delta = \omega - \omega_0$ describes the detuning of the driving frequency ω to the actual transition frequency ω_0 between $|0\rangle$ and $|-1\rangle$. For resonant driving a complete polarization transfer (i.e. a spin flip with 100% probability) can be achieved for a certain pulse length, referred to as π-pulse (since it corresponds to a 180° rotation on the Bloch sphere). Correspondingly, a $\pi/2$-pulse creates the superposition state Ψ_{sp} described by equation 2.3. This ability for controlled spin flips and creation of coherent states is fundamental for advanced EPR sequences.

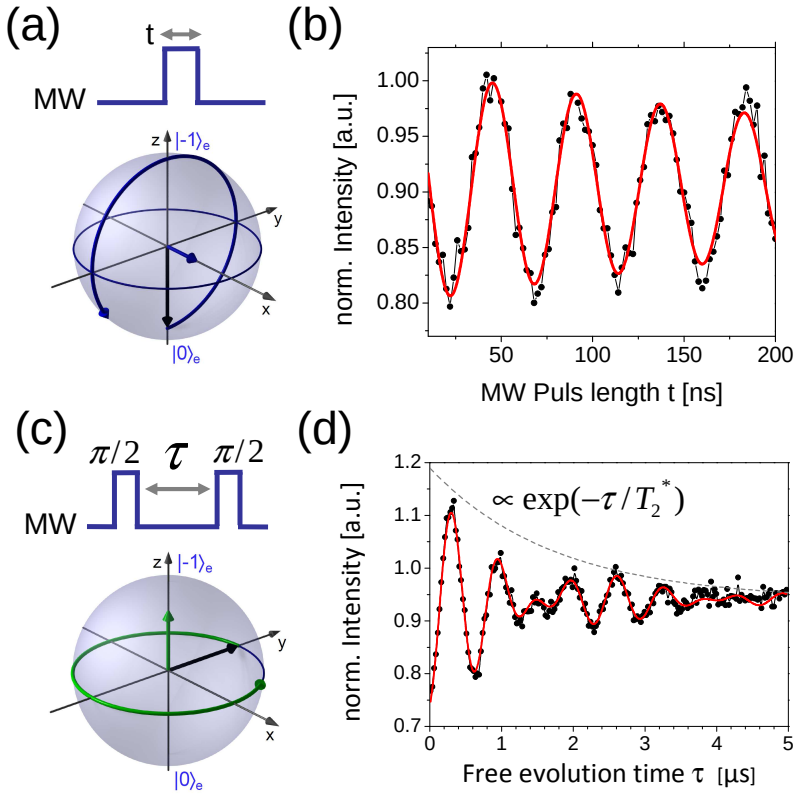

Figure 2.7: (a) Pulse sequence for the observation of Rabi-oscillations and corresponding Bloch sphere representation the spin dynamics in the rotating frame under resonant excitation (adapted from [99]). (b) Experimentally observed Rabi-oscillations in the fluorescence emission. (c) Pulse sequence for Ramsey interferometry and corresponding Bloch sphere representing the free evolution of the superposition state. (d) Free-induction decay in the fluorescence signal.

Ramsey Interferometry

In order to study local magnetic fields and the spin environment of the NV center it is necessary to observe its free (undriven) spin dynamics; this can be carried out by creating the superposition state Ψ_{sp}, letting it evolve freely, and then converting the accumulated phase between the eigenstates $|0\rangle$ and $|-1\rangle$ into a detectable population difference. That is achieved by the pulse sequence $\pi/2 - \tau - \pi/2$, called a Ramsey sequence. A typical fluorescence signal as a function of free evolution time τ is shown in figure 2.7 (d). Such measurement is in analogy to conventional EPR-experiments also called the free-induction decay (FID). During free evolution, the two spin eigenstates forming the superposition accumulate a phase shift depending on the magnetic field

$$\varphi = \gamma \int_0^\tau B(t)\mathrm{d}t \tag{2.5}$$

This can be represented by a rotation of the state vector in the Bloch sphere in the equatorial plane, as depicted in figure 2.7 (c). Thus, in the ideal case of a two-level system with on-resonant excitation in a constant magnetic field the FID would reveal oscillations with the Larmor frequency $\omega_L = \gamma B$. Due to the ^{14}N-hyperfine structure the response of the NV center can rather be described by three independent two-level system (two in case of ^{15}N), resulting in a beating of the signal due to the detuning of the applied microwave pulses to the actual transition frequencies.

The oscillations are damped due to decoherence induced by spin bath fluctuations. In higher purity samples this spin bath is dominated by ^{13}C, which are present with 1.1% natural abundance in the diamond lattice. The decay arises from the averaging over many measurement runs (which corresponds to an ensemble average over many quantum systems): Since the averaging process takes place on a time-scale longer than the spin bath dynamics (flip-flop rate typically $\sim$ kHz), the magnetic field and therefore the oscillation frequency changes between the measurement runs. The spread of different frequencies results in a decay of the averaged signal. This decay is described by the time constant T_2^*, which is referred to as the dephasing time and is typically in the μs-range for NV centers in high-purity diamond.

Although ramsey interferometry can be used to probe the dynamics of the spin bath in the NV environment [100, 101], the strong modulation and rapid decay of the FID limits the magnetic field sensitivity and usually precludes sensing of single spins (see also section 2.3.2). This limitation can be overcome by employing spin echo techniques, which eliminate the phase shifts associated with the static hyperfine interaction and quasi-static effects of the environment.

Spin Echo Spectroscopy

A spin echo measurement is in principle a Ramsey measurement where a π-pulse is inserted in the middle of the free evolution time. The sequence and associated spin dynamics in Bloch sphere representation is depicted in figure 2.8. The π-pulse refocuses the dephasing induced by static and slowly varying magnetic fields; the final state is therefore reached regardless of the actual magnetic field value, as long as the phase shifts induced in both halfs of the free evolution time are the same. The accumulated phase

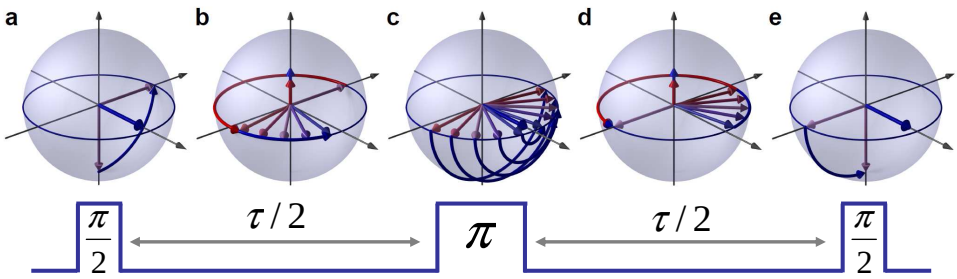

Figure 2.8: Pulse sequence and corresponding spin dynamics for the Spin echo detection (adapted from [99])

during the complete sequence can be expressed as

$$\varphi = \gamma \left(\int_0^{\tau/2} B(t)\mathrm{d}t - \int_{\tau/2}^{\tau} B(t)\mathrm{d}t \right) \tag{2.6}$$

Thus, the spin echo is insensitive to static fields and fluctuations on a timescale longer than the sequence length (i.e. to field noise with frequencies $f_B \ll 1/\tau$). On the other hand, the sequence has maximum sensitivity to fields with frequency around $f_B \sim 1/\tau$. The echo amplitude decays on a time scale referred to as coherence time T_2. Since T_2^* describes decoherence induced by noise over the full frequency range and T_2 only for higher frequency noise, it is $T_2 > T_2^*$. T_2 in diamond depends very strongly on the mesoscopic environment of the NV center and ranges from a few μs in nanodiamonds and N-rich bulk samples to ms in high-purity ^{12}C-enriched diamond. This strong dependence of the spin echo amplitude and its modulation by spin-spin interactions (known as ESEEM: Electron Spin Echo Envelope Modulation) makes it a powerful tool to study the environment of a NV-center, especially the coupling to nearby spins. How spin echo spectroscopy is employed for (single) spin sensing will be discussed in more detail in section 2.3.

An ESEEM effect that is commonly observed in experiments in small magnetic fields is the periodic collapse and revival of the spin echo induced by the ^{13}C spin bath [102]. In a magnetic field the ^{13}C nuclei undergo Larmor precession with a frequency $f_L^{^{13}C} =$ 10.71 kHz/mT and correspondingly generate a time-varying background field with this frequency. With increasing external magnetic field the frequency increases and the refocusing becomes less effective, therefore the echo amplitude decays faster. However, if the echo sequence is timed such that the pulse interval $\tau/2$ commensurates with an integral number of nuclear Larmor periods, the overall phase accumulation due to the

nuclear field is refocused and the spin echo revives.

2.2.3 Dynamic Decoupling

As discussed in the previous section, the coherence time of a NV center is strongly affected by its mesoscopic environment, especially by interactions with a spin bath. Since long coherence times are required for sensitive magnetometry (see next section 2.3), methods to mitigate these interactions have to be employed. One way is to improve the diamond growth process so as to obtain high purity samples with low spin concentrations. Another strategy to reduce the spin bath induced decoherence is to polarize the bath spins by cooling the sample to low temperature and applying a high magnetic field. For N-rich diamond an improvement of T_2 by more than an order of magnitude has been demonstrated by freezing out electron spin bath dynamics at $T = 2$ K and $B = 8.5$ T [82]. However, this approach is experimentally challenging and not applicable to nuclear spin baths due to the small nuclear Zeeman energy.

A promising strategy is to employ dynamic decoupling (DD) techniques, which allow one to reduce the interactions of the NV spin with the environment by driving the NV spin with appropriate pulse sequences. The above discussed spin echo techniques represent a simple form of dynamic decoupling that extends the coherence time by refocusing effects of DC and low frequency fields and shifting the sensitivity window to higher frequencies. A variety of more elaborate DD sequences has been developed for conventional EPR and subsequently applied to ODMR experiments on single NV centers [103–106]. One approach is to extend the spin echo sequence in the way that several π-pulses are applied in the free evolution period to strengthen the refocusing effect. A widely used DD sequence is the Carr-Purcell-Meiboom-Gil (CPMG) sequence depicted in figure 2.9 (a). For a given sequence length T, a higher number of π-pulses n results in a decreasing sensitivity to low frequency fields and a shift of the sensitivity window to higher frequencies.

This frequency dependence can be described by the filter function of the pulse sequence [107, 108]. In general the coherence loss of the NV has the form

$$C(t) = e^{-\chi(t)} \tag{2.7}$$

with the decoherence functional

$$\chi(t) = \frac{1}{\pi} \int_0^\infty \mathrm{d}\omega \, S(\omega) \, F(\omega, t) \tag{2.8}$$

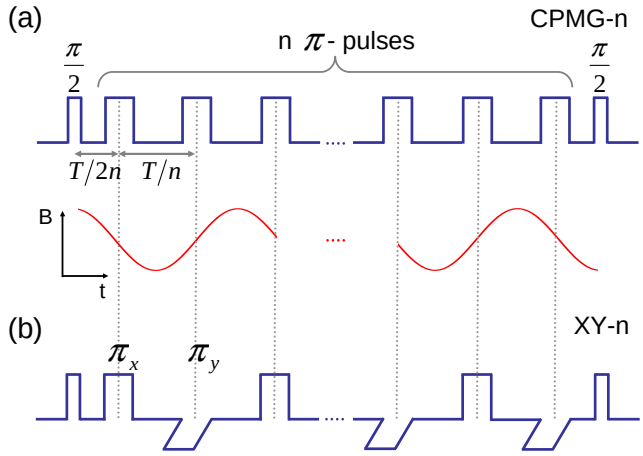

Figure 2.9: (a) pulse scheme for the CPMG-n sequence; the red curve represent the magnetic AC-field to which CPMG has maximum sensitivity. (b) XY-4 sequence with alternating π_x and π_y pulses to compensate for cumulative pulse errors.

$S(\omega)$ is the spectrum of the magnetic field noise in the environment and $F(\omega t)$ is the filter function of the applied pulse sequence in the frequency domain. The coupling of a spin bath to the NV spin can be assumed to yield a Lorentzian noise spectrum [109,110] (see also section 2.3.1):

$$S(\omega) = \frac{\Delta^2 \tau_c}{\pi} \frac{1}{1 + (\omega \tau_c)^2} \tag{2.9}$$

The spin bath is characterized by two parameters: Δ is the average coupling strength of the bath to the NV spin, τ_c is the correlation time of the bath spins, which describes their mutual coupling and is thus related to their characteristic flip-flop time. These parameters depend on the bath spin density n_{spin} approximately with $\Delta \propto n_{spin}$ and $\tau_c \propto n_{spin}^{-1}$.

The frequency domain filter functions associated with the discussed Ramsey, Spin echo and CPMG sequence can be calculated to [107–110]

$$\text{Ramsey} \quad F_R = \left| \frac{\sin(\omega T/2)}{\omega/2} \right|^2 \tag{2.10}$$

$$\text{Spin echo} \quad F_{SE} = \left| \frac{\sin^2(\omega T/4)}{\omega/4} \right|^2 \tag{2.11}$$

$$\text{CPMG-n} \quad F_{CPMG} = 2 \left| \frac{\sin(\omega T/2)}{\omega/2} \frac{\sin^2(\omega T/(4n))}{\cos(\omega T/(2n))} \right|^2 \tag{2.12}$$

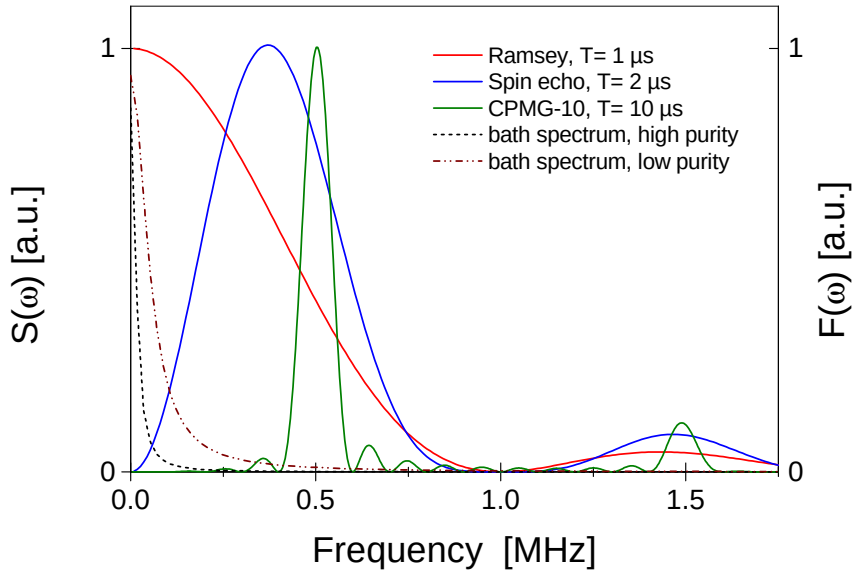

Figure 2.10: Spin bath noise spectra for high and low purity diamond (parameters from reference [109]); normalized Filter functions for Ramsey, Spin echo and CPMG-10 sequence

T is the length of the complete sequence. The filter functions are plotted in figure 2.10. As already mentioned the Ramsey sequence is sensitive to low frequency noise up to the inverse free evolution time - as can be seen in equation 2.5 the accumulated phase shift becomes zero for $f = 1/T$. The spin echo is not affected by low frequency fields due to the refocusing, but is maximally sensitive to fields with $f \sim 1/T$ (compare equation 2.6). Correspondingly, the maximum sensitivity of the CPMG-n sequence is given for $f = n/(2T)$. In the time domain, this frequency dependence can be understood by means of figure fig 2.9 (a); an AC field with a frequency matching the spectral sensitivity of the pulse sequence is illustrated by the red curve. If the half of the oscillation period equals the time interval between the refocusing pulses, the phase shift accumulates over the length of the sequence. For lower or higher frequencies the phase shifts are partly compensated. Since this effect is periodic in frequency, the filter function shows satellite peaks for $fT = (2k-1)N/2$. The main difference between the filter functions of the Spin echo and the CPMG-sequence is the width of peaks; the width decreases with higher order decoupling, i.e. with a larger number n of refocusing π-pulses.

In figure 2.10 also two exemplary spin bath noise spectra are shown. The curves represent equation 2.9 with experimentally determined parameters Δ and τ_c for high

($N \sim 1$ ppm, $^{13}C \sim 0.01\%$) and low ($N \sim 100$ ppm, $^{13}C \sim 1.1\%$) purity diamond from reference [109]. The overlap of noise spectrum and filter function represents the decoherence induced into the NV spin state. The large overlap of the noise spectra and the Ramsey filter function is reflected by a short T_2^*, while the decreasing overlap for spin echo and higher order DD sequences corresponds to longer coherence times T_2.

The efficiency of the CPMG-n sequence in enhancing the coherence time depends on the correlation time of the spin bath. In the limit of very short correlation times, $\tau_c \ll T_2$, the decoupling is inefficient and $T_2 \propto n^0$ (no improvement with number of pulses). In the opposite limit of long correlation times $\tau_c \gg T_2$ the scaling is $T_2 \propto n^{2/3}$ [109].

Another limitation to high-order decoupling with the CPMG-sequence is the detrimental effect of pulse imperfections. A detuning of the microwave frequency, incorrect pulse lengths or fluctuations in driving field amplitude leads to phase errors in the spin manipulation. For sequences comprised of many control pulses these errors add up and reduce the fidelity of the spin manipulation. This can be circumvented by using the XY-n sequence as depicted in fig 2.9 (b). Here the applied π-pulses are alternately polarized along the x- and y-axis of the Bloch-sphere, which is realized by shifting the phase of the microwave pulses by 90°. In this fashion the pulse errors compensate and the fidelity is increased [111]. The above discussed properties of the CPMG-n sequence do apply also to the XY-n sequence, since in the case of ideal pulses the result is identical for both sequences.

For sufficiently long bath correlation times the decoupling of CPMG-n (or XY-n) improves with a larger number of refocusing pulses n and shorter pulse separations T/n. The limiting case for this relationship is reached in the so-called spin-locking regime, where the spins are continuously driven by a resonant microwave field. In this case the spin magnetization is "locked" to the y-axis in the rotating frame and decays with a time constant $T_{1\rho}$ determined by the noise spectral density at the Rabi frequency. For strong driving fields, where the Rabi frequency is comparable to the NV Lamour frequency, $T_{1\rho}$ approaches the NV spin lifetime T_1 [112].

2.3 Application to Magnetometry and Spin Sensing

By detecting the Zeeman shift of the ground state levels the NV center can be employed effectively as an atomic sized magnetometer. Moreover, the sensitivity windows in the frequency domain that can be generated and tuned by appropriate pulse sequences make the NV center a spectrometer for AC magnetic fields arising from other electron or nuclear spins in the environment. In contrast to conventional EPR methods limited to

ensemble measurements, ODMR of single NV centers can be used for probing nanoscale volumes and enables single spin detection. This high spatial resolution and sensitivity is a consequence of the strong distance dependence of the dipolar spin-spin interaction: The coupling of the NV-spin to isolated (nuclear or electron) spins in the environment is given by

$$\hat{H}_{DD} = g_j g_k \frac{\mu_0 \mu_j \mu_k}{2h} \left(\frac{\vec{S}_j \cdot \vec{S}_k}{r_{jk}^3} - \frac{3(\vec{S}_j \cdot \vec{r}_{jk})(\vec{S}_k \cdot \vec{r}_{jk})}{r_{jk}^5} \right) \tag{2.13}$$

$$\approx g_j g_k \frac{\mu_0 \mu_j \mu_k}{2h} \frac{(3\cos^2\Theta - 1)}{r_{jk}^3} \tag{2.14}$$

where $g_{j,k}$ and $\mu_{j,k}$ are the g-factor and magnetic moment of the two spins and $\vec{r}_{jk}$ is the connecting vector with an angle Θ relative to the external field. Equation 2.14 is the high-field approximation valid if $\hat{H}_{Zeeman} \gg \hat{H}_{DD}$. The interaction scales $\propto r_{jk}^{-3}$; for a distance of $r_{jk} = 5nm$ and $\Theta = 0$ (strongest coupling) the interaction strength is $\sim$ 1.6 MHz for NV- e^- coupling and $\sim$ 7 kHz for NV-proton coupling.

Besides the coupling strength, the dynamics of the target spins have to be considered; while isolated spins in small external fields generate low frequency fields due to their rather slow Larmor precession, strongly interacting spin ensembles create typically rapidly fluctuating field noise. By exploiting the variety of sensing protocols developed in pulsed EPR spectroscopy, the NV center can be employed as a wide-band spectrometer covering a frequency range from DC up to several GHz.

The ODMR-spectra presented in figure 2.5 are the most basic form of DC magnetometry with a sensitivity limited by the line width given by $\sim 1/T_2^*$. A much higher sensitivity can be reached by AC sensing schemes detecting changes of either the longitudinal or the transverse relaxation of the NV spin. The former is known as T_1 relaxometry and is susceptible to frequencies at the NV Larmor frequency ω_{NV} ($\sim$ GHz), which makes it especially suitable for detecting rapid field fluctuations arising from a strongly interacting spin ensemble. The latter approach relies on effects on the phase of the NV spin state as probed by spin echo techniques (or higher order DD-sequences) and is most sensitive to fields with frequency on the order of $1/T_2$ (kHz to MHz), as discussed in section 2.2.3.

2.3.1 T_1 Relaxometry

The longitudinal relaxation rate $\Gamma_1 = 1/T_1$ describes the probability of a spin-flip due to an energy exchange with the environment and is therefore susceptible to magnetic

fields with the frequency of the NV spin transitions $\omega_{NV} = D \pm \gamma B_0$. In low external fields, strongly interacting spins in the environment of the NV center (which differ in their transition frequency by less then the average dipolar coupling to the next neighbor) form a fluctuating spin bath due to statistical polarization and cross-relaxation [6]. The spin bath creates a random magnetic field at the NV center position with zero mean ($\langle B \rangle = 0$), but non-zero RMS value ($\sqrt{\langle B^2 \rangle} > 0$). Its dynamics can be described by its autocorrelation function

$$\mathbb{G}(\tau) = \langle B(t)B(t+\tau) \rangle \tag{2.15}$$

In many cases, the autocorrelation function can be approximated in the first order by an exponential decay superimposed to the Larmor precession of the spin bath [7,104,113]

$$\mathbb{G}(\tau) = \left\langle B^2 \right\rangle \exp\left(-\frac{|\tau|}{\tau_c}\right) \cos(\omega_L t) \tag{2.16}$$

where ω_L denotes the precession frequency and the correlation time τ_c describes the dominant time scale of the spin bath dynamics due to flip-flop processes. This correlation time can be interpreted as the inverse coupling strength of neighboring bath-spins [109, 114]. The Fourier transformation of the autocorrelation function yields a lorentzian noise spectrum (which was already used in section 2.2.3):

$$S(\omega) = \frac{\langle B^2 \rangle}{\pi} \frac{\tau_c}{1 + \tau_c^2(\omega \pm \omega_L)^2} \tag{2.17}$$

With $f_{bath} = 1/\tau_c$ and for small external fields ($f_{bath} >> \omega_L$) this can written as

$$S(\omega) = \frac{\langle B^2 \rangle}{\pi} \frac{f_{bath}}{f_{bath}^2 + \omega^2} \tag{2.18}$$

The sensitivity function for T_1 relaxometry is given by the normalized NV resonance line that can be approximated by $F_{T_1}(\omega) \approx \delta(\omega - \omega_{NV})$. With that the longitudinal relaxtion rate can be written as

$$\Gamma_1 = \gamma_{NV}^2 \int F_{T_1}(\omega)\, S(\omega)\, d\omega \approx \frac{\gamma_{NV}^2 \langle B^2 \rangle f_{bath}}{f_{bath}^2 + \omega_{NV}^2} \tag{2.19}$$

Due to the large zero-field splitting ($D = 2.87$ GHz) the NV transition frequency ω_{NV} is in the GHz range even for low magnetic fields, therefore only rapidly fluctuating fields arising from strongly interacting spin ensembles can be probed by T_1-relaxometry. According to equation 2.14, an electron spin bath with average spin-spin separation on the order of a few Å is needed to generate field noise in this frequency range via dipolar interaction. In molecular spin systems, fast spin relaxation can additionally arise from

spin-phonon interactions or rotational and translational diffusion [10]. Using NV-based relaxometry, the detection of Gadolinium-chelates [10], Mn-ions [11], and iron-clusters in Ferritin molecules [11, 115] has been demonstrated. Also paramagnetic defects at the diamond surface have been studied via T_1 relaxometry [116, 117]. However, for the detection of weakly coupled spin systems and especially sensing of individual spins the T_1 based approach is not suitable. These applications require T_2 based techniques discussed in the next section.

2.3.2 Phase Detection Magnetometry

An extremely sensitive method for detecting weak magnetic fields is the measurement of the accumulated phase shift of spin-sublevels in a freely evolving superposition state. This principle is employed, for example, in atomic vapour magnetometers [118] and can also be applied to single NV centers. As described by equation 2.5 in section 2.2.2, the accumulated phase during free evolution is given by the time integral over the magnetic field. Since the maximum integration time is limited by decoherence, the smallest DC field detectable by a Ramsey sequence is given by $B_{min} = \varphi_{min}/(\gamma T_2^*)$. The minimum measurable phase shift φ_{min} is limited by photon shot noise and spin projection noise [118]. With a total accumulation time T, the sensitivity $\eta = B_{min}\sqrt{T}$ for DC magnetometry is approximately [1]

$$\eta_{DC} \approx \frac{1}{\gamma C\sqrt{T_2^*}} \quad \text{(Ramsey)} \tag{2.20}$$

A similar expression can be derived for AC magnetometry using the spin echo sequence:

$$\eta_{AC} \approx \frac{\pi}{2\gamma C\sqrt{T_2}} \quad \text{(Spin echo)} \tag{2.21}$$

The photon shot noise depends on the photon collection efficiency of the experimental apparatus which is described by the parameter $C \leq 1$. Its dependence on the detected photons per shot $\tau_D\Gamma$ (with $\tau_D \sim 300$ ns detection window and Γ the photon count rate) and on the ODMR-contrast Δ can be approximated by

$$C = \sqrt{1 + \frac{2}{\tau_D\Gamma\Delta^2}}^{-1} \tag{2.22}$$

The dependence of C on the photon count rate is plotted in figure 2.11 (a) for two ODMR-contrast values. The estimated AC-sensitivity as funtion of NV coherence time

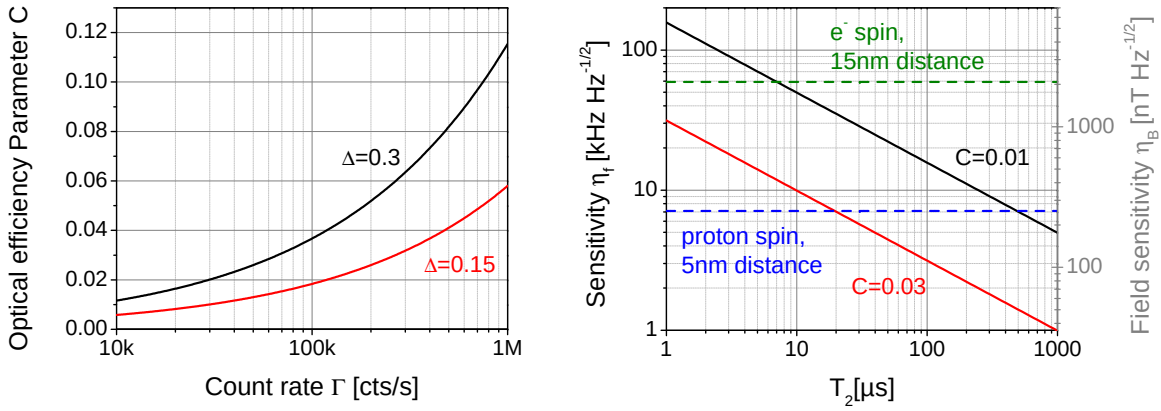

Figure 2.11: (a) Optical efficiency parameter C as a function of NV count rate Γ for two ODMR-contrast values Δ; (b) sensitivity in frequency and field units as a function of coherence time (≈ optimum sequence length) for two values of C. For comparison the approximate coupling strengths to proton and electron spins are depicted as dashed lines.

is depicted in figure 2.11 (b) for two values of C. As can be seen, already for rather low values of C arround 0.01 and T_2 on the order of 10 μs, the detection of a single electron spin at $\sim$ 15 nm distance is possible. For the detection of a single proton spin at 5 nm distance, T_2 has to be roughly 2 orders of magnitude larger. In essence, single spin sensing requires high quality samples, where the NV centers are close to the surface and have long coherence times, and an experimental setup optimized for maximum photon collection efficiency.

The sensitivity of the spin echo is improved relative to the Ramsey sequence by $\approx \sqrt{T_2^*/T_2}$, which is achieved by limiting the detection bandwidth to the sensitivity window of the related pulse sequence. This effect is even stronger for CPMG-n and XY-n sequences; the maximum sensitivity is only obtained for frequencies corresponding to peaks in the filter functions and if the sequence length is chosen such that $T \approx T_2$. For single spin sensing the interaction between the target spin and the NV center thus has to be modulated with a frequency matching the transmission band of the pulse sequence. Since in this approach the measurement signal is extracted from a noisy environment by spectral separation analogous to a classical lock-in detection, this detection method can be seen as a "quantum lock-in amplifier" [119].

The filter function given by the pulse sequence can be tuned by adjusting the number of control pulses and the pulse spacing, which results typically in transmission bands in

the kHz - MHz range. In this range lie also the precession frequencies of nuclear spins in small magnetic fields ($\gamma(^1H)$= 42.6 kHz/mT, $\gamma(^{13}C)$= 10.7 kHz/mT). Thus, nuclear spin detection can be achieved by tuning the nuclear Larmor frequency into resonance with the pulse sequence pass band by an adequate choice of the experimental parameters B, n, and T. Using this approach, sensing of a remote ($\sim$ 3 nm) individual ^{13}C nucleus in the diamond lattice [120] and small ensembles ($\sim 10^5$ spins) of ^1H nuclei in organic molecules on the diamond surface (distance $\sim$ 7 nm) [14] has been demonstrated. If the interaction frequency of the probed spins does not fall in the range accessible by the employed pulse sequence, it can be modulated by actively driving the target spins in a double resonance approach.

2.3.3 Double Resonance

The Larmor frequency of electrons at a given field is three orders of magnitude higher than the nuclear precession, thus phase detection via spin echo or CPMG can not be readily applied for electron spin detection due to their limited bandwidth. To investigate electron spins, they have to be actively driven in a double resonance experiment to generate a signal in the frequency range of an appropriate pulse sequences.

The spin state of electron target spins can be coherently manipulated by resonant radio frequency pulses (28 MHz/mT for free electrons) in the same way as discussed in section 2.2.2 for the NV spin. Since the spin state cannot be read out directly, the result of the spin manipulation has to mapped to the phase of the precessing NV-spin. This is achieved by the double resonance sequence shown in figure 2.12 (a), known as SEDOR (Spin echo double resonance) or DEER (Double electron electron resonance) sequence. In the simplest case, the RF-sequence acting on the target spin is only a single π-pulse that flips the target spin. Due to the dipolar coupling this changes the magnetic field at the NV-position. The timing of this spin manipulation in the middle of the NV spin echo sequence makes the NV extremely sensitive to these field fluctuations. For higher order decoupling sequences the target spin has to be flipped simultaneously to every refocussing pulse on the NV, so that the dipolar coupling between both spins is modulated with a frequency matching the pass band of the filter function. An important requirement for this approach is that the target spin lifetime T_1^t is longer than the sequence length, thus $T_1^t > T \approx T_2^{NV}$ for maximum sensitivity.

Due to the coherent nature of the RF target spin manipulation, more advanced pulses sequences can also be introduced into the SEDOR scheme. The main limitation is that the RF sequence length should be short compared to the pulse spacing in the NV control sequence ($\sim T_2/n$) to allow a sensitive read out. Ramsey and spin echo

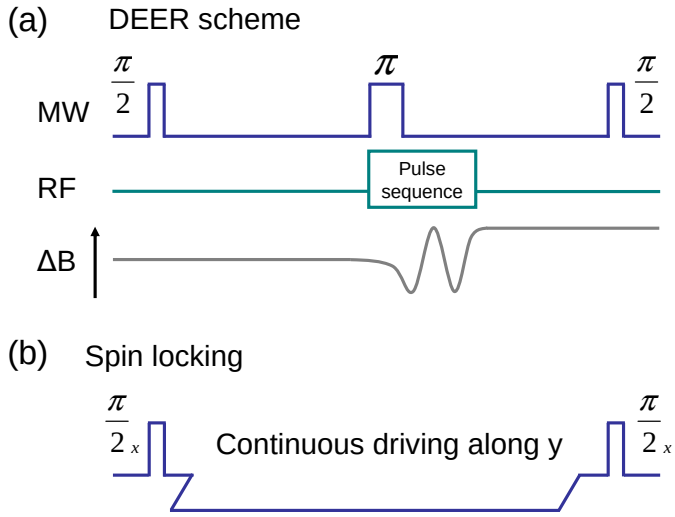

Figure 2.12: (a) Pulse scheme for double resonance experiments: a spin echo sequence is applied to the NV spin; in the middle of the sequence the target spin is manipulated by the RF-pulse sequence. The change in the target spin state creates a variation in the magnetic field detected by the NV spin echo (b) Pulse sequence for spin locking experiments. A superposition state is created by a $\pi/2$ polarized along the x-axis; a continuous microwave field polarized along the y-axis locks the spin in the rotating frame to this axis. For spin state read out, the spin state is projected onto the z-axis.

sequences have been applied to single electron spins in diamond probably related to a N-impurity [121]. Also the observation of Rabi nutations presumably of small ensembles of organic radical spins on the diamond surface has been reported [12,13]. Moreover, double resonance schemes can be employed for nuclear spin detection as recently demonstrated for ensembles of ^1H spins in organic molecules on the diamond surface [15].

2.3.4 Spin Locking

Apart from the phase detection based magnetometry described in the previous two sections, spin sensing can also be performed by employing the spin locking technique [4, 122]. As discussed in section 2.2.3, spin locking can be seen as the limiting case of the CPMG-sequence for $\tau \to 0$ (no free evolution) such that decoherence due to field fluctuations is supressed in a wide frequency range. The pulse sequence applied for spin locking is shown in figure 2.12. The continuous driving with a microwave field with Rabi frequency ω_R results in a quantization of the spin along the microwave field axis in the rotating frame with an energy separation $\Delta E = \hbar\Omega_R$. An additional weak RF-field (e.g. arising from a near target spin) can induce transitions between the parallel and

anti-parallel states only if the RF-frequency matches the Rabi-frequency. The rate of the corresponding spin flip-flops between the driven NV spin and the target spin is set by the coupling strength. Since the Rabi-frequency can be precisely tuned over a wide frequency range by adjusting the microwave power, a controlled coupling between the NV center and individual spins in the environment should be achievable [4]. In contrast to the phase detection technique, the bandwidth of the spin-locking approach extends into the MHz-range, so that electron spins can be detected via their larmor precession.

Since the spin locking technique is not employed in the experiments presented in this thesis, it will not be discussed here in more detail. However, it might be an useful tool for future experiments.

2.4 Conclusion

The combination of spin-state dependent fluorescence, optical spin polarisation and long spin coherence time make the NV center an atomic scale magnetic field sensor with very high sensitivity. By applying spin echo or higher order dynamic decoupling techniques to the NV center, the detection of single electron or even nuclear spins within a few nanometer distance is within reach. However, two important requirements have to be met: the T_2 time of the NV sensor spin close to the diamond surface must be sufficiently long, and the distance between NV center and target spin must be small enough (i.e. $\leq$ 10 nm). While the former requires control over the physical properties of shallow NV centers by optimized surface preparation, growth and implantation techniques, the latter can be achieved by the integration into a scanning probe architecture, which is the intended purpose of the instrument developed in this thesis. From a more technical point of view, the optical collection efficiency and the ODMR contrast are crucial for the achievable sensitivity. The design and realization of the experimental apparatus for scanning probe NV magnetometry at low temperatures will be described in the next two chapters.

Chapter 3

Instrument Design

For the envisaged NV-magnetometry experiments on the single molecule level a combined confocal and atomic force microscope had to be designed and constructed that meets the following demands:

- Optical access with high collection efficiency for sensitive NV spin state read out
- Optical resolution close to the diffraction limit for single NV center experiments
- Microwave and RF-access to the sample for spin manipulation
- Sub-nm stability of the AFM to achieve a controlled coupling between NV and target spins
- Sample temperature close to 4.2 K
- Ultra-high vacuum environment (p$< 10^{-9}$ mbar)
- Rapid sample and tip exchange

Only a subset of these demands is commonly met in specialized experimental setups, while their combination in one instrument is technically extremely challenging and has not been realized so far. Our approach for constructing such an instrument is summarized in this chapter.

3.1 System Overview

Before the design of the instrument is presented in detail, a brief overview of the setup is given. General design concepts are discussed in the first section, while the different sub-systems will be characterized in the following sections.

3.1.1 Design Concepts

While combined confocal and atomic force microscopes operating at ambient conditions are widely used [123–125], low temperature setups are less common and technically far more challenging. In general, optical access to the sample at low temperature can be realized in two ways: One approach is to keep all optical elements at ambient conditions and to focus and collect the light through view ports in the cryostat [126]. This requires a long working distance front lens and thus a smaller solid angle for light collection. Furthermore, the view ports cause optical aberrations that have to be corrected by additional optical elements for high quality imaging. Aberrations and long working distance typically reduce the performance of the imaging system. An alternative approach is to mount the focusing and light collecting element inside the cryostat, which avoids aberrations by windows and enables short working distances [127, 128]. This facilitates a potentially better collection efficiency and thus higher count rates in NV-center experiments. Since the sensitivity in spin sensing experiments depends strongly on the experimentally achieved count rate (see 2.3.2), we opted for this "cold lens" approach for our setup. Having the optical element and the sample at the same temperature also enables a more compact design without temperature gradients, resulting in a higher mechanical stability. The details and technical challenges of the optical access in the cryostat are addressed in section 3.2.1. To avoid transmission losses and background fluorescence related to the use of optical fibers, we realized a free-beam access to the optical element in the cryostat.

Laser, microwave and RF excitation introduce a strong heat load to the the system, resulting in the need for a high cooling power of the cryostat. This is commonly achieved by using an exchange gas [128, 129] or by immersing the sample in liquid helium [130], which is in our case excluded by the need for ultra-high vacuum conditions. We therefore employ a cold-plate cryostat and designed the system in a way guaranteeing an efficient coupling to the liquid helium reservoir. The required ultra-high vacuum conditions additionally makes demands to the temperature compatibility (bake out at $\sim 130°$) of the setup and the vapor pressure of the used materials.

Atomic force microscopy under ambient conditions is commonly performed by vibrating a cantilever, whose motion is optically detected via the deflection of a laser beam (see e.g. reference [131]). Although this technique is considered to be very reliable and sensitive, its integration and alignment in a low temperature system is challenging. In our setup we therefore employ a tuning-fork based approach [132] that features an all-electrical detection of the cantilever oscillation and is therefore well suited for integration into a low temperature UHV setup. To achieve sub-nm or even atomic resolution the

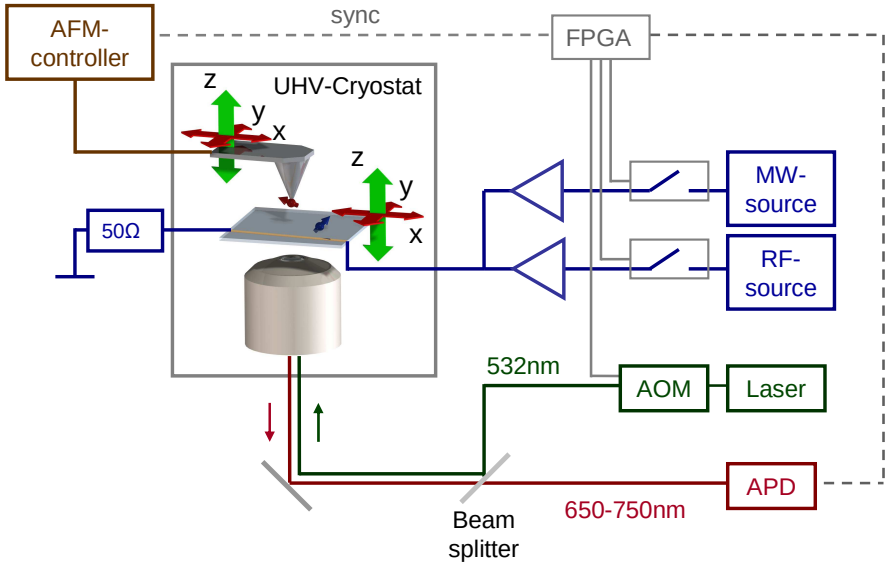

Figure 3.1: Schematic of the system architecture

complete system has to be designed for high mechanical stability.

3.1.2 Overview Scheme

The experimental setup is composed of different sub-systems, i.e. the confocal microscope, the atomic force microscope, the high-frequency (HF) facilities, and the vacuum system with the cryostat. A block diagram of the setup is depicted in figure 3.1. The central element is the microscope head that contains the AFM-scanner, the sample with HF transmission lines, the front lens of the confocal microscope, and piezomotors for tip and sample positioning. It is situated in UHV and cooled to liquid helium temperature.

The confocal microscope consists of the excitation channel with a green laser and an acousto-optical modulator (AOM) for pulsed excitation and the detection channel with an avalanche photo-diode (APD) capable of single photon detection. Apart from the front lens used for focusing the laser light and collecting the fluorescence photons, all components of the confocal microscope are mounted outside the vacuum system. The microwave and RF fields for NV and target spin manipulation are generated by two high frequency sources and coupled into a waveguide on the sample via an impedance matched transmission line in the cryostat.

The coordination of the pulse sequences in ODMR experiments is carried out by a Field Programmable Gate Array (FPGA) triggering the AOM and switches for the RF and microwave signal. The FPGA also enables the time-gated read out of the

APD required for the NV spin state detection in pulsed experiments (see section 2.2.1). The atomic force microscope is controlled by a commercial electronics (Nanonis SPM controller, Specs Zürich), which is synchronized with the ODMR control system for combined experiments.

The different sub-systems of the setup are described in more detail in the following sections.

3.1.3 Confocal Microscope

Addressing single NV centers in ODMR experiments is achieved by confocal microscopy. Compared to conventional optical wide-field microscopy this technique offers an enhanced contrast and resolution by confining the excitation and detection volume to a focus spot close to the optical diffraction limit [133]. The collection efficiency and thus the photon count rate detected on a single NV depends primarily on the numeric aperture and the performance of the front lens which is situated in the cryostat. This component is an important building block of the microscope head and is discussed in detail in section 3.2.1.

A scheme of the confocal microscope is depicted in figure 3.2. The green light (532 nm) from a frequency-doubled Nd:YAG laser is focused by the front lens onto the sample in the cryostat to excite the NV center. The emitted fluorescence light is collected by the same lens. A dichroic mirror acts as beam splitter to separate the excitation (green light) and detection (red light) channel. The fluorescence light is focused through a pin hole and then detected by an avalanche photo-diode. A 650 nm long pass filter in front of the detector rejects scattered photons from the excitation light. The pin hole serves as spatial filter blocking light emitted from parts of the sample that are not in the optical focus. Thus, ideally only photons emitted from a diffraction limited volume reach the detector. The lateral and axial dimension $(\Delta r, \Delta z)$ of this focus region is given by [133]

$$\Delta r = \frac{0.44\,\lambda}{\mathrm{NA}} \tag{3.1}$$

$$\Delta z = \frac{1.5\,n\,\lambda}{\mathrm{NA}^2} \tag{3.2}$$

$$\mathrm{NA} = n\,sin(\Theta) \tag{3.3}$$

where λ is the wavelength, NA is the numeric aperture of the front lens, Θ is the half angle of the focused light cone and n is the refractive index of the medium (n=1 for vacuum). In practice, this optimum resolution can be degraded by optical aberrations.

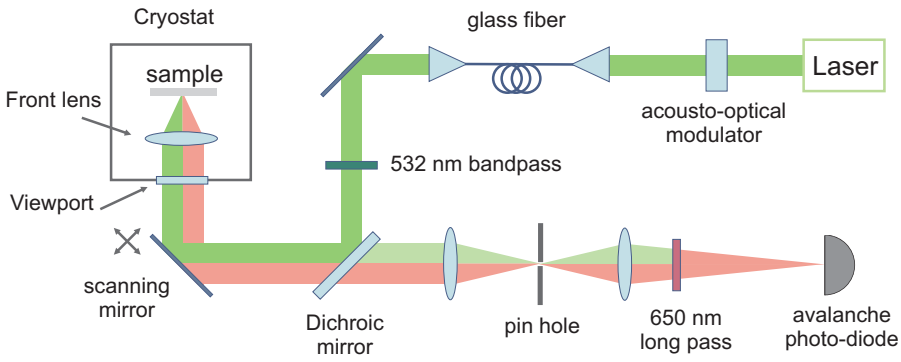

Figure 3.2: Simplified setup of the confocal microscope; the beam path of the excitation and fluorescence light is depicted in green and red, respectively.

To acquire an image, the focus has to be scanned over the sample. This can be achieved by moving the sample with the piezo positioner in the microscope head (see section 3.2) or by scanning the laser beam with a piezo-based scanning mirror (PI S-330.8). The latter enables faster scanning and a higher reproducibility, but the scan range is limited by the field of view of the front lens.

For pulsed excitation the laser is switched by the AOM (Crystal Technologies, model 3350-192). Its operation principle is based on the diffraction of light by sound waves in a TeO_2 crystal, which enables switching with a rise time of $\sim$ 10 ns. The employed APD (Excelitas SPCM-AQRH-10) is capable of single photon counting with a detection efficiency of 65% at 650 nm and a dead time of 20 ns.

3.1.4 Microwave and Radio-frequency Setup

To manipulate the NV spin and target spins in double resonance experiments, microwave and radio-frequency fields have to be applied to the sample. For the small magnetic fields used in the experiments in this work (around 10 mT) the frequencies are typically in the range of 2.4 - 3.4 GHz for NV spin manipulation and 100 - 500 MHz for electron target spins. A scheme of the high frequency setup is shown in figure 3.3. Two separate signal generators (Vaunix Lab Brick LSG-451 and LSG-402) are employed to generate fields in the required frequency range with a maximum output power of $\sim$ +10 dBm. These signals have to be amplified to drive fast Rabi oscillations on the spins, which is achieved by two amplifiers delivering a peak power of 42 dBm (16 W).

Microwave and RF pulses are created by fast switching the respective signal before it is send into the amplifier. The employed switches feature a rise time below 1 ns,

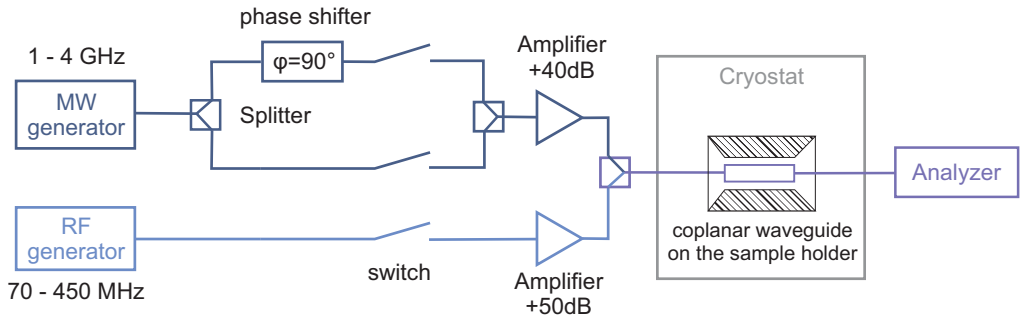

Figure 3.3: Scheme of of the high frequency setup

resulting in rectangular pulses within a good approximation. The switches as well as the AOM in the optical setup are controlled by a FPGA that coordinates the whole experimental sequence. Its timing resolution is up to 2.5 ns.

Sophisticated pulse sequences that are compensated for pulse errors (e.g. XY-n, see section 2.2.3) require microwave pulses with 90° phase shift relative to each other. This is achieved by splitting the MW signal and sending one half through a phase shifter. Both signals are controlled by separate switches and combined before they reach the amplifier.

After the amplification stage, the microwave and RF signals are combined and coupled into the transmission line in the cryostat via a coaxial UHV feedthrough. The field is guided through coplanar waveguides on the sample holder and from there through a stripline or a thin copper wire ($\sim$ 20 μm thickness) across the sample. The oscillating magnetic field around the current carrying wire is used for spin manipulation. Details of the sample holder design are presented in section 3.2. The transmitted signal is guided outside the cryostat and sent to an analyzer device for experiment surveillance.

To obtain a strong driving field (i.e. fast Rabi oscillations) in the vicinity of the sample stripline a transmitted power on the order of 10 dBm is required. To achieve this without strong power dissipation in the cryostat, losses due to reflections and ohmic damping have to be minimized. For signals in the GHz-frequency range it is therefore important that all transmission lines are impedance matched to 50Ω to reduce reflexions.

3.1.5 Atomic Force Microscope

In our setup, the AFM is intended to be used primarily for positioning the NV center and the target spin relative to each other with nanometer precision. In general, AFM enables the study of the sample topography and interaction forces down to the atomic scale [52, 134]. The operation principle is based on scanning a sharp tip over the sample

surface, using the interaction forces to control the distance between tip and sample. The forces are measured by mounting the tip to a cantilever that is vibrated at its resonance frequency. The distance-dependent tip sample interaction induces a shift of the resonance frequency f, which can be approximated by

$$\Delta f = \frac{f_0}{2k} \langle k_{ts} \rangle \tag{3.4}$$

where $\langle k_{ts} \rangle = \langle -\partial F_{ts}/\partial z \rangle$ denotes the force gradient of the tip-sample interaction F_{ts} averaged over one tip oscillation cycle, k is the stiffness of the cantilever and f_0 is its free resonance frequency (i.e. in the absence of tip sample interactions). A detailed discussion of tip-sample interactions in atomic force microscopy can be found for example in references [52, 135, 136].

In our setup we use a quartz tuning fork as vibrating cantilever in a so-called Q-plus design [132, 137]. The piezoelectric effect leads to charge fluctuations when the tuning fork is oscillating. Electrodes fabricated on the tuning fork enable a read out of the mechanical motion by detecting the current between the electrode and ground. The inverse effect can be used for the excitation of the tuning fork by applying an AC voltage to one of the electrodes.

Since the Q-factor of the oscillating tuning fork (defined as the ratio of the energy stored in the oscillator and the energy loss per cycle) is on the order of 10^5 in an UHV and low temperature environment, we employ frequency modulated (FM) feedback control; the oscillation amplitude is kept constant while the excitation frequency is locked to the actual resonance frequency. The frequency shift relative to the free resonance is used for controlling the tip sample distance. In contrast to amplitude-modulation (AM) feedback, which is commonly employed in experiments under ambient conditions and which uses the change in oscillation amplitude at constant excitation frequency as feedback signal, the control bandwidth b in FM mode is independent of Q (while $b \propto 1/Q$ in AM-AFM) [131, 136]. This enables relatively fast scanning speeds while the high Q-factor improves the sensitivity ($\delta(\Delta f) \propto 1/\sqrt{Q}$).

Figure 3.4 shows a block diagram of the feedback control used in our setup. The tuning fork is excited by an AC voltage at its resonance frequency which is typically around 30 kHz. The mechanical oscillation generates a signal current on the order of pA for vibration amplitudes around 1nm. The signal passes two amplification stages; the first one is a home-build transimpedance amplifier with a gain of 10^8 V/A. It is integrated into the microscope head enabling a short connection to the tuning fork, which improves the signal-to-noise ratio. The second stage outside the cryostat has a variable gain of 1-100 and is combined with a band-pass filter with adjustable center frequency to single out

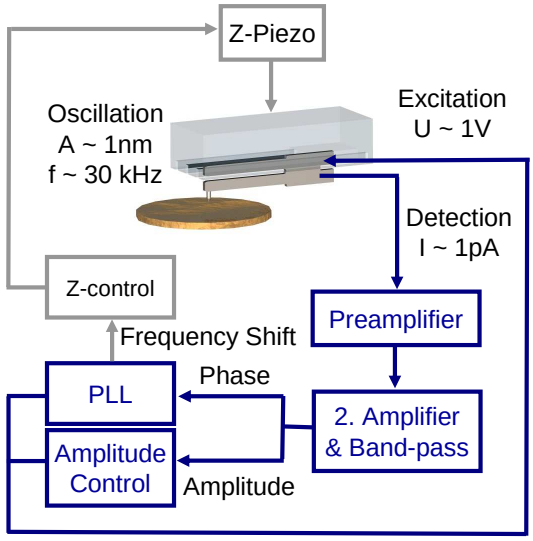

Figure 3.4: Feedback control loops for atomic force microscopy in frequency-modulation mode

the tuning fork signal from the background noise. The amplified and filtered signal is fed into the AFM-controller (Nanonis SPM-Controller, Specs Zürich). Amplitude and phase are used for a closed-loop control of the excitation voltage: One feedback loop controls the excitation amplitude to maintain an constant signal amplitude, while a phase-locked loop (PLL) is used to adjust the excitation frequency to the actual resonance frequency by setting the phase shift of both signals to $\pi/2$ (resonance condition). A third feedback loop controls the tip-sample distance to keep the shift of the resonance frequency relative to the free resonance frequency at a defined set point value.

3.2 Microscope Head

The microscope head can be considered as the heart of the instrument since it combines the key components of the previously described sub-systems, i.e. the front lens of the confocal microscope, the high frequency waveguides to the sample and the AFM scanner with the tuning fork. In Addition, it houses the various piezo actuators for sample and tip coarse positioning. Its design is crucial for the mechanical stability and thus the performance of the AFM, furthermore it determines the cooling efficiency since heat is transferred from the sample to the cryostat by thermal conduction of the head components.

3.2.1 Low Temperature Optical Access

The key challenge in designing the microscope head is the realization of the optical access to the scanning tip with high collection efficiency. Similar challenges were addressed in various vacuum setups by using high NA objective lenses [128], optical fibers [138], single lenses [139–141], or parabolic or ellipsoidal mirrors [142–144].

High NA objective lenses are commonly employed for room temperature experiments and typically consist of sophisticated multi-lens systems to correct for aberrations, including doublet and triplet lenses made from different glasses and connected by optical cement. As an example, figure 3.5 (a) shows a cross-section through a high NA objective lens (Zeiss). The complex lens assembly is designed in a way that the inevitable aberrations from the individual lenses compensate each other and thus an imaging performance close to the diffraction limit over a wide field-of-view and across a broad wavelength range is reached [147]. Temperature (and to a lesser extent also pressure) affect the performance of such an optical system in multiple ways [148]: First, the index of refraction and the dispersion of glass depends upon temperature. Second, glass expands and contracts with temperature, which alters the curvature radius and thickness of a lens. Third, the spacings between lens elements changes due to the expansion and contraction of the mounting material (in objective lenses this is usually brass). The temperature dependence of the refraction index and the thermal expansion of different glasses and brass is shown in figure 3.5 (b) and (c). Consequently, the correction of aberrations in a lens systems optimized for room temperature operation becomes less effective at low temperature and thus the imaging performance decreases. Moreover, thermal stress induced by different thermal expansion coefficients of the employed glasses and of the mounting material can lead to cracking of the optical cement or to stress birefringence [148]. Since high-NA objective lenses designed for low temperature operation are not commercially available, either suitable room temperature objective lenses have to be employed to the cost of a reduced performance, or alternative solutions have to be implemented.

Single aspheric lenses are less sensitive to temperature and have been used under cryogenic conditions [140, 141]. The surface profile of an aspheric lens is optimized to eliminate spherical aberrations for a defined design-wavelength [148]. We carried out simulations (using the optical design software Zemax) for different commercially-available aspheric lenses to estimate their performance in the required wavelength range (532 nm for focusing the excitation laser, 650-750 nm to collect the NV fluorescence). Figure 3.6 shows the results for a lens with NA 0.68 and working distance 1.76 mm designed for a wavelength of 830 nm (Geltech 352330). The main drawback of single

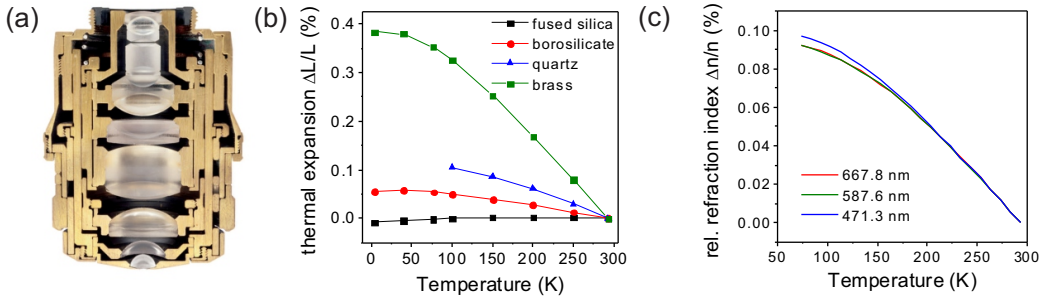

Figure 3.5: (a) Cross-section through a high NA objective lens. (b) Relative thermal expansion for different optical glasses and brass [145]. (c) Temperature dependence of the refraction index of fused silica glass [146].

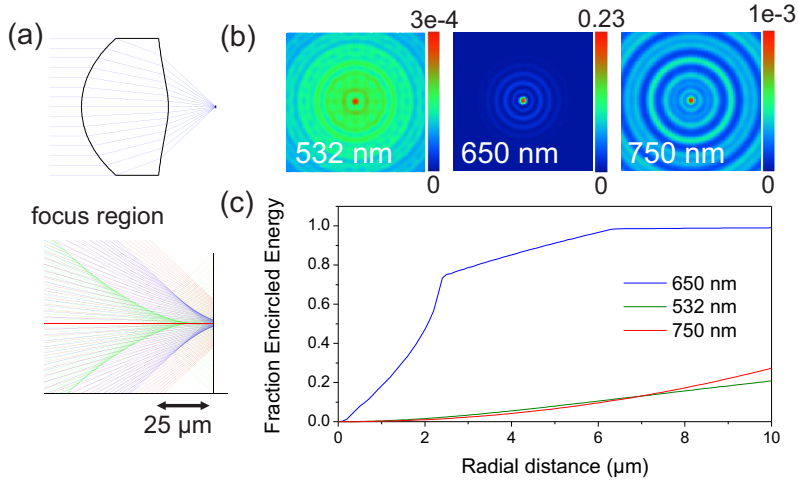

Figure 3.6: Simulated focus of an aspheric lens. (a) Lens layout and axial focus shift for 532 nm (green), 650 nm (blue) and 750 nm (red) light. (b) Intensity distribution in the the focus plane. Image size 10 x 10 μm, intensity relative to an ideal (diffraction-limited) lens. (c) Fraction of encircled energy as a function of spot radius in the focus plane.

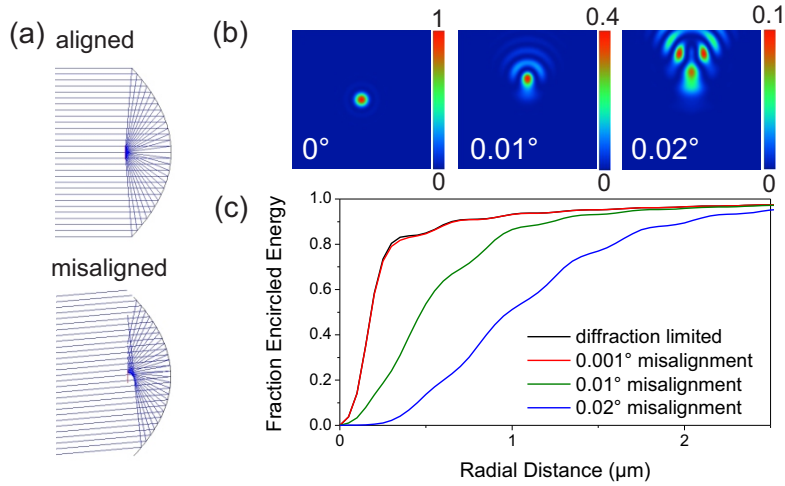

Figure 3.7: Simulated focus of a parabolic mirror for a misalignment of mirror axis and incoming wavefront. (a) Schematic illustration (exaggerated). (b) Intensity distribution in the focal plane, image size 5 x 5 μm. (c) Fraction of encircled energy as a function of spot radius.

lenses is the large chromatic focus shift; as can be seen in figure 3.6 (a), the focus spots for 532 nm and 750 nm are shifted by roughly 50 μm on the optical axis. Figure 3.6 (b) and (c) show the intensity distributions and the corresponding encircled energy over radius for three representative wavelengths at a fixed working distance chosen to yield a tight focus for 650 nm light. As consequence of the axial chromatic aberrations, the intensity distributions for 532 nm and 750 nm are extremely blurred. For the excitation light, this poor focusing would result in the need for high laser power and thus a high power dissipation in the cryostat. For the detection channel, it corresponds to a wide spatial distribution of the fluorescence light in the pinhole plane of the confocal microscope; to obtain a high collection efficiency, a large pinhole diameter had to be used to the cost of a high background and thus a poor signal-to-noise ratio. These results suggest that the imaging performance of a single lens is insufficient for sensitive measurements on NV centers at low temperature.

Metallic mirrors on the other hand do not show any chromaticity and are fully low temperature compatible. Confocal microscopes using high NA parabolic mirrors have demonstrated spatial resolution close to the diffraction limit under ambient [149] and cryogenic conditions [150]. However, parabolic mirrors feature a poor off-axis performance, requiring a precise alignment of the optical setup. This is illustrated by the simulations presented in figure 3.7; for a parabolic mirror with a NA of 0.95, the intensity distribution in the focal plane along with a plot of the encircled energy is depicted for different misalignment angles between the incoming wavefront and the mirror axis. For perfect alignment the imaging is diffraction-limited without any aberrations and independent of the wavelength. Already for a small misalignment of 0.01° the focus intensity distribution becomes distorted and blurred. A similar detrimental effect on the focus arises from phase errors of the light wavefront caused by imperfections of the parabola shape or other components in the beam path (collimator, vacuum view ports, etc.) [150–152]. These effects make the use of a parabolic mirror in a vacuum and low temperature environment very challenging.

Based on these considerations we decided to pursue two approaches in parallel and designed a versatile setup in which an objective lens as well as a parabolic mirror can be employed. The two possible configurations for optical access are schematically shown in figure 3.8 (a) and (b). When using the parabolic mirror, the sample is supported by a transparent sapphire plate, while the AFM tip is mounted on a piezo tube situated in a bore in the center of the mirror. Alternatively an objective lens can be mounted beneath the sample. In this geometry one is limited to transparent samples, but it enables the use of lenses with a short working distance and thus a high collection efficiency.

3.2.2 Head Assembly

The microscope head is designed for utilizing either an objective lens or a parabolic mirror with only small modifications. To align AFM tip, sample and optical focus, nanopositioning with six degrees of freedom is required. In our design, tip and sample can be moved independently in three dimensions, while the optical element is fixed to guarantee a stable alignment relative to the optical setup outside the vacuum system (which is especially important when a parabolic mirror is used). The main components of the microscope head are shown in the exploded view depicted in figure 3.9 (a). It consists of the tip positioner unit with the AFM scan assembly, the sample stage, a rigid housing and the interface plate that connects to the cryostat and holds the wiring.

The sample stage features a 50 mm aperture in the center providing optical access to the sample from the bottom. The objective lens can be mounted in this free space as depicted in figure 3.9 (b), or the parabolic mirror can be placed above the sample as shown in figure 3.9 (c). The large aperture facilitates the use of parabolic mirrors up to $\sim$ 40 mm in diameter for illumination and light collection. The sample stage and the AFM unit are described in detail in sections 3.2.3 and 3.2.4.

For the mechanical stability of the instrument, which is especially crucial for AFM-experiments, the design of the housing is important. Its stiffness should be as high as possible to yield high resonance frequencies, which make the instrument less sensitive to environmental vibrations (e.g. building vibrations or acoustic noise) [153]. The shape and dimension of the housing in our design was optimized by carrying out finite element simulations of its eigenfrequencies and related vibrational modes. By this optimization a substantial increase of the eigenfrequency could be reached; the two lowest modes have frequencies of $\sim$ 1.5 kHz and $\sim$ 2.5 kHz and correspond to a pendulum motion in x and y direction, respectively.

The microscope head is designed to operate in a temperature range from room tem-

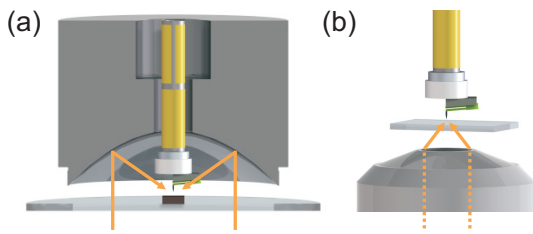

Figure 3.8: The two optical detection schemes which can be realized in the microscope head: (a) Parabolic mirror (b) Objective lens.

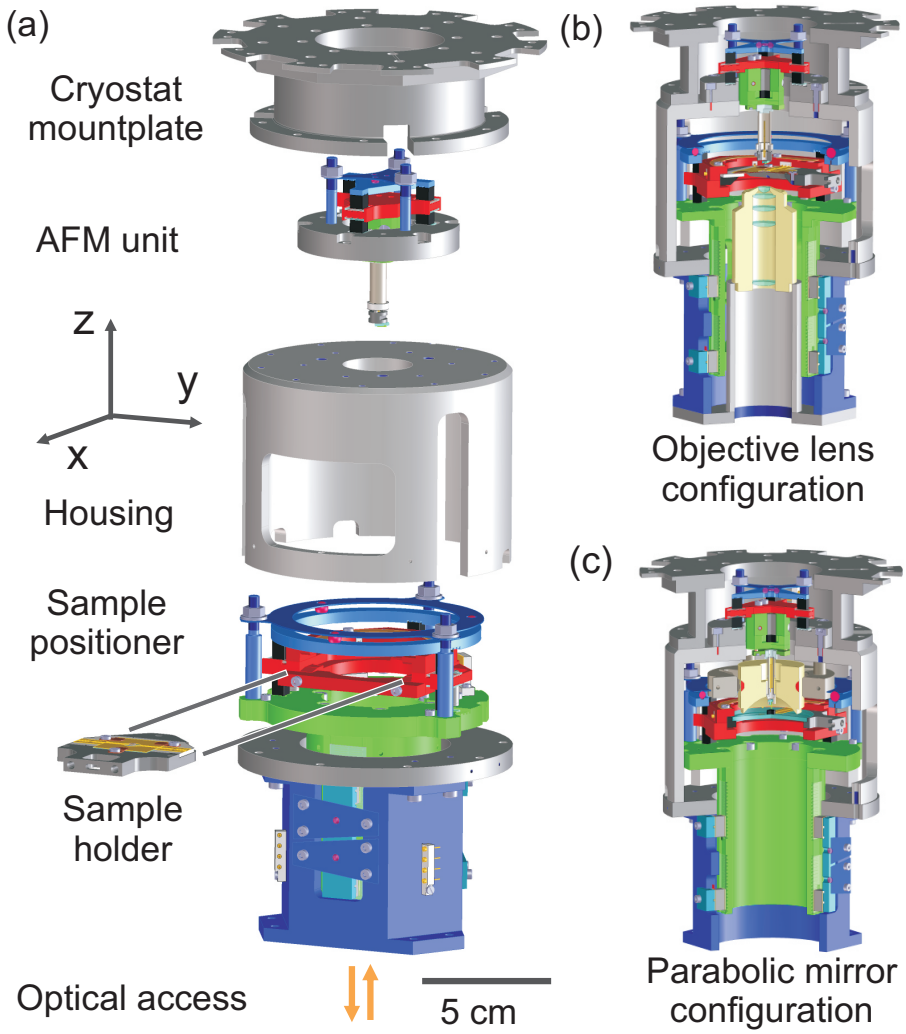

Figure 3.9: (a) Exploded view of the microscope head (b) Cross section with mounted objective lens (c) Cross section with mounted parabolic mirror; Components depicted in red are parts of the piezo positioners moving in the xy-plane, green parts are moving in z-direction.

perature down to 4.2 K and also has to withstand bake out temperatures about 400 K required to achieve UHV. Therefore the materials have to be chosen with respect to their thermal conductivity, heat capacity, thermal expansions coefficients, and vapor pressure. The thermal conductivity is especially important since the thermal coupling between sample and cryostat is achieved almost exclusively via heat conduction through the microscope head components. Since all the parts are fabricated in the workshops in house, also the machineability has to be taken into account. Most parts of the microscope head are machined from phosphor bronze (CW453K : 92% Cu, 8% Sn, 0.1% P)

	Thermal conductivity [W/(m K)]		Heat capacity [J/(g K)]	Thermal expansion $[10^{-6}K^{-1}]$
	300K	10K	300K	300K
Phosphor bronze	67 [154]	1.7 [155]	0.377 [154]	18.0 [154]
OFHC copper	397	1500	0.385	16.5
Macor	1.46 [156]	0.25	0.79 [156]	0.93 [156]
Alumina	35	5.6	0.88	8.4
Sapphire	47	2900	0.779	5.4
PZT piezo ceramic	1.1-2.1 [157, 158]		0.35 [157]	3.0-4.7 [158]
Stainless Steel	15	0.9	0.48	14.5
Titanium	21.9	14.3	0.522	8.6
Diamond	2300	317	0.4715	1.18
Manganin	22	∼1	0.406	18.7

Table 3.1: Thermal properties of various materials used in the setup. Values according to references [145, 159] unless otherwise stated.

due to its high thermal conductivity and good machinability. The parts are gold plated to prevent surface oxidation and to improve heat transfer at the interface between different components. For a further enhancement of thermal coupling, braids and foils of oxygen free copper (OFHC) are used due to its superb thermal conductivity below 50K. Electrically isolating parts are made predominantly from glass-ceramic (Macor) or alumina, In cases where the heat conductivity is crucial (e.g. for sample and tip holder) sapphire is chosen. Table 3.1 summarizes important properties of the employed materials.

A photograph of the assembled microscope head mounted to the cold plate of the cryostat is shown in figure 3.10.

3.2.3 Sample Stage

The sample stage consists of the piezo actuators for three dimensional sample positioning, the mounting fixture for the exchangeable sample holder, and the high frequency transmission lines. The assembly of the sample stage is shown in detail in figure 3.11.

The home-built piezo positioners are based on the so-called slip-stick principle [160]; the moving part (slider) is clamped between shear piezo stacks, the clamping force can be adjusted by springs. If the piezos deform quickly in one direction they slip over the slider due to its high inertia, leaving its position virtually unchanged. For a sufficiently

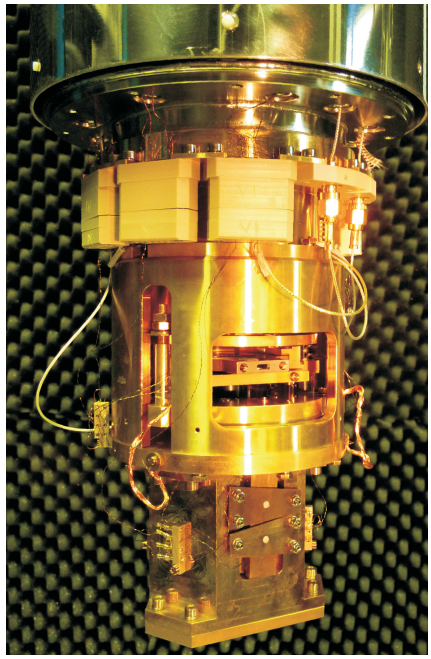

Figure 3.10: Photograph of the assembled microscope head mounted to the cryostat cold plate

slow deformation of the piezos they drag the slider with them. If a saw tooth voltage (typical frequency 100 -2000 Hz) with one fast and one slow ramp is applied to the piezos, the effect is a step by step motion of the slider in one direction.

The assembly of such a piezo actuator is exemplary shown for the z-positioner in the exploded view in figure 3.11 (a): the slider-part, depicted in green, is clamped between six piezo stacks in a triangular arrangement. The adjustable clamping force is generated by two CuBe leaf springs that press two of the piezo stacks onto the slider. The piezos are capped with alumina, while polished sapphire plates serving as sliding surfaces are glued onto the slider part. This results in a very low friction between the parts which is crucial for the slip-stick motion. Additionally, the hardness of sapphire and alumina makes the motor wear-resistant. Since sapphire and the piezo ceramic (lead zirconate titanate, PZT) have a considerable mismatch in the thermal expansion coefficient relative to bronze (compare table 3.1), there is a high risk that adhesive joints between this materials will fail during cooling. To prevent this, comb-like structures for thermal strain relief are machined into the bronze at the contact areas. The positioner provides a travel range of 15 mm and a step size around 50 nm. By applying a DC-voltage ($\leq$ 250 V) to the piezos a continuous motion within a range of $\sim$500 nm (2 μm) at 4.2 K (300 K) is generated.

On top of the z-slider the piezo positioner for the xy motion is mounted. The slider,

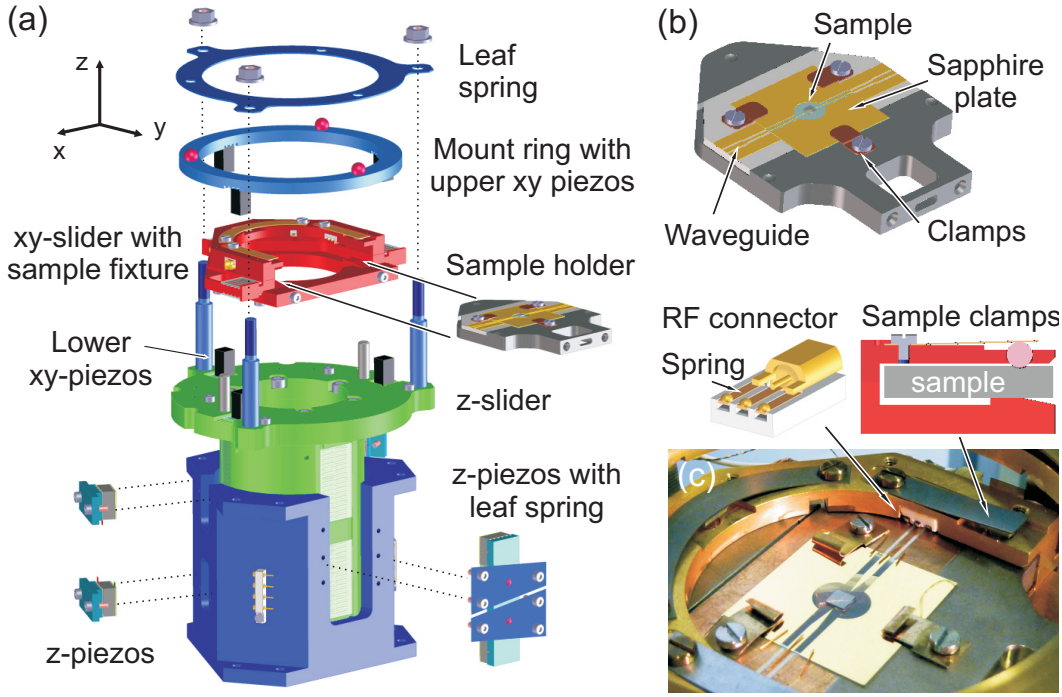

Figure 3.11: Assembly of the sample stage. (a) Exploded view revealing details of the piezo positioners; The z-slider is depicted in green, the xy-slider in red. (b) Sample holder with waveguide structures for experiments utilizing an objective lens. (c) Photograph of the sample holder mounted in the fixture. Schematically shown are the high frequency connectors and the clamping mechanism.

depicted in red in figure 3.11 (a), rests on three piezo stacks and is clamped by three additional piezos from the top. Its travel range is 5 mm in the x and y direction. The slider contains the mounting fixture for the exchangeable sample holder and the high-frequency contacts used to couple the microwave and RF signals into the sample holder waveguide.

The design of the sample holder is schematically depicted in figure 3.11 (b); a base part made from phosphor bronze or titanium supports a circuit board with a coplanar waveguide. In the center a thin plate ($\sim$ 170 μm thick) of sapphire with a similar waveguide is mounted by three CuBe clamps (the large misfit in thermal expansion coefficients prohibit the use of glue for the connection of sapphire and metal base part). The sapphire supports the actual sample, e.g. a diamond membrane. The high thermal conductivity of sapphire at low temperature enables an efficient cooling of the sample. High frequency access to the sample is realized by a microfabricated waveguide or a thin wire spanned over the surface. The different waveguides on the sample holder are

connected by wire-bonding. For handling the samples in the vacuum system the sample holder has an interface to the wobble stick transfer head. The sample holder shown in the figure is the version for experiments using an objective lens, the sapphire plate has a small aperture beneath the sample to provide direct optical access. For measurements using the parabolic mirror an adapted version is utilized which features a larger sapphire plate (diameter 40 mm) with smaller waveguides to limit shadowing.

To provide a mechanically stable mount for AFM experiments the holder is fixed in the xy-slider by the spring mechanism schematically shown in figure 3.11 (c): The sample holder rests on three pads in the sample stage, while it is clamped by three spring-loaded ruby balls. The ruby balls snap into dents in the sample holder, which provides a high reproducibility of the sample position.

The coupling between the waveguides on the sample holder and the transmission lines in the microscope head is realized by home-built spring-loaded contacts which are shown in figure 3.11 (c). They are assembled from commercially available MiniSMP connectors, a glass-ceramic body and three CuBe springs with Cu half spheres glued to it. The dimensions of these connectors as well as the waveguides on the sample holder are chosen to give a characteristic impedance close to 50 Ω to provide high microwave transmission and low reflections. From these spring connectors flexible coaxial cables lead to the cryostat mount plate where they are connected to the semi-rigid transmission lines through the cryostat.

3.2.4 AFM Unit

The AFM unit consist of coarse motors for the alignment of the AFM tip with the optical focus, the piezo scanner for fine motion of the tip in AFM measurements and the exchangeable tip holder carrying tuning fork sensor and tip. The assembly is shown in figure 3.12. Coarse positioning in the xy-plane is carried out by a home-built piezo actuators (travel range 3 mm) similar to the one used for sample movement. For coarse z-motion of the tip a commercial positioner (attocube ANPz51eXT) with 6.5 mm travel is employed. It works according to the slip-stick principle very similar to the home-built actuators and is mounted to the xy-slider. Fine scanning of the AFM-tip in three dimensions is carried out by a PZT piezo tube. Applying a DC voltage to segmented electrodes on the tube sidewall induces an axial elongation of the tube (i.e. tip motion in z-direction) or a bending corresponding to a tip displacement in the xy-plane. By that a resolution on the pm-scale within a scan range of approximately 1 μm at low temperature is reached.

To perform *in-situ* tip exchange, we designed a magnetic tip holder that provides a

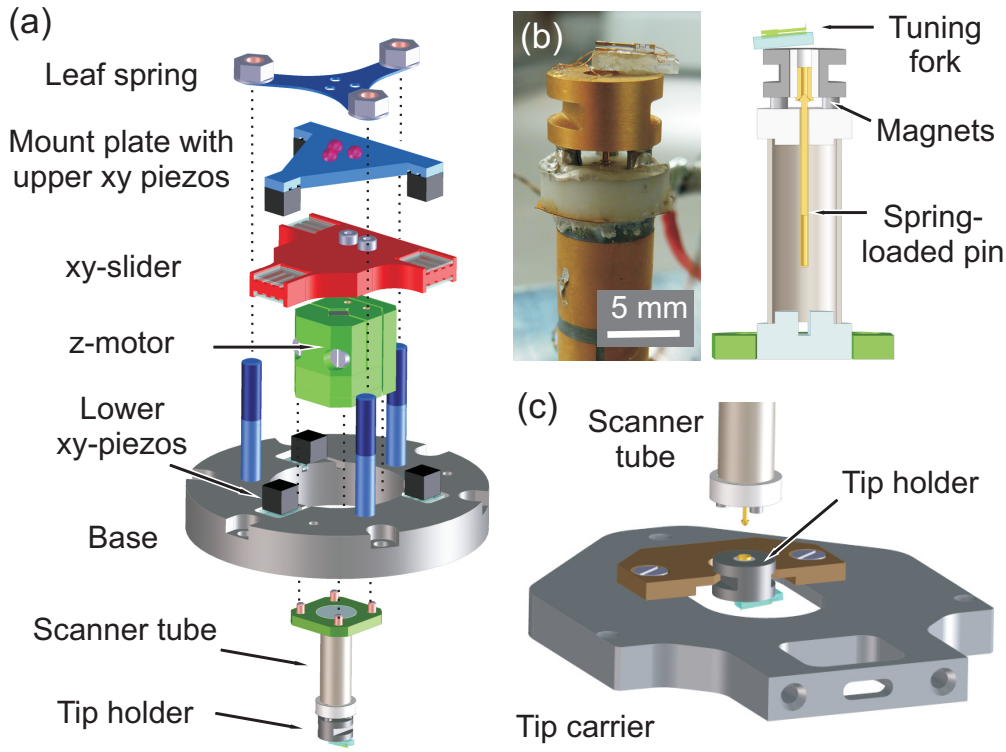

Figure 3.12: Assembly of the AFM unit. (a) Exploded view showing the xy-slider in red and the z-positioner in green. (b) Photograph and cross section of the scanner tube with the magnetic tip holder. (c) Tip carrier utilized for *in-situ* tip exchange.

rigid mechanical connection to the scan piezo and the two electrical contacts needed for the tuning fork excitation and readout. A photograph and a cross section view can be seen in figure 3.12 (b). The stationary part is glued to the piezo tube and consists of a glass-ceramic body with three CoSm magnets in a triangular arrangement around a central spring loaded pin. The exchangeable part is assembled from a gold-plated body of magnetizable steel and a central contact isolated by an alumina tube. The tuning fork, supported by a sapphire holder, is glued on top of the steel body. One electrode of the tuning fork is connected via the central contact to the spring-loaded pin in the piezo tube, the other one via the steel body to the magnets. The central pin and one of the magnets are contacted by wires inside the piezo tube. The force between the magnets and the magnetic steel piece is much stronger than the opposing force generated by the spring loaded pin, resulting in a rigid and reliable connection. For tip exchange, a modified sample holder with a specially designed tip mount is used. This tip carrier has an aperture in the center that fits the tip holder geometry as depicted in figure

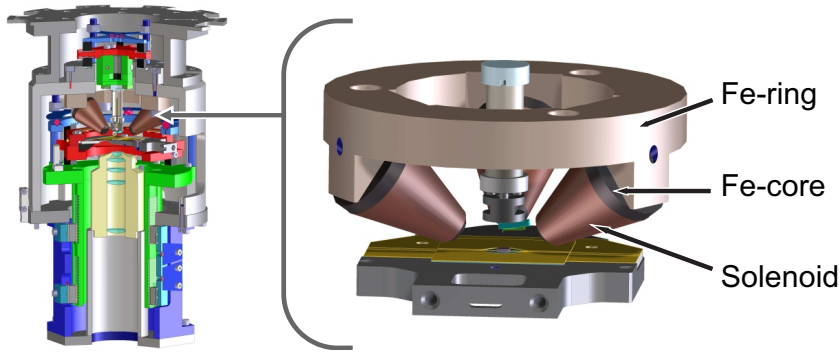

Figure 3.13: The vectormagnet consisting of three solenoids.

3.12 (c). For exchanging the tip, the carrier is moved in three dimensions such that the tip holder is locked in the carrier. The scan piezo can then be retracted while leaving the tip holder in the carrier. The mounting of fresh tips works in an analogous way; the conical pin in the piezo tube and the funnel-like shape of the central contact in the tip holder lead to a self-centering of the tip holder relative to the piezo tube.

3.2.5 3D Vectormagnet

If the parabolic mirror is not mounted there is free space inside the microscope head that can be used to install an electromagnet. The magnet consists of three solenoids arranged around the tip and the sample and oriented perpendicularly to each other, as shown in figure 3.13. This geometry enables tuning of the magnetic field strength and the field orientation in three dimensions by adjusting the current flowing through the individual solenoids. To enhance the field strength, the solenoid core and the ring-shaped holder are fabricated from high purity iron due to its high magnetic permeability. The solenoids consist of approximately 5000 loops of OFHC copper wire (0.1 mm thickness). The maximum achievable field strength is $\sim$ 5-10 mT for currents around 100 mA, for which no additional heating effects and only a negligible increase in the helium evaporation rate is observed.

3.3 Cryostat and vacuum setup

3.3.1 Cryostat

The cryostat consists of two stages with distinct base temperatures, depicted as blue (4.2 K) and green (77 K) parts in figure 3.14 (a). The inner part is comprised of a 9.6 l

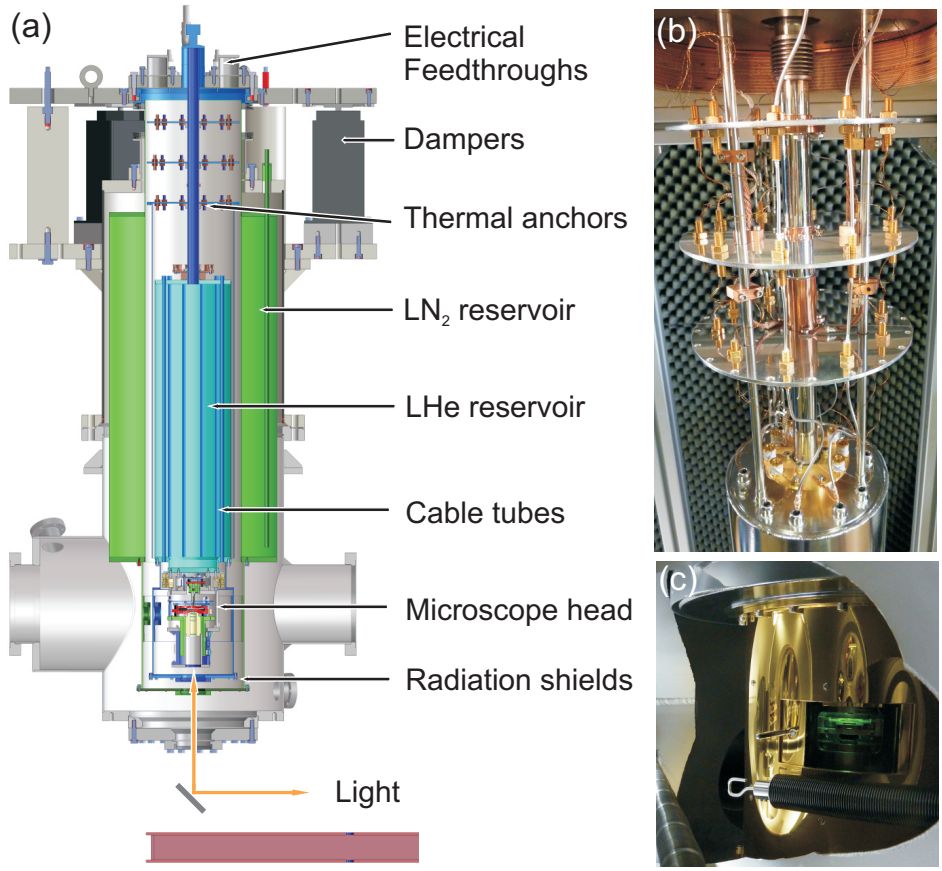

Figure 3.14: (a) Cross-section of the cryostat. In blue the insert cooled to liquid helium temperature is shown, green parts are cooled to 77 K. Optical access to the microscope head is realized by view ports in the vacuum chamber and radiation shields. (b) Photograph of the upper section of the cryostat insert showing the thermal anchoring of the wires. (c) Photograph of the radiation shields surrounding the microscope head. The green light stems from the laser illumination of the sample.

tank for liquid helium with a copper base plate where the microscope head is mounted. The head is surrounded by a radiation shield connected to the helium tank. The outer part consist of a circumferential liquid nitrogen reservoir (30 l) and a second radiation shield surrounding the microscope head. The whole assembly is integrated into an UHV chamber. For maintenance the inner part of the cryostat together with the microscope head and the wiring can be taken out via a flange on top of the setup.

The cryostat is fabricated predominantly from stainless steel, which is a poor thermal conductor (compare table 3.1). Due to this and the UHV surroundings, heat transfer to the environment is dominated by thermal radiation and thermal conduction through the electrical wires connected to the microscope head.

The former is suppressed by various baffles integrated in the cryostat assembly and by the two radiation shields surrounding the microscope head. These shields are made from gold plated copper and posses a shutter mechanism enabling sample and tip transfers. Figure 3.14 (c) shows a photograph of the radiation shields inside the vacuum chamber with the shutter opened. View ports in the bottom of the shields provide optical access to the front lens in the microscope head. To prevent a derogating affect on the performance of the confocal microscope we choose high-quality view ports made from fused silica with an broadband anti-reflection coating (525-975 nm) and a transmitted wavefront distortion of less than $\lambda/10$.

To minimize the heat transfer to the microscope head via the electrical connections, the wire materials have to be carefully chosen. In general there is always a trade-off between thermal and electrical conductivity; wires made from stainless steel or manganin (84 % Cu, 4 % Ni, 12 % Mn) feature a low thermal conductivity at the cost of a high electrical resistance. Copper wires on the other hand are good electrical conductors but pose a strong heat load to the microscope head. The best choice depends on the type of signal which has to be transmitted: piezo actuators require voltage pulses up to 250 V with fast rise times (on the ns-scale), therefore the resistance of the leads has to be low. Accordingly we choose bronze wires for the home built motors and Cu wire for the attocube positioner (which requires $R < 10\ \Omega$). For the microwave transmission lines semi-rigid coaxial cables with stainless steel shielding and an Ag-plated CuBe inner conductor are employed since they are a good compromise between damping at high frequencies (3.33 dB/m at 5 GHz) and thermal conductivity. For the tuning-fork and the z-piezo signals, which are sensitive to electrical noise, stainless steel coaxial wire is used. The remaining, less sensitive signals (temperature sensors, preamplifier connections, etc.) are transmitted via manganin twisted-pair wires.

The heat transfer to the microscope head through the wires is additionally reduced by thermal anchoring. All electrical leads are connected via UHV feedthroughs in the top flange of the cryostat insert and subsequently coupled to the three baffles between the top flange and the helium tank (see figure 3.14 (a) and (b)). For an effective thermal coupling the wires are glued with silver epoxy into copper tubes attached to the baffles. Additionally the cables are wound around copper bobbins mounted on top of the helium tank and subsequently guided through tubes in the tank to the microscope head. The semi-rigid cables (which cannot be wound) are thermalized by copper braids.

The thermal shielding of the cryostat insert and the optimized wiring result in a base temperature of 4.7 K and a standing time of the cryostat of roughly 6 days, corresponding to a liquid helium consumption of 1.4 l/day or an heat introduction of 42 mW. However,

extensive laser and high frequency excitation can strongly affect this standing time, which will be discussed in section 4.5.

3.3.2 UHV Setup

The vacuum setup consist of two chambers that are separated by a gate valve and can be independently pumped to a base pressure on the order of 10^{-10} mbar. The main chamber contains the cryostat and the microscope head; the load-lock chamber is used for introducing samples and tips into vacuum (without venting the main chamber) and sample preparation. Samples and AFM tips can be moved with a mechanical transfer mechanism between both chambers. A model of the complete system can be seen in figure 3.15.

Both chambers are equipped with a combination of vacuum pumps covering different pressure ranges. Membrane pumps are used to evacuate the system from ambient pressure down to a few mbar and to generate the pre-vacuum for the turbomolecular pumps. These turbomolecular pumps feature an integrated Holweck stage and can thereby operate in a pressure range from 10 down to 10^{-8} mbar. Starting from a pressure below 10^{-6} mbar, ion pumps are employed to pump the system to the base pressure of 10^{-10} mbar. Since ion pumps, in contrast to turbomolecular pumps, do not posses moving parts and thus do not cause vibrations, they are typically the only pumps running during AFM measurements. The main chamber is furthermore equipped with a titanium sublimation pump (which periodically evaporates titanium to chemisorb gas molecules) and a mass-spectrometer for residual gas analysis.

Samples and tips can be transferred between the chambers by a magnetically coupled linear transfer rod. The transfer head mounted to the rod features an integrated heater stage that enables sample annealing up to 130°C. In the main chamber samples and tip carriers can be handled by a wobble stick and transferred into the microscope head or into a magazine. Here up to seven samples or tips can be stored under UHV conditions. A scheme of the sample transfer in the system is depicted in figure 3.15 (b). The load-lock chamber is equipped with ports for Knudsen cell evaporators and leak valves enabling sample preparation and molecule deposition.

The vacuum system is supported by a rigid frame constructed from aluminum strut profiles. Underneath the main chamber, an optical breadboard for the confocal microscope is integrated in this assembly (see figure 3.15 (a)). The excitation and fluorescence light is transmitted through a view port mounted in the base of the vacuum chamber. It features a transmitted wavefront distortion of less than $\lambda/4$ (the best value available due to the pressure difference acting on the window) and an anti-reflex coating in the

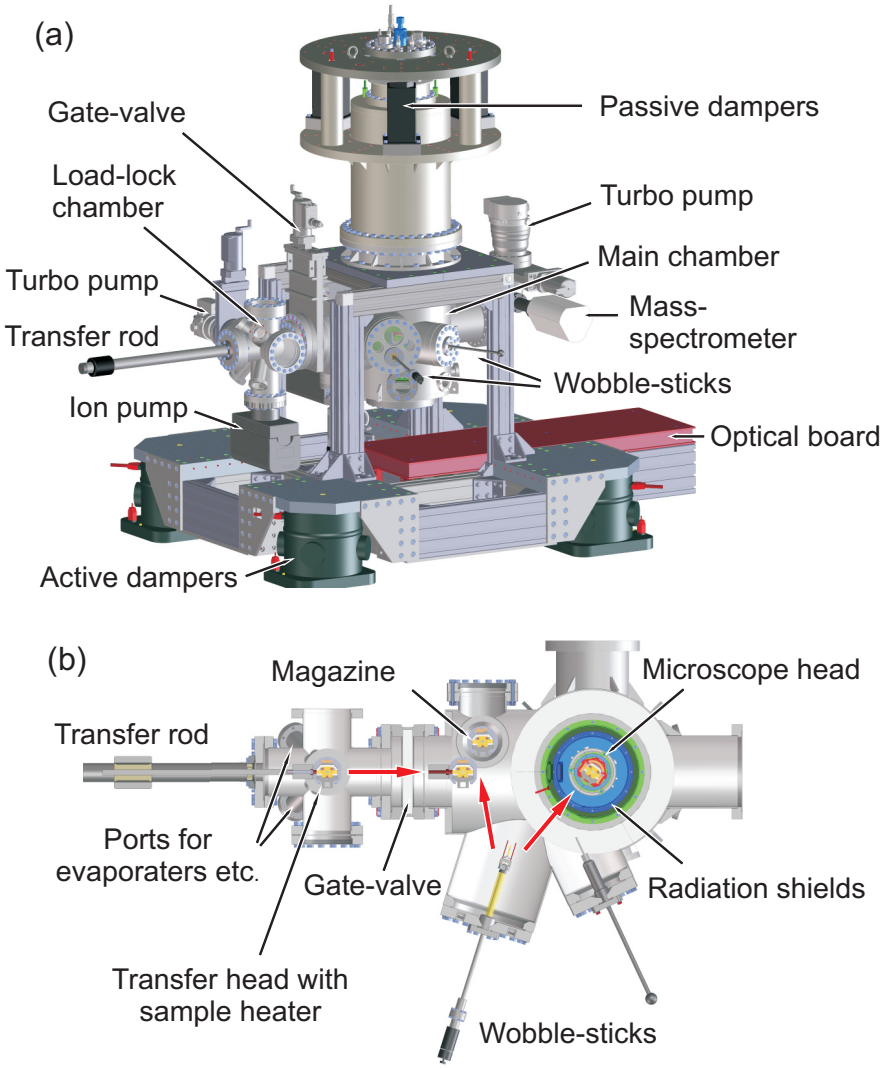

Figure 3.15: (a) Model of the vacuum system. (b) Horizontal cross-section trough the system revealing the sample transfer system.

wavelength range 425-760nm to minimize optical aberrations and transmission losses.

3.3.3 Vibration Isolation

To achieve sub-nm resolution in AFM experiments a low vibration level of tip and sample has to be achieved. Mechanical vibrations in the environment are typically in the low frequency range of 1 - 500 Hz and comprise, for example, building vibrations ($\sim$ 1-20 Hz), floor vibrations induced by vacuum pumps ($\sim$ 10-300 Hz), or acoustic noise. As already mentioned, the microscope head and the frame of the vacuum setup are designed for high stiffness, resulting in high resonance frequencies and thus a weak

coupling to these vibrations. Additionally the system is equipped with a combination of vibration damping elements. Piezo-based active dampers (TMC Stacis 2100) at the base of the machine decouple the system from vibrations in a frequency range of 0.6-100 Hz, while passive pneumatic dampers (Newport I-500) between the UHV-chamber and the cryostat insert (see figures 3.15 (a)) suppress efficiently higher frequency vibrations (>10 Hz).

Chapter 4

Instrument Performance

The different sub-systems of the experimental setup have been extensively tested and optimized for operation at low temperature in UHV. In the first three sections of this chapter we present benchmark measurements characterizing the performance of the optical imaging system, the high frequency setup and the atomic force microscope. Section 4.4 demonstrates the combination of all techniques to enable magnetic resonance imaging of nanoscale magnetic fields. These measurements utilizing the scanning field gradient technique are the first realization of NV magnetic imaging at low temperature. Of particular importance for the projected experiments is the achievable sample temperature and how this is affected by laser and high frequency irradiation. Since the actual temperature in the probed sample region is not accessible by conventional sensors, we utilized a novel approach based on optical spectroscopy to address this issue. This method is described in the last section 4.5 along with a discussion of the various sources of dissipative heating in the cryostat.

4.1 Optical Imaging

Optical imaging can be carried out by confocal microscopy using either a parabolic mirror or an objective lens as light collecting and focusing element. Since it was not *a priori* clear which approach provides the better performance at low temperature, we carefully tested both elements.

Parabolic Mirror

Parabolic mirrors in the required size and quality are not commercially available, therefore we got a prototype fabricated from the Fraunhofer Institute for Applied Optics (IOF). The mirror has a diameter of 30 mm, a focal length of 6.75 nm and a NA close

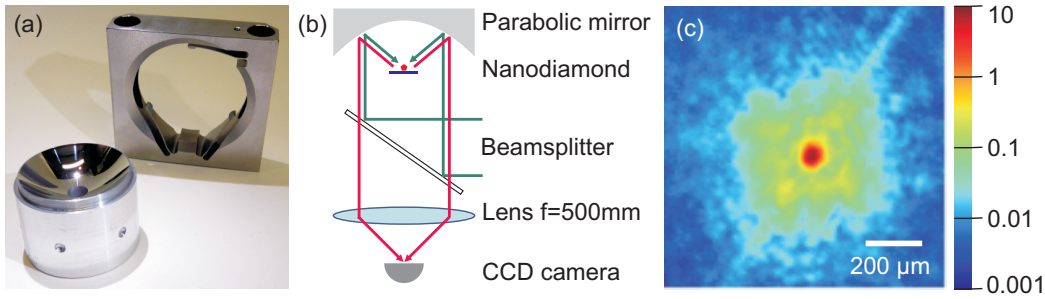

Figure 4.1: (a) Photograph of the Parabolic mirror prototype with its kinematic holder. (b) Scheme of the experimental setup for the mirror test. (c) Image of a nanodiamond obtained with the parabolic mirror setup.

to 1. A 5 mm diameter bore along the mirror axis enables access to the focal region with the AFM tip. The mirror is manufactured from an aluminum alloy with a layer of nickel-phosphorous that allows precise polishing with nm-accuracy. The materials are thermal expansion-matched to prevent deformation at low temperatures. The high-precision machining was achieved by diamond turning with deviations from an ideal parabola shape expected to be less then $\lambda/4$ over the full surface. Furthermore the IOF designed and fabricated a kinematic mirror holder which provides a stable mount over a wide temperature range without deforming the mirror. Figure 4.1 (a) shows a photograph of the mirror prototype and the kinematic mount.

We tested the mirror under ambient conditions with a sample of nanodiamonds dispersed on a diamond substrate. The green excitation laser is focused by the parabolic mirror onto the sample, the fluorescence light is collected by the mirror and focused onto a CCD camera by a f = 500 mm lens (see figure 4.1 (b)). After careful alignment of all components, fluorescence images of single nanodiamonds such as the one shown in figure 4.1 (c) can be obtained. Since the nanodiamond (diameter ∼150 nm) is a sub-wavelength emitter, this image can be interpreted as the lateral point spread function (PSF) of the optical system, where the nominal magnification was $M \approx 75$. The broad intensity distribution indicates a poor focusing of the parabolic mirror. As discussed in section 3.2.1, this results in a large background signal generated from the surrounding of the NV, leading to a poor signal-to-noise ratio in single NV experiments, and the need for high excitation power causing laser heating. The poor focusing of the mirror is probably related to phase errors caused by imperfections in the parabolic shape [161]. These mirror imperfections and the tedious alignment, which is expected to be even more difficult in the low temperature vacuum setup (owing to the limited access, additional elements in the beam path (view ports) and the vibration dampers between the cryostat

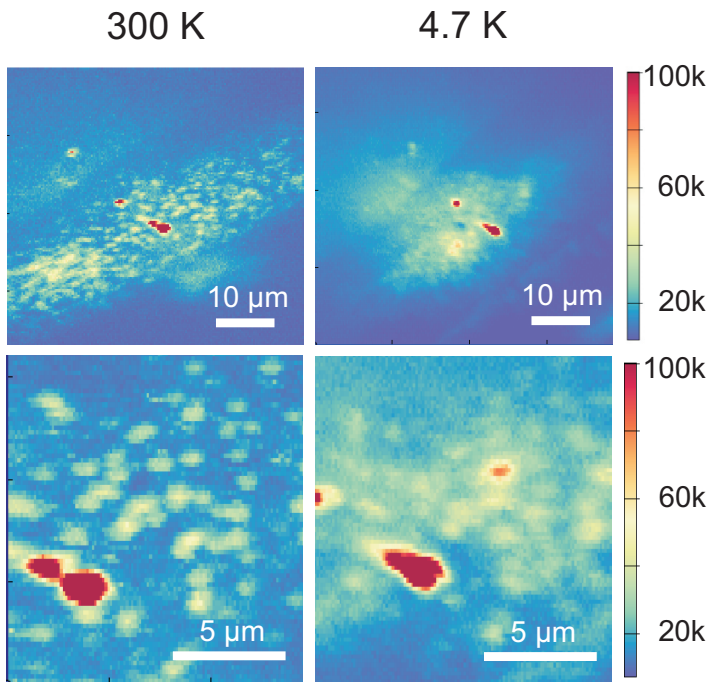

Figure 4.2: Confocal images of single NV centers obtained with the Partec objective lens in the vacuum setup at room temperature (left) and at 4.7 K (right).

insert and the optical setup), are strong obstacles for the further use of the mirror in low temperature experiments.

Objective Lens

As objective lens we used a Partec lens with a numeric aperture of 0.82 and a working distance of 0.4 mm, which offers to our knowledge the best low temperature performance among the available cryo-compatible (i.e. withstanding cooling to liquid helium temperature without severe damage) objective lenses. However, since its lens system is not optimized for low temperature operation, the cooling reduces the image quality (as discussed in section 3.2.1). Furthermore, its room temperature performance is worse compared to higher quality objective lenses due to its relatively simple lens assembly without cemented doublets. Figure 4.2 show confocal images of the same NV centers in a bulk diamond acquired at room temperature and at liquid helium temperature, respectively. At low temperature, the images are clearly blurred, making it difficult to resolve the individual NV centers and leading to a higher background count rate. Also the field of view (imaging is carried out by laser beam scanning) is strongly reduced at

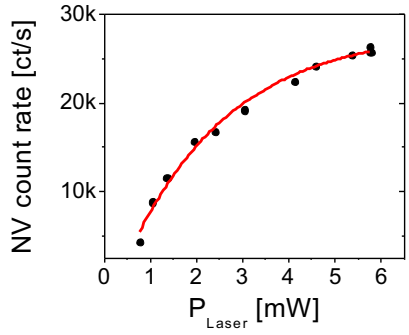

Figure 4.3: NV count rate as a function of excitation laser power, measured at 4.7 K in UHV.

4.7 K which is probably due to an insufficient correction of lateral chromatic aberrations for larger field angles and thus a divergence of excitation and detection focus [147].

The saturation curve depicted in figure 4.3 reveals a maximum signal strength for a single NV center of ∼30 kcts/s at 4.7 K. This value is significantly lower than the approximately 100 kcts/s obtained with higher quality air objective lenses under ambient conditions (∼300 kcts/s for commonly used oil immersion lenses), but corresponds well to values reported for low temperature experiments [162]. Correspondingly, the excitation power needed for saturation is approximately a factor of 10 larger than values reported for room temperature experiments [73]. Both facts indicate that the focusing of the objective lens is severely degraded by uncompensated aberrations at low temperature. The performance loss at low temperature is reversible and is found to be reproducible even after several thermal cycles between 4.7 K and 400 K, thus no permanent damage induced by thermal strain occurs. However, we noticed temperature dependent birefringence (rotation of the polarization of the transmitted light) which is probably caused by stress resulting from the thermal expansion mismatch between the lens material and the brass mounts [148] (see figure 3.5).

Conclusion

In spite of the performance loss at low temperature the objective lens offers the better imaging performance than the parabolic mirror prototype. Compared to experiments under ambient conditions, the NV density in the sample has to be sufficiently low to resolve single NV centers due to the blurring at low temperature and longer averaging times are needed in ODMR-experiments owing to the low count rates. Additionally, the poor focusing make the imaging system more sensitive to background fluorescence by

contaminations. However, the demonstrated imaging performance enables the detection of single NV centers at low temperature with a sufficient signal-to-noise ratio for ODMR-measurements.

4.2 ODMR Measurements

Optically detected magnetic resonance of single NV centers requires spin manipulation by microwave pulses with ns time resolution and an optical NV read-out with high sensitivity. To demonstrate the performance of the setup we carried out different magnetic resonance experiments on the single spin level.

Basic ODMR

The basic ODMR experiments presented in the following are performed at 4.7 K in UHV on single NV centers in a 20 μm thick diamond membrane. The implantation energy was 5 keV resulting in a NV depth of 8 $\pm$ 3 nm below the surface [42]. A small magnetic field is applied by mounting a permanent magnet instead of the the AFM tuning fork to the tip holder. Control of the field strength, as well as a crude alignment of the field orientation with respect to the NV axis, is achieved by coarse positioning the magnet with the piezo actuators of the AFM unit. Figure 4.4 (a) shows typical cw-ODMR spectra for two magnetic fields. The spectra show the two $|m = 0\rangle \rightarrow |\pm 1\rangle$ transitions with a symmetric splitting around $D = 2.87$ GHz that increases with larger fields. The different transition strength of the two lines, especially in the case of the larger magnetic field, is probably related to a certain misalignment of the external field in combination with the linear polarization of the MW driving field [99].

Figure 4.4 (b) depicts Rabi oscillation with a frequency close to 10 MHz, which are driven by transmitting a microwave signal of a few mW power through the sample stripline. The generated AC field (roughly 60 μT for the measurement shown) enables the manipulation of spins at a distance of up to $\sim$ 50 μm from the stripline. In these pulsed experiments a spin state contrast of 20 % is typically achieved, which is limited by the signal-to-noise ratio of the optical read out.

A typical spin echo of a shallow NV center is shown in figure 4.4 (c). The collapse and subsequent revival of echo signal is induced by the interaction between the NV and the C^{13} nuclear spin bath (see section 2.2.2). Due to the rather slow C^{13} Larmor precession (B $\approx$ 9 mT) and the limited T_2 only a single revival is expressed in the measurement. The T_2 times of the shallow NV centers in the studied sample are typically 3 - 20 μs as

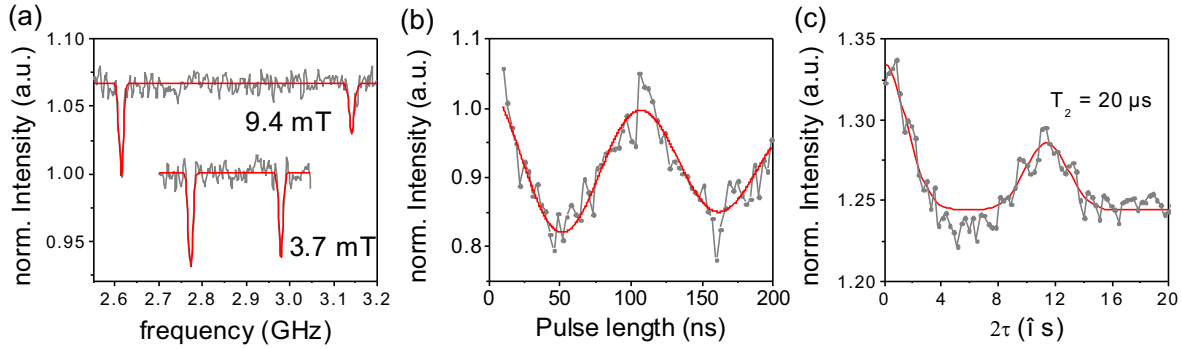

Figure 4.4: (a) cw-ODMR spectra. (b) Rabi-oscillations. (c) Spin-echo. All data is measured on single NV centers in a diamond membrane at 4.7 K.

a consequence of their proximity to the diamond surface and the related impurities and defects.

Dynamic Decoupling

To overcome the limitations of the short T_2 we employed dynamic decoupling protocols. As discussed in section 2.2.3, the efficiency of the decoupling depends on the properties of the spin bath environment as well as on the fidelity of the spin manipulation. We used XY-n sequences due to their intrinsic compensation of pulse errors. Figure 4.5 shows a comparison of the normal spin echo and a XY-8 sequence for an shallow NV center at 4.7 K (the sample was the same as in the previous section). Each pulse sequence was measured with a final $\pi/2$ and $3\pi/2$ pulse (marked with * in the figure), respectively. This corresponds to a projection onto the bright and the dark eigenstate, resulting ideally in two horizontally mirrored decay curves. The normal spin echo decays with a short time constant of $\sim$ 3 μs, while the XY-8 sequence generates a detectable signal even after 15 μs. Thus, dynamic decoupling increases the coherence time at least by a factor of five for the investigated sample system. The spin echo reveals a modulation with an apparent period of 650 ns, corresponding to a modulation frequency of 3 MHz (a factor of 2 has to be introduced to account for the two free evolution periods in the spin echo sequence). This ESEEM-effect can be attributed to interactions of the NV spin with the N^{15} nuclear spin [163, 164]. The same interaction appears in the XY-8 experiment as pronounced dips (peaks for XY-8*) at T= 2.4 μs and T= 7.5 μs, such that Δ T/n $\approx$ 650 ns.

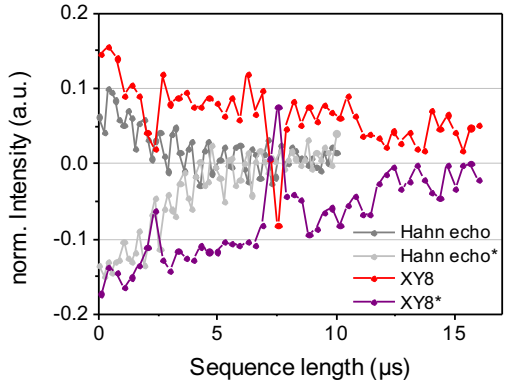

Figure 4.5: Comparison of Hahn echo and XY8 sequence for a shallow NV at 4.7 K.

Double Resonance

To demonstrate the indirect detection of 'dark' spins via the NV center, we carried out double resonance experiments using a SEDOR-sequence. The sample was a 1b diamond crystal, where the high nitrogen concentration ($\sim$ 200 ppm) creates an electron spin bath interacting with the NV center. The measurements were performed in an external magnetic field of $\sim$ 3 mT. Figure 4.6 (a) shows a NV spin echo with and without manipulation of target spins. The additional RF pulse in the middle of the pulse sequence drives the electron spin bath, which reduces the NV center coherence time. The spectrum of the spin bath is measured by sweeping the RF frequency while monitoring the NV spin echo amplitude. The resulting spectrum is depicted in figure 4.6 (b), the plotted signal represents the difference of spin echo amplitude measured with and without RF pulse for a evolution time of $2\tau = 3\ \mu s$. A peak around 93 MHz is evident, which fits well to the Larmor frequency of a free electron spin ($\sim$ 28 MHz/mT) in the applied magnetic field. Although no hyperfine structure is observed and thus an unambiguous identification of the detected spin species is difficult, the most likely candidate is the paramagnetic nitrogen impurity (referred to as P_1 center) due to its high abundance in 1b diamond [165].

Coherent control of the spin bath can be achieved by applying RF pulses at the resonance frequency. Figure 4.6 (c) shows the NV echo amplitude as a function of pulse length for two different RF powers. The periodic revivals with a frequency increasing with RF power are the key signature of coherently driven Rabi oscillations of the target spins. While in principle the coherent manipulation of the spin bath enables more sophisticated control sequences such as spin echo, the rather short NV coherence time limiting the maximum sequence length precludes these experiments.

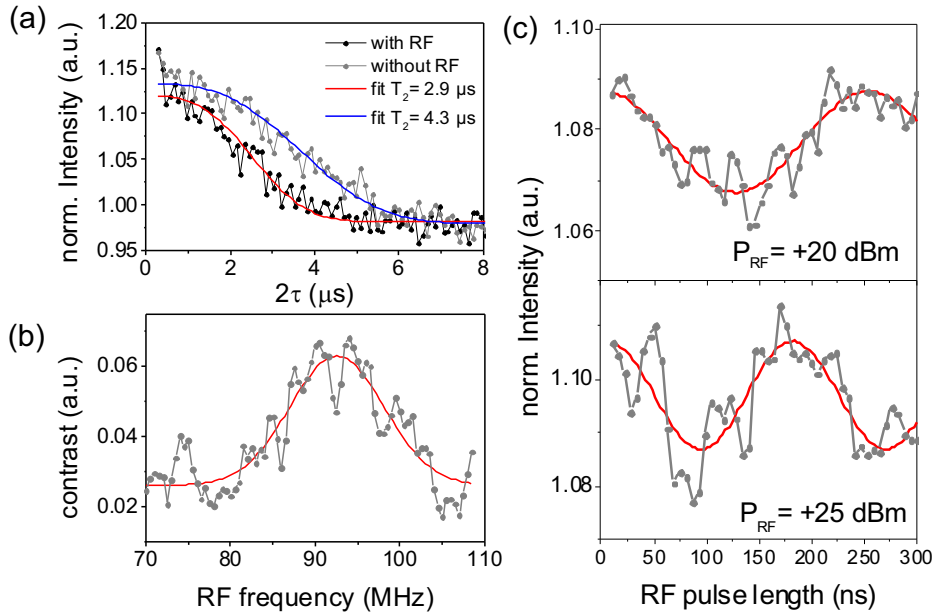

Figure 4.6: (a) Spin echo with and without applied RF pulses. (b) DEER spectrum (c) NV spin echo intensity as function of RF pulse length.

Conclusion

The high frequency access to the sample enables the manipulation of the NV spin as well as potential target spins with driving powers corresponding to 10 MHz Rabi frequency; complex pulse sequences required for dynamic decoupling and double resonance can be realized by the control electronics. The sensitivity of ODMR on single spins at low temperature is primarily limited by the signal-to-noise ratio of the optical read out. The question of HF-field induced heating is addressed in section 4.5.

4.3 Atomic Force Microscopy

The AFM performance was tested under ambient and cryogenic conditions with various sample systems and with different tips mounted to the tuning fork sensor (stiffness k = 1800 N/m). The measurements presented in the following were carried out with a commercially-available silicon tip, which we transferred to the tuning fork sensor with a micromanipulator. For the all-electrical excitation and read-out of the tuning fork the electric circuit depicted in figure 4.7 is used. The small current signal generated by the tuning fork ($\sim$ pA) passes through a transimpedance-amplifier (gain 10^8) based on an AD827 operational amplifier and mounted in the microscope head. This enables

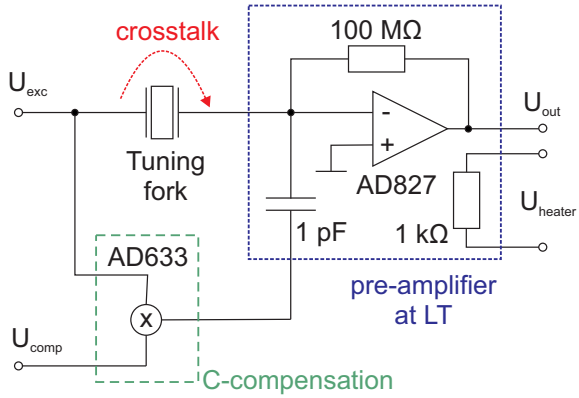

Figure 4.7: Schematic of the all-electrical excitation and read-out of the tuning fork signal.

a short connection to the tuning fork, which is crucial for a high signal-to-noise ratio. Since the silicon-based operational amplifier is not working at liquid helium temperature (charge carriers in silicon are frozen out at this temperature), the chip is heated by a small 1 kΩ resistor glued onto the device. Our tests indicate that a device temperature of 77 K is sufficient for proper operation, which requires a heating power of $\sim$ 25 mW (heat current $\sim$ 5 mA) when the microscope head is at liquid helium temperature. The electronic noise on the amplified signal is found to be dominated by thermal noise of the R= 100 MΩ feedback resistor (Johnson noise density $n_R = \sqrt{4k_BTR}$), thus cooling the preamplifier to the lowest possible temperature enhances the signal quality.

As the tuning fork is excited directly by applying the driving voltage to one of its electrodes, the parasitic capacitance between its electrodes (and the attached wires) leads to a crosstalk between excitation and detection channel. This reduces the Q-factor and thus the sensitivity of the tuning fork sensor and manifests itself in an asymmetry of the resonance curves (i.e. a Fano-lineshape instead of an Lorentzian). We compensated the effect of the parasitic capacitance by an approach similar to the one reported in [166] by driving an additional capacitor parallel to the tuning fork with an inverted signal. We employ an analog multiplier (AD633) to create the inverted excitation signal with adjustable amplitude (see figure 4.7). The crosstalk-signal is phase shifted by 90° compared to the excitation signal, while the multiplier in combination with the second capacitor creates a 270° phase shift (180° + 90°). Thus, both signals cancel each other out when the amplitude of the compensation signal is chosen properly, resulting in symmetric resonance curves as shown in figure 4.8.

The Q-factor of the tuning fork resonance increases by orders of magnitude when going from ambient conditions to UHV and low temperature due to the reduced me-

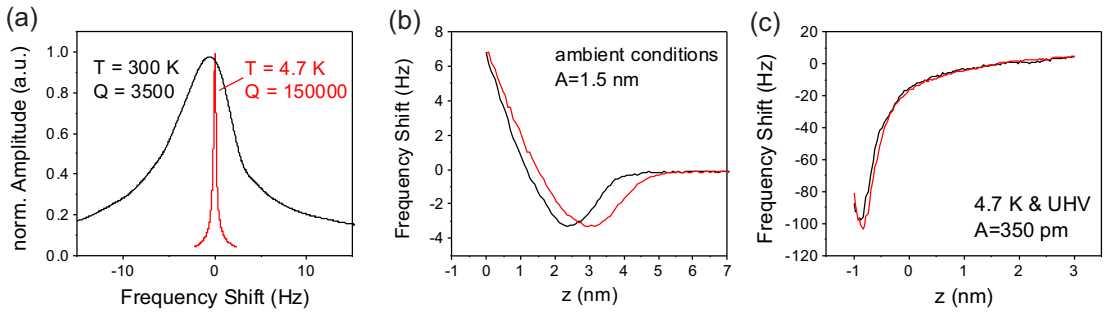

Figure 4.8: (a) Tuning fork resonance at 300 K (black) and 4.7 K (red). The center frequency is around $f_0 = 30$ kHz. (b) Approach-retract curves of a Si-tip on a Au surface under ambient conditions. (c) Approach-retract curves on HOPG in vacuum at 4.7 K.

chanical damping of the oscillation (see figure 4.8). The high Q-factor enables a very sensitive frequency detection and therefore less noise in the FM-feedback. Furthermore, smaller oscillation amplitudes ($\sim$ 1 Å) are possible at low temperature in UHV, which results in an increased sensitivity to short-range forces and therefore a higher spatial resolution. This is demonstrated by the approach-retract curves in figure 4.8 (b) and (c) depicting the frequency shift as a function of tip-sample distance. The curve in 4.8 (b) is obtained on a gold surface with a silicon tip under ambient conditions using an oscillation amplitude of 1.5 nm. It reveals tip-sample interactions over a rather long distance range ($\sim$ 5 nm) with both attractive and repulsive force regimes. These are attributed to van der Waals interaction and electrostatic forces (attractive) and Pauli repulsion [131]. The hysteresis between tip approach (black curve) and retraction (red) is probably caused by the water film on the sample, which is always present under ambient conditions. The curve in 4.8 (c), obtained with a silicon tip on *in-situ* cleaved highly-ordered pyrolytic graphite (HOPG) at 4.7 K in UHV, reveals almost no hysteresis (no water film on the sample) and much steeper slopes for small tip-sample distances; since the oscillation amplitude was only 350 pm in this measurement, the tuning fork is more sensitive to strong short-range interactions such as chemical forces, resulting in a large frequency shift close to the sample. The steep slope in this regime allows a precise control of the tip-sample distance during scanning, and the short-range nature of the probed interactions enhances the lateral resolution.

To benchmark the imaging performance of the AFM we investigated a gold film on glass cleaned by flame annealing under ambient conditions and subsequently introduced into the vacuum system. The flame annealing of polycrystalline Au films is known to yield relatively large terraces with (111) orientation [167]. Imaging is carried out in

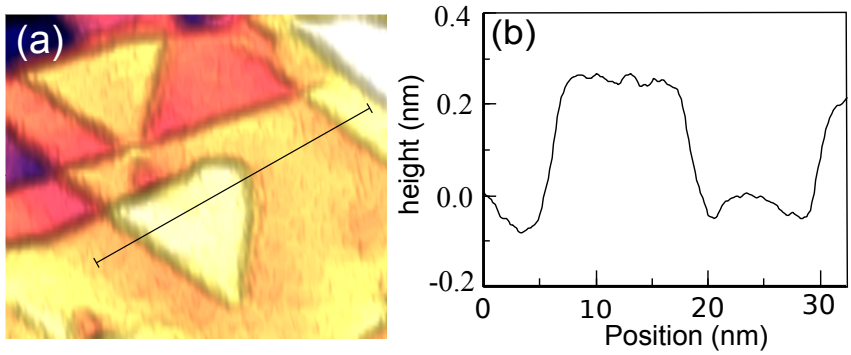

Figure 4.9: (a) AFM topography of Au on glass. (b) Line profile.

the non-contact regime with frequency modulation feedback, an oscillation amplitude of 1 nm and a set point of Δf = -6 Hz (free oscillation frequency f_0 = 30300 Hz). The topography image depicted in figure 4.9 (a) reveals terraces with triangular structure and mono-atomic steps with height $\sim$ 2.4 Å in good agreement with previous observations on Au(111) (e.g. [168]). The z-noise during scanning is approximately 20 pm (peak-peak) in the bandwidth of 1-100 Hz, verifying the high mechanical stability of the setup. Lateral atomic resolution is precluded by the sharpness of the employed silicon tips but could probably be reached with metal tips in combination with *in-situ* tip forming techniques. However, since the AFM is used in the envisaged experiments predominantly for positioning of the target or sensor spins rather than high-resolution imaging, we did not follow this approach.

Conclusion

Stable AFM operation can be reached under ambient conditions as well as in UHV at liquid helium temperature. The sensitivity and resolution improves at cryogenic conditions due to a higher quality factor and smaller achievable oscillation amplitudes such that a vertical resolution below 1 Å is obtained. The demonstrated performance enables experiments on the single molecular level.

4.4 Combined Experiments

To carry out combined optical and AFM measurements, the sample has to be transparent and thin enough to focus the light on (and collect fluorescence from) the top surface while the objective lens is located underneath the sample. Moreover, optical focus, AFM

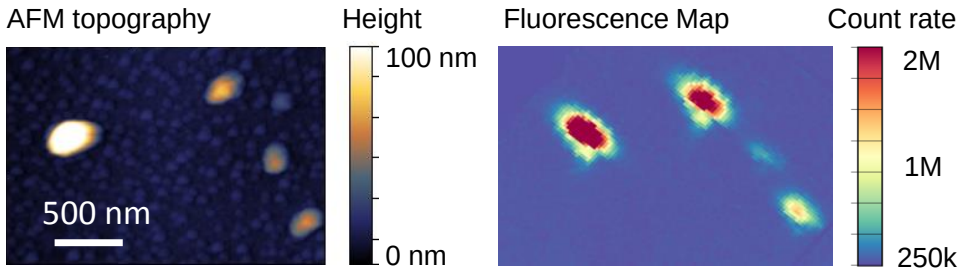

Figure 4.10: AFM topography and fluorescence map of nanodiamonds dispersed on a glass slide.

tip, and sample have to be positioned relative to each other with sub-μm accuracy. The first section briefly describes the corresponding alignment procedure. In section 4.4 we utilize the combination of ODMR spectroscopy and AFM to demonstrate nanoscale magnetic resonance imaging via the scanning gradient technique. This method, which has so far been used only at ambient conditions, enables not only magnetic field imaging, but could also be extended to map target spin with nanometer resolution [18].

Alignment of AFM and confocal microscope

The positioning of the AFM tip in the optical focus of the confocal microscope (lateral extension ∼300 nm) is a non-trivial task due to the limited scan ranges of both microscopes and the restricted access in the cryostat. The first step is a coarse alignment 'by eye' using a video camera with high magnification optics (looking through windows in the UHV chamber and radiation shields) and positioning of the AFM tip with the piezopositioners. If the sample shows features that can be correlated in the AFM and confocal image, this first step is often precise enough to determine the tip position relative to the optical scan frame. An example for this is shown in figure 4.10, where confocal image and AFM topography of nanodiamonds dispersed on a glass slide are depicted. Clearly, both images show the same structures.

While figure 4.10 is measured at room temperature, this image correlation is more difficult at low temperature; since the piezo constants are reduced approximately by a factor of 4 between 300 K and 4.2 K, the AFM scan range at low temperature is only ∼ 1.5 μm in the lateral directions, which is only slightly larger than the optical resolution. Thus, finding the same structures in both micrographs is difficult. Moreover, sample systems like diamond membranes do not show any correlation between fluorescence and topography. In this case, the alignment has to be carried out via the excitation light back-scattered by the tip into the objective lens.

If the tip is positioned in the laser focus it absorbs a certain fraction of the power, depending on the tip material. With silicon tips, this results in a considerable heating and correspondingly a thermal expansion of the tip by a few nm, which is compensated by the AFM feedback control. That leads to a crosstalk of the focus position and the z-channel of the AFM, which can also be used to locate the tip position within the optical scan frame.

Scanning-field-gradient Imaging

To demonstrate the interplay of confocal microscopy, magnetic resonance spectroscopy and atomic force microscopy we performed scanning-field-gradient MRI. This technique employes the strong field gradient created by a magnetic AFM tip to spatially resolve the magnetic resonance signal; using this technique, Grinolds *et. al.* localized spins under ambient conditions with nanoscale resolution in three dimensions [18, 169].

We carried out these experiments at 4.7 K on the 20 μm diamond membrane containing shallow NV centers. A scheme of the experiment is depicted in figure 4.11 (a): The magnetic tip is scanned over the NV center close to the diamond surface, while simultaneously a microwave field with a constant frequency close to the NV resonance frequency is applied. We used a commercially available magnetic tip commonly used for MFM experiments, which produces a field gradient on the order of $5 \cdot 10^{-2}$ mT/nm [16]. Due to this gradient, the field at the NV position and therefore the resonance frequencies depend strongly on the tip position. When plotting the NV fluorescence as a function of tip position, areas where the applied microwave is on resonance with the NV appear dark. Figure 4.11 (b) shows two overlaid fluorescence maps measured with different microwave frequencies. The structures in the fluorescence map can be interpreted as equipotential lines of the magnetic field created by the tip. For a radially-symmetric field the lines form ring-like structures centered around the NV spin [16, 169]. The diameter depend on the microwave frequency; for larger microwave detunings a stronger field is required to tune the NV center into resonance and correspondingly the ring diameter becomes smaller. This effect can be qualitatively seen in the presented measurements; however, the field distribution deviates from the expected symmetric shape and reveals a rather complex structure, presumably because the tip apex is composed of different magnetic particles or domains.

If the AFM tip is scanned through the laser focus, optical near-field effects lead to a variation of the fluorescence count rate depending on the tip position. These effects tend to cover the spin resonance effect and therefore have to be removed from the signal. For the measurements presented above we achieved this by acquiring the fluorescence data

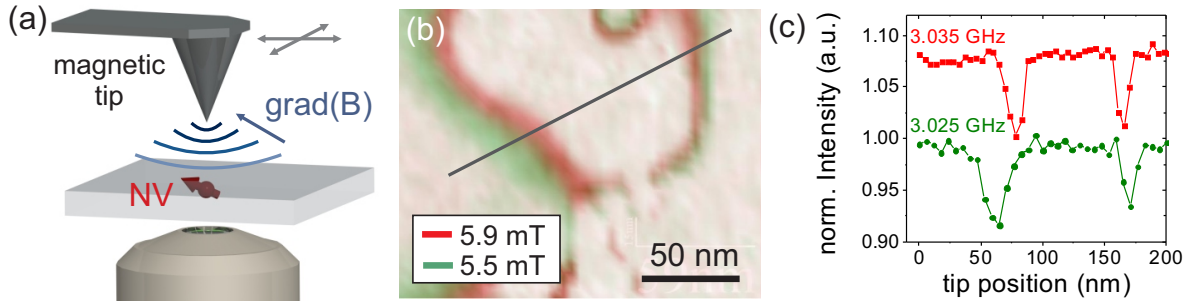

Figure 4.11: Scanning-field-gradient MRI. (a) Measurement schematics. (b) NV fluorescence intensity as a function of tip position. The image is an overlay of two subsequent scans with 3.025 GHz and 3.035 GHz microwave irradiation. (c) Line section through the measurements in (b).

in every pixel of the scan with and without applied microwave and therefore obtained two distinct fluorescence maps. The near-field effects are present in both maps, while the spin resonance is only detected in the data-set measured with applied microwave. The subtraction of both images yield the image presented in figure 4.11 (b).

The acquisition time per pixel was around 20 s, thus a complete scan took a few hours. Figure 4.11 (b) is composed of two images taken more than 6 h apart and overlaid with each other without further modifications. The fact that no lateral drift is obvious in the image even though laser excitation and strong microwave pulses are applied demonstrate the high long-term stability of the system.

Conclusion

The combination of optically detected magnetic resonance and atomic force microscopy requires transparent and thin samples and a careful alignment of the optical focus and AFM tip. The laser irradiation and high frequency fields influence the AFM-feedback due to local heating and corresponding thermal expansion of the tip, but since this effect is slow compared to the time scale of the AFM feedback a stable AFM operation can be maintained. We demonstrated scanning-field-gradient MRI at low temperature, which can be used in future experiments to spatially resolve the location of the target spins in double resonance experiments with nanometer precision in three dimensions.

4.5 Heating Effects

An important question in a low temperature setup is the local temperature of the probed sample region. Heat introduced by the laser and high frequency fields might not only affect the standing time of the cryostat, but also lead to local heating. We quantified these effects by measuring the power dissipation of various sources in the cryostat and by an optical temperature measurement of the sample temperature. This novel approach based on color centers in sapphire enables to address local heating effects in the probed sample region which cannot be detected by conventional sensors.

Power dissipation

As already discussed in section 3.3.1, the standing time of the cryostat of six days at 4.7 K correspond to a heating power of about 42 mW introduced by thermal radiation and conduction of the wires. If the AFM is operated, the heater of the pre-amplifier introduces an additional $\sim$ 25 mW (see section 4.3). Since the amplifier is situated in the upper part of the microscope head close to the cryostat cold-plate, this heating reduces the standing time but is not expected to raise the temperature of sample and tip.

The laser power for optical excitation is typically around 4 mW which is sufficient to almost saturate the NV centers when using the Partec objective lens (see figure 4.3). Due to the low absorption of the transparent samples and the high thermal conductivity of the supporting sapphire plate, the sample heating should be negligible. As already discussed in section 4.4, the (material dependent) absorption of the AFM tip causes a considerable thermal expansion of the tip material and thus a crosstalk of focus position (or the time-averaged laser intensity in pulsed experiments) and the AFM z-channel. The local temperature of the tip apex is difficult to estimate, but the heating can be reduced by employing transparent tips, e.g. pulled glass fibers. Due to the high NA and the resulting strong divergence of the laser beam the heating is negligible for parts that are not in the laser focus.

The third and potentially strongest source of dissipative heating are the applied microwave and RF-fields. A transmitted power on the order of 10 dBm (10 mW) through the sample stripline is required to generate a sufficiently strong driving field for nearby spins. Due to the strong damping at high frequencies a much larger power has to be fed into the cryostat transmission line to achieve this field strength. Figure 4.12 (a) depicts a typical transmission curve of the cryostat transmission line and sample waveguides. The transmission is considerably decreasing with higher frequencies. Since the reflexions

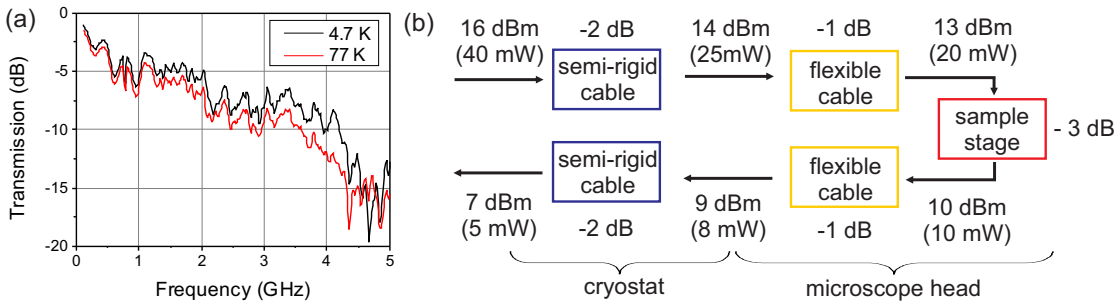

Figure 4.12: (a) Typical high frequency transmission curve of the setup at 77 K and 4.7 K. (b) Block diagram of the transmission losses inside the cryostat at 3 GHz.

are below -20 dB over the full frequency range, the main part of the transmission losses are due to dissipation. In the range of 2.5 - 3 GHz, where the NV center resonance is usually located, the transmission is only around -9 dB or $\sim$ 13 %. The transmission increases slightly at lower temperatures due to the higher electrical conductivity of the materials.

Figure 4.12 (b) shows in detail where in the cryostat the power is dissipated. As an example, numbers for a typical cw-signal of 16 dBm and 3 GHz are stated. The semi-rigid cables leading through the cryostat have a damping of -2 dB, the thin flexible connections between cryostat cold-plate and sample stage -1 dB. The spring contacts in the stage and the different waveguides on the sample holder have a transmission around -3 dBm. Thus, from 40 mW inserted in the setup, 18 mW are dissipated in the transmission line through the cryostat, 12 mW in the connections to the sample stage, 10 mW in the sample stage itself, and only 5 mW are transmitted. Due to the strong thermal coupling between cables and cryostat (see section 3.3.1) the transmission losses here will not affect the sample temperature but only shorten the cryostat standing time. The dissipation in the sample stage on the other hand is expected to cause sample heating. This effect is quantified by the optical temperature measurements described in the next section.

Optical Temperature Measurements

The conventional temperature sensors integrated in the microscope head are too far away from the probed sample region to account for local heating effects of the microwave and the laser. Capitalizing on the optical access to the sample, we employed a spectroscopic method based on the fluorescence of Cr^{3+} color centers in sapphire [170, 171] to access the local temperature. The Cr^{3+} center features a strong fluorescence emission around

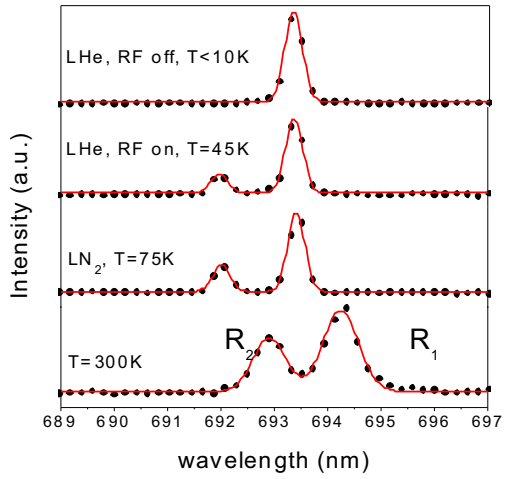

Figure 4.13: Representative fluorescence spectra of Cr3+ in sapphire at different temperatures.

693 nm due to radiative transitions from the ^2E to the $^4A_2$ manifold. Since the ^2E degeneracy is partially lifted by the crystal field, the zero-phonon line is split into two emission lines (referred to as R_1 and R_2) separated by approximately 2 nm. The occupation of the ^2E-levels is governed by the Boltzmann distribution, and therefore the intensity ratio between both lines is strongly temperature dependent. To evaluate the temperature from an intensity analysis the strong polarization of the light emission has to be taken into account; the intensity ratio depends on the angle of the sapphire c-axis relative to the polarization direction of the detector [172].

Since Cr^{3+} is an abundant impurity in the sapphire plates used as support in our sample holders, we estimated the local temperature by analyzing their fluorescence with a grating spectrometer. The analysis of the spectra is complicated by the *a priori* unknown angle between the sapphire c-axis and the spectrometer and the fact that the objective lens does not maintain the polarization direction of the transmitted light at low temperature. To account for these effects, we measured spectra at different base temperatures (T_B = 4.7 K, 77 K, 300 K) and with different polarization directions of the excitation laser. The angle between the sapphire c-axis and the spectrometer axis was inferred from the reference spectra at T_B = 300 K and the polarization dependence published in reference [172]. For the low temperature measurements we estimated the rotation of polarization caused by the objective lens relative to the room temperature measurement by the dependence on the laser polarization. Under the assumption that the fluorescence light undergoes the same rotation we corrected the measured intensity ratios for the polarization effect and were therewith able to compare the results for differ-

ent temperatures. By assuming a simple Boltzmann law we calculated the approximate temperature.

Figure 4.13 shows the acquired fluorescence spectra with the estimated temperature. At liquid helium temperature we measured the spectra with and without strong microwave irradiation to account for RF heating. The laser power was in all measurements set to 2.5 mW, the RF transmitted through the sample waveguide had an approximate power of 10 mW. At liquid nitrogen cooling ($T_B = 77$ K) without applied RF our analysis yielded T = (75 ± 5) K, verifying the applicability of our approach. The results at liquid helium cooling ($T_B = 4.7$ K) with and without RF transmission differ significantly. The spectrum without applied RF shows only a single R1 line, the R2 is frozen out implying negligible heating effects due to laser heating [170]. With applied RF field R_2 is clearly expressed, the local sample temperature is increased to about T = 45 K.

Conclusion

The main heat sources during measurements are the laser irradiation, the heater of the AFM pre-amplifier and the high-frequency driving fields for spin manipulation. The latter provides the dominant contribution to local sample heating, which was estimated to result in a temperature of up to 45 K for cw-irradiation. Typical ODMR-experiments are performed with pulsed RF excitation with lower time-averaged power; for realistic pulse sequences we therefore expect $T \leq 30$ K (depending on the RF duty cycle) to be more realistic. In future experiments the effective temperature could be reduced by improving the thermal anchoring of the sample or by using RF transmission lines thermally decoupled from the sample.

4.6 Conclusion

The presented measurements verify the functional capability as well as the efficient interplay of the different sub-systems. While the AFM performance is enhanced at low temperature due to an improved stability and force sensitivity, the performance of the optical imaging system is clearly degraded under cryogenic conditions. As a figure of merit for NV-magnetometry the optical efficiency parameter C defined in section 2.3.2 can be employed: with an optical count rate of 30 kcts/s per single NV center and an ODMR contrast of 20% this yields $C \approx 0.013$. Even with the relatively short T_2 of approximately 10 μs for the shallow NV centers in the diamond samples studied so far, this should enable sensing and imaging of individual electron spins (compare figure 2.11).

Prospects for improving the optical count rate and the ODMR contrast will be discussed in section 6.1.1.

Chapter 5

Probing the Spin Dynamics of Ferritin

To demonstrate NV magnetic sensing of molecular spin dynamics at low temperatures we studied horse-spleen ferritin proteins. The individual molecules possess a mineral core with a relatively large magnetic moment of roughly 300 μ_B and therefore generate a strong spin signal. Recently, the T_1-relaxometric detection of ferritin molecules under ambient conditions has been demonstrated using NV centers in nanodiamonds [115] and bulk diamond [11]. Here we carry out NV magnetometry utilizing different sensing protocols to study the magnetic properties in a wide temperature range from room temperature down to 5K, enabling tracking of the temperature dependent spin relaxation time over many orders of magnitude. To address these different timescales of the spin dynamics, a combination of different experimental techniques is commonly used, including Mößbauer spectroscopy [19,20,173], susceptibility measurements [174–176] and ESR spectroscopy [22]. We demonstrate that by tuning the detection bandwidth by appropriate ODMR protocols this wide frequency range can be covered by NV magnetometry. In contrast to the above mentioned techniques, the high sensitivity of the NV sensor enables additionally the investigation of single molecules.

5.1 Structure and Magnetic Properties of Ferritin

Ferritins are a family of proteins occurring in mammals, bacteria and plants with the primary function being iron storage [177]. The form predominant in mammals, which is considered in the following, consists of 24 subunits forming a hollow protein shell, which surrounds a cavity with approximately 8 nm diameter [178]. This cage-like nanostructure encloses an inorganic core containing a maximum of 4500 iron atoms, which are stored

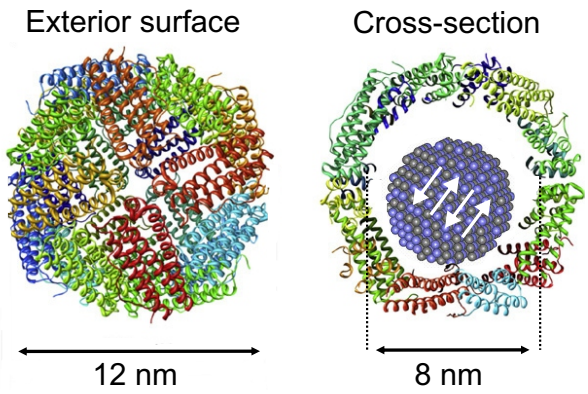

Figure 5.1: Ribbon diagram of the ferritin exterior surface and a cross-section revealing the cavity with the antiferromagnetic core. Modified from [178].

in form of a hydrous ferric oxide-phosphate mineral similar in structure to ferrihydrate [19]. Besides its physiological importance, ferritin attracted much attention for the magnetic properties of this biomineral core. Since the organic shell prevents aggregation, ferritin molecules are a unique model system for the investigation of spin-structure and dynamics of isolated nanoparticles, revealing effects like superparamagnetism [173], superantiferromagnetism [176, 179], and macroscopic quantum tunneling [175].

These effects arise from Fe^{3+} spins ($S = 5/2$) in the ferritin core, which are antiferromagnetically coupled at lower temperatures. The Neél temperature is still under debate with estimates ranging from 240 K [19] to 500 K [179]. This large spread is due to the fact that superparamagnetism sets in at a temperature far below the Neél temperature [20]: due to the small particle size and the corresponding low anisotropy energy barrier, the Neél-vector fluctuates between easy directions with a relatively fast (temperature dependent) rate, prohibiting the observation of the phase transition and thus the determination of the Neél-temperature by conventional methods.

Even in the antiferromagnetically ordered phase the ferritin core possesses a net magnetic moment due to an imperfect compensation of the Fe^{3+} spins on the two sublattices. The magnetic moment scales with the iron loading factor of the core approximately as $\mu = \sqrt{n}\,\mu_{Fe^{3+}}$, where n is the number of iron atoms and $\mu_{Fe^{3+}} = 5.92\ \mu_B$ the ionic moment [174]. This indicates a random population of the sublattices throughout the volume of the nanoparticle as origin of the excess moment, rather than surface effects or a canting of the sublattices [174]. The ferritin core forms a single domain with uniaxial anisotropy, thus the spin relaxation time τ can be described by the Neél-Arrhenius equation [180, 181]

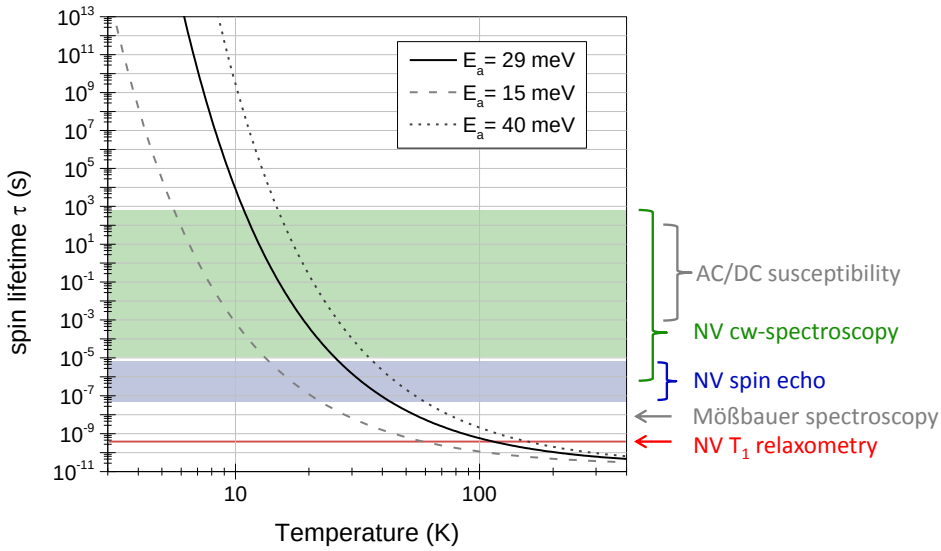

Figure 5.2: Spin lifetime τ of the antiferromagnetic ferritin core for three different anisotropy barriers. The curves represent equation 5.1 with $\tau_0 = 2 \cdot 10^{-11} s$ [182]. The characteristic timescales of Mößbauer spectroscopy and AC/DC susceptibility measurements are indicated in gray, the sensitivity windows for NV-based T_1-relaxometry, spin echo, and cw-spectroscopy are sketched in red, blue, and green, respectively.

$$\tau = \tau_0 \cdot \exp\left(\frac{E_a}{k_B T}\right) \tag{5.1}$$

The prefactor τ_0 can be interpreted as inverse attempt frequency, E_a denotes the anisotropy energy of the core particle. The experimentally derived values for τ_0 have a large spread and are typically in the range $10^{-13} - 10^{-9}$s [20, 182, 183]; in the following, a value of $\tau_0 = 2 \cdot 10^{-11} s$ is used for calculations. For a particle with volume V the anisotropy energy barrier can be expressed as $E_a = KV + E_{sh} + E_s + E_\sigma$, where K is the magnetocrystalline energy density and E_{sh}, E_s, E_σ account for additional contributions due to the particle shape, surface effects and strain [20], respectively.

The temperature dependence of the spin relaxation time is shown in figure 5.2 for three different values of the anisotropy barrier E_a. The spin relaxation corresponds to thermally induced reversals of the magnetization with an average rate $1/\tau$. If this strongly temperature dependent frequency is much faster then the characteristic measurement time of the applied sensing technique, the measurement yields an average value over the rapidly fluctuating magnetic field, resembling a paramagnetic behavior. If the switching frequency is much lower then the timescale of the measurement, the spin

dynamics is effectively blocked and a net magnetization can be detected. The former is called superparamagnetism, while the (technique dependent) transition temperature between both regimes is referred to as blocking temperature T_B. The spin dynamics of Ferritin has been previously studied by various techniques; Mößbauer spectroscopy (characteristic measurement time $\tau_m \sim 10^{-8}$ s) yields typical blocking temperatures on the order of $T_B \sim 30\text{-}50$ K [19, 20, 173], susceptibility measurements $T_B \sim 5\text{-}20$ K ($\tau_m \sim 10^{-4} - 100$ s) [20, 174–176], and electron spin resonance $T_B \sim 100$ K ($\tau_m \sim 10^{-9}$ s) [22]. These findings follow approximately the $T_B \propto \log(\tau_m)^{-1}$ dependence expected from equation 5.1. Also the scaling of T_B with the iron content and thus the core size V has been observed [173, 174].

In the following we use NV magnetometry with different AC sensing schemes to probe the ferritin spin dynamics at varying temperatures. The key advantage of this technique is the capability for tracking the spin dynamics over a wide frequency range even on the single molecule level by capitalizing on the tunable detection bandwidth and extraordinary sensitivity of the NV sensor.

5.2 Experimental approach

To investigate the ferritin spin dynamics we measured the longitudinal relaxation time T_1, the coherence time T_2, and the decoherence time T_2^* of shallow NV centers coupling to adsorbed ferritin molecules on the diamond surface at different temperatures. The horse-spleen ferritin (Sigma-Aldrich) was deposited with different coverages by a drop-casting method. For that the diamond surface was covered with diluted ferritin solution for a few minutes and subsequently rinsed with pure water before drying it in Ar-flow. The NV sensor spins were located in a depth of 5 -10 nm below the surface (2.5 keV and 5 keV implantation energies). Spin ensembles of densely implanted NV centers as well as individual NV spins were utilized in the experiments.

Figure 5.3 (a) shows schematically the sample geometry. Due to the short range of the dipolar interaction, the distance between NV center and ferritin molecule has to be less than ~ 15 nm to affect the NV spin. Thus, even for multi-layers of adsorbed ferritin each NV center couples only to a limited number (≤ 10) of molecules. For sufficiently reduced molecular coverages also the coupling to single ferritin molecules can be realized. The approximate number of adsorbed ferritin molecules on the diamond surface was analyzed by AFM; a typical topography image for the case of sub-monolayer coverage can be seen in figure 5.3 (c).

As discussed in section 2.2, the different relaxation times T_1, T_2, and T_2^* of the

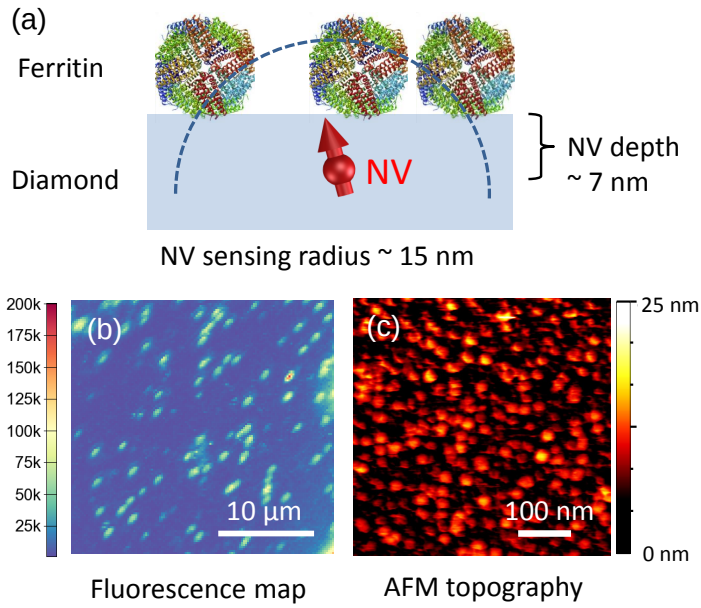

Figure 5.3: (a) Sample schematic; ferritin molecules are adsorbed on the diamond surface and couple to shallow implanted NV centers. Due to the short range interaction, a single NV center interacts only with a small number of molecules. Different Ferritin coverages and NV center densities are employed for the measurements. (b) Fluorescence map of isolated NV centers. (c) AFM topography image of adsorbed ferritin molecules with sub-monolayer coverage.

NV sensor are accessed by the inversion recovery protocol, spin echo spectroscopy and one-pulse ODMR spectroscopy, respectively. These protocols are linked with distinct spectral sensitivities, such that they are expected to be susceptible to the ferritin spin dynamics in different temperature ranges. The temperature dependence of the NV center relaxation times in response to the ferritin can be described by the simple model presented in the next section.

5.3 Model of the Ferritin - NV Center Interaction

The NV center couples to the magnetic core of nearby ferritin molecules via dipolar interaction. To describe the interaction, the spectrum of the magnetic field generated by the ferritin core and the spectral sensitivity of the driven NV spin have to be considered. Depending on the frequency of the ferritin spin noise, the longitudinal relaxation and / or the transverse relaxation of the NV spin will change; the reverse effect of the NV spin on the ferritin core can be disregarded since the magnetic moment of the ferritin core is orders of magnitude larger the moment of the NV center.

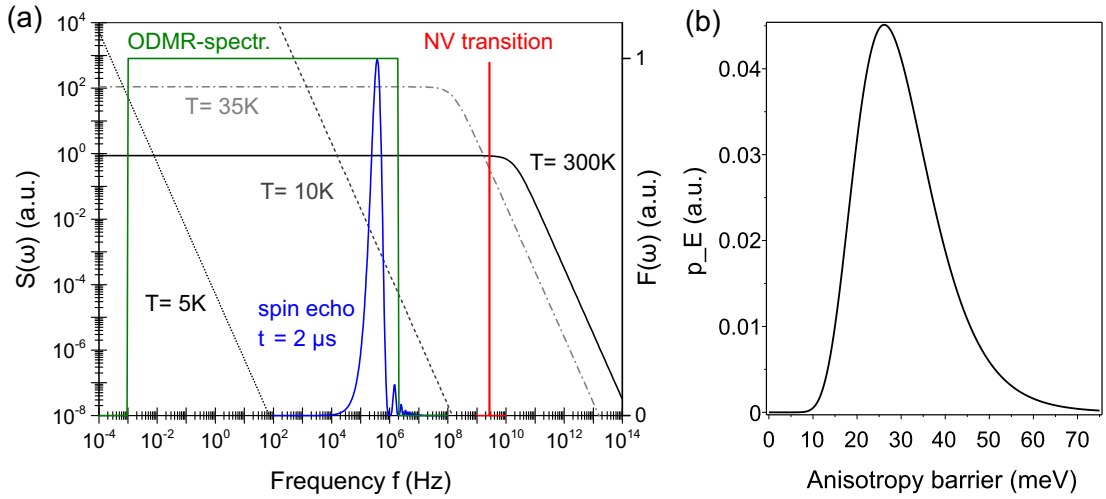

Figure 5.4: (a) Spectral density $S(\omega)$ of the ferritin spin noise for different temperatures. The curves represent equation 5.2 for an anisotropy barrier of $E_a = 25$ meV and $\tau_0 = 2 \cdot 10^{-11}$s. The spectral sensitivities $F(\omega)$ of T_1 relaxometry, spin echo spectroscopy and ODMR-spectroscopy are additionally depicted in red, blue, and green, respectively. (b) Log-normal distribution of Anisotropy barriers in an ensemble of ferritin molecules, corresponding to equation 5.4 with $\overline{E_a}$= 29 meV and σ_E=0.321 [21].

The flipping of the magnetization of a single molecule generates magnetic field fluctuations resembling random telegraph noise with a temperature dependent frequency distribution. The spectrum of this spin noise can be modeled employing the autocorrelation function, which was already used in section 2.3.1. If the autocorrelation function is assumed to decay exponentially with the ferritin spin lifetime as decay time constant, one obtains a lorentzian noise spectrum:

$$S(\omega, T, E_a) = \frac{\langle B^2 \rangle}{\pi} \frac{\tau(T, E_a)}{1 + \tau(T, E_a)^2 \omega^2} \tag{5.2}$$

Here, $\langle B^2 \rangle$ describe the distant dependent coupling strength between the NV center and the ferritin molecule. The spectrum is shown in figure 5.4 for different temperatures. For lower temperatures the high-frequency components are suppressed, while the amplitude at low frequencies increase. This reflects the fact that the integral of the noise spectrum over the full frequency range is proportional to the magnetic moment of the ferritin core, which can be assumed to be temperature independent. As discussed in section 2.3, the relaxation rate Γ of the NV center can be derived from the environmental noise spectrum by the expression

$$\Gamma = \Gamma_{int} + \Gamma_{env} = \Gamma_{int} + \int S(\omega, T, E_a)\, F(\omega)\, d\omega \tag{5.3}$$

where Γ_{int} accounts for intrinsic relaxation processes and $F(\omega)$ denotes the spectral response function of the applied ODMR protocol.

To track the ferritin relaxation dynamics over a large temperature range, we employed T_1-relaxometry, spin echo spectroscopy, and one-pulse ODMR-spectroscopy. The spectral response of the former two techniques has been discussed in chapter 2 and is shown in figure 5.4 in red for T_1-relaxometry and in blue for spin echo spectroscopy, respectively. ODMR-spectroscopy is susceptible to magnetic fields over a wide frequency range; For our analysis we assumed the averaging time per spectrum ($\sim 10^3$ s) and the length of the microwave pulse ($\sim$ 500 ns) as limits for the spectral sensitivity, which result in an estimated sensitivity window depicted in green in figure 5.4.

When molecular ensembles are investigated, the distribution of anisotropy barriers in the sample has to be taken into account. It results from the different iron content per molecule and correspondingly a spread of core volumes, but also from varying contributions due to shape, surface effects and strain for the individual molecules [20, 182]. The distribution of core volumes and the resulting spread of anisotropy energies in a ferritin ensemble was investigated in detail in reference [21], indicating a log-normal distribution of energy barriers

$$p_E(E, \overline{E_a}, \sigma_E) = \frac{1}{\sqrt{2\pi}\sigma_E E} \exp\left(-\frac{\ln(E) - \ln(\overline{E_a})}{2{\sigma_E}^2}\right) \tag{5.4}$$

with mean value $\overline{E_a}$ = 29 meV and width parameter σ_E =0.321. This function is plotted in figure 5.4 (b). Using this result, the spectral density of the molecular ensemble can be written as

$$S_e(\omega, \overline{E_a}, \sigma_E, T) = \int_0^\infty S(\omega, T, E) \cdot p_E(E, \overline{E_a}, \sigma_E)\, dE \tag{5.5}$$

This simplified model enables the calculation of the temperature dependent NV relaxation times T_1, T_2, and T_2^* in response to the ferritin spin dynamics and thus a direct comparison to the experimental results presented in the next sections.

5.4 Investigation of Ferritin Ensembles

Ferritin ensembles were studied by preparing samples with multi-layers of molecules adsorbed on diamonds containing densely implanted NV centers. The different ODMR

sensing protocols were applied at varying temperatures. For reference, the same measurements were repeated on clean diamond samples without adsorbed ferritin.

T_1 relaxometry

As T_1 relaxometry is susceptible to magnetic noise at the NV transition frequency (see section 2.3.1), which was $f_{NV} = 2.7$ GHz for the applied external field of 5 mT, these measurements effectively probe high frequency magnetization reversals of ferritin. The temperature dependent longitudinal relaxation time T_1 of the NV center ensemble is shown with and without adsorbed ferritin in 5.5 (a).

The reference measurement without ferritin reveals a strong increase of T_1 between room temperature and 77 K. In the range 77 K to 4.7 K it is above 2.5 ms, which was the longest decay time detectable in our measurement protocol. This temperature dependence agrees with published results [83]. Upon the adsorption of ferritin molecules, the T_1 time at room temperature is reduced roughly by a factor of 5, similar to previous observations for bulk diamonds [11] and diamond nanocrystalls [115]. The ferritin-induced reduction in T_1 vanishes at low temperatures, since the cut-off frequency of the ferritin noise spectrum shifts below the NV transition frequency. The experimental data shows approximately an exponential increase of T_1 with lower temperatures. The characteristic temperature of this exponential dependence, which can be interpreted as blocking temperature for T_1-relaxometry, is T_B= 50 K.

The red curve in figure 5.5 depicts the simulated longitudinal relaxation time using the above described model with the filter function $F_{T_1}(\omega) \approx \delta(\omega - \omega_{NV})$ for T_1 relaxometry. For the intrinsic relaxation processes a temperature dependence as found in reference [83] was assumed. We adjusted the value for the mean anisotropy barrier of the molecular ensemble and the interaction strength until a reasonable agreement with the experimental data was obtained, yielding $\overline{E_a} \approx 15$ meV and $\sqrt{\langle B^2 \rangle} = 22$ MHz. We note that varying the width parameter σ_E of the energy distribution function or the exact form of the temperature dependence of $\Gamma_{1,int}$ has only an negligible effect on the simulated curve, such that these parameters were not systematically optimized to reproduce the measurement outcome.

The simulated curve describes the experimental data reasonably well at higher temperatures and also reproduces the strong increase in T_1 below 50 K. For lower temperatures the measured relaxation times scatter strongly and are significantly shorter than the calculated values. This might be a measurement artifact related to the optical leakage of the acousto-optical modulator used to create the laser pulses; since the measurement of long T_1 requires pulse sequences with prolonged "dark" intervals, the

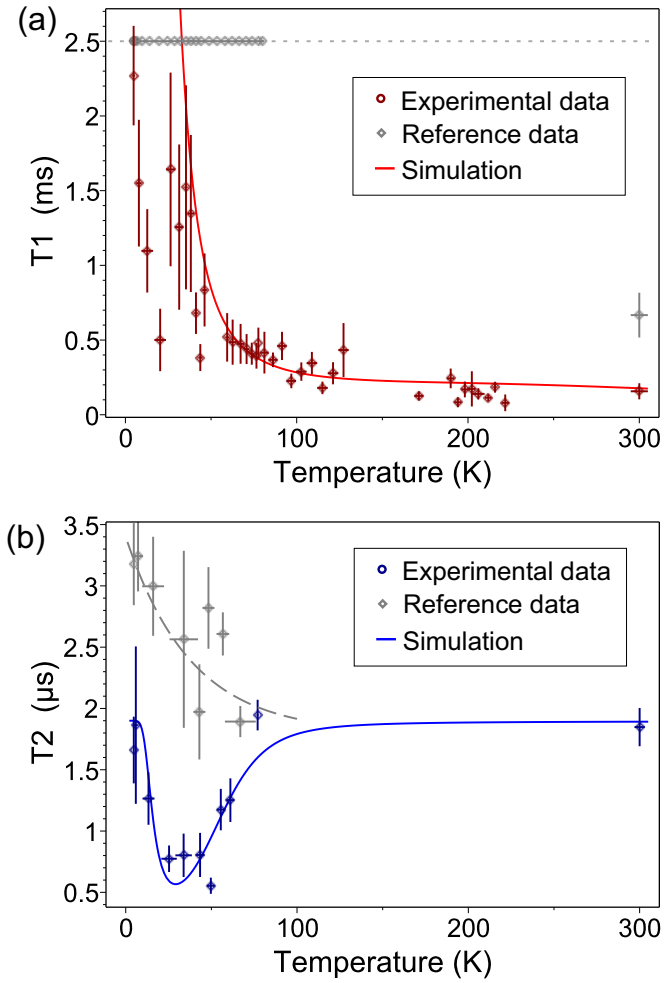

Figure 5.5: (a) Experimental and simulated longitudinal relaxation time T_1 of an ensemble of NV centers interacting with adsorbed ferritin molecules. The parameters used for calculating the red curve were $\overline{E_a} = 15$ meV and $\sqrt{\langle B^2 \rangle} = 22$ MHz. Reference data measured without adsorbed ferritin is depicted in gray. The longest decay time detectable in the experiment was 2.5 ms, indicated as upper sensitivity limit by the dashed line. (b) Experimental and simulated spin coherence time T_2 of an NV ensemble with adsorbed ferritin molecules. The simulated curve is calculated using $\overline{E_a} = 25$ meV and $\sqrt{\langle B^2 \rangle} = 10$ MHz. Reference data measured without adsorbed ferritin is depicted in gray.

parasitic photon transmission in the off-state of the AOM can significantly affect the measurement result by reducing the observed spin lifetime.

Spin echo spectroscopy

Spin echo spectroscopy of the NV sensor spins is used to access the ferritin magnetization dynamics at lower frequencies around 0.5 - 1 MHz. The temperature dependence of the obtained coherence time T_2 of the NV ensemble is depicted in figure 5.5 (b). At room temperature it is rather unaffected by the ferritin molecules, since the intrinsic transverse relaxation rate $\Gamma_{2,int}$ is relatively high due to the surface proximity of the NV centers. The additional contribution induced by the ferritin is comparably low, since the ferritin spin noise is stretched over a wide frequency range (see figure 5.4 (a)). This changes at low temperatures; as the cut-off frequency of the ferritin noise spectrum decreases, the spectral density in the probed frequency range initially increases with lower temperatures. The ferritin contribution to the relaxation rate becomes dominant for temperatures below $\sim$ 80 K, leading to a reduction of T_2. When the temperature falls below $\sim$ 35 K, the cut-off frequency of the ferritin noise spectrum shifts below the detection window of the spin echo sequence, resulting in a recovery of the T_2 time. At 5 K it approaches the room temperature value. The minimum in the coherence time T_2 at roughly 35 K corresponds to the blocking temperature of ferritin for spin echo spectroscopy. The reference measurement acquired without adsorbed ferritin shows only a modest increase of T_2 with lower temperature which might be related to temperature dependent intrinsic relaxation processes.

The blue curve depicts the calculated coherence time using the spin echo filter function given in equation 2.11. A good agreement with the experimental data is achieved with the parameters $\overline{E_a} = 25$ meV and $\sqrt{\langle B^2 \rangle} = 10$ MHz. The experimentally observed broad dip in T_2 is well reproduced by the theoretical curve, indicating that the employed model provides an adequate description of the ferritin-NV interaction.

The discrepancy in the obtained fit-parameters $\overline{E_a}$ and $\sqrt{\langle B^2 \rangle}$ for the T_1 and T_2 data is probably explained by to the fact that different samples were used for the measurements, and correspondingly the distribution of anisotropy barriers and the number of detected molecules were different in both experiments. In general the obtained values correspond well to reported average anisotropy barriers in ferritin around 28 meV determined by Mößbauer spectroscopy and magnetization measurements [21, 176].

ODMR spectroscopy

Further insight into the ferritin spin dynamics especially at low frequencies is provided by ODMR-spectroscopy. Two spectra of the NV center ensemble acquired at 77 K and 4.7 K are shown in figure 5.6. A broadening of the resonance lines at 4.7 K by

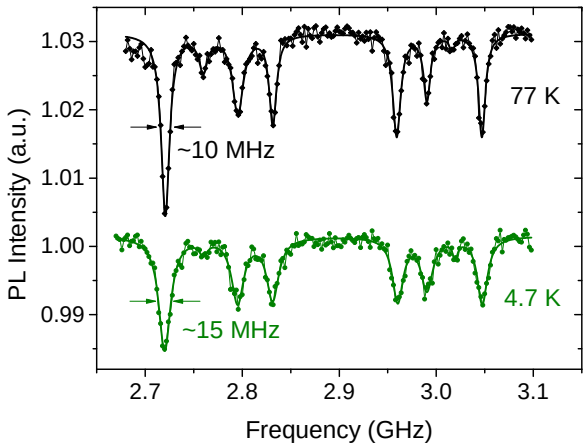

Figure 5.6: Comparison of the ODMR spectra of an NV center ensemble acquired at 77 K and 4.7 K, revealing a broadening of the resonance lines at lower temperature.

roughly 5 MHz is obvious. In both spectra the line width is probably affected by power broadening arising from the microwave pulse; however, since the experimental parameters were very similar in both measurements, the pronounced difference in both spectra can be attributed to the ferritin spin noise. This effect can be interpreted using the spectral sensitivity window for ODMR-spectroscopy as discussed in section 5.3; at 77 K, the majority of the ferritin molecules fluctuate with a rate faster than the inverse microwave pulse length (500 ns), such that only the average magnetization of the molecular ensemble is affecting the line shape. This effect is similar to the so-called motional narrowing commonly observed in NMR- and ESR spectroscopy in liquids [6,7]. At 4.7 K the spin dynamics of most molecules is blocked, therefore the magnetization is static over the measurement time ($\sim 10^3$ s). Since the local magnetic field differs for the NV centers in the ensemble depending on the size and the orientation of the nearby molecules, their resonance frequencies vary and correspondingly a broad transition line width is observed. Such anisotropic broadening has also been observed in ESR studies of ferritin ensembles [22]. The line width of ∼15 MHz at 4.7 K is comparable to the coupling strength $\sqrt{\langle B^2 \rangle}$ estimated from the T_1 and T_2 measurements. It correspond to an internal field variation in the NV center ensemble on the order of 500 μT, which is consistent with the estimated dipolar field of ferritin molecules with a magnetic moment of 300 μ_B on the diamond surface in $\sim$ 7 nm distance.

5.5 Study of Isolated Ferritin Molecules

To make use of the extremely high sensitivity of NV magnetic sensing and its capability for investigating single molecules, we reduced the coverage of the adsorbed ferritin such that isolated molecules are obtained (figure 5.3 (c)). By employing individual NV centers as sensors, the number of detected molecules can be expected to be very low due to the short range interaction. We studied the same NV centers (∼35 in total) before and after ferritin deposition and found for roughly 50% a pronounced reduction of T_1 at room temperature. These centers interacting with one or more molecules where investigated at low temperature.

Spin echo spectroscopy

Figure 5.7 (a) shows the temperature dependent coherence time T_2 for a representative single NV center. In contrast to the ensemble measurements, the curve exhibits several minima with varying width. Other NV centers investigated revealed only a single feature in the same temperature range. In general, all observed coherence dips fall in the range of the broad feature observed in the ensemble measurements. In a reference measurement on one NV center showing no ferritin-induced T_1 effect at room temperature, no minima in the coherence time are observed. These findings verify the assumption that only a small number of molecules in the direct vicinity of each NV center contribute to the measured signal. We modeled the response of a NV center to a single molecule by considering $S(\omega)$ without ensemble broadening. The resulting temperature dependence of the coherence time is shown in figure 5.7 (b). The observed T_2 dip at T = 47 K in (a) can be reproduced by assuming an anisotropy energy of E_a= 43 meV and a coupling strength $\sqrt{\langle B^2 \rangle} = 1.5$ MHz. The width of the simulated dip is on the order of 10 K, which corresponds well to the sharp features observed in the experiment. This suggests that such signals can be attributed to single molecules, and that the different minima in figure 5.7 (a) correspond to molecules with different anisotropy barriers in the vicinity of the NV center. This interpretation is consistent with the rather low coverage in the experiment and the limited sensing range of each NV center.

ODMR spectroscopy

To address the spin dynamics at lower frequencies, ODMR-spectroscopy at 4.7 K and 77 K was performed. The anisotropic broadening effect observed in the ensemble measurements in 5.4 should not be present in single NV center spectra, instead a random shift

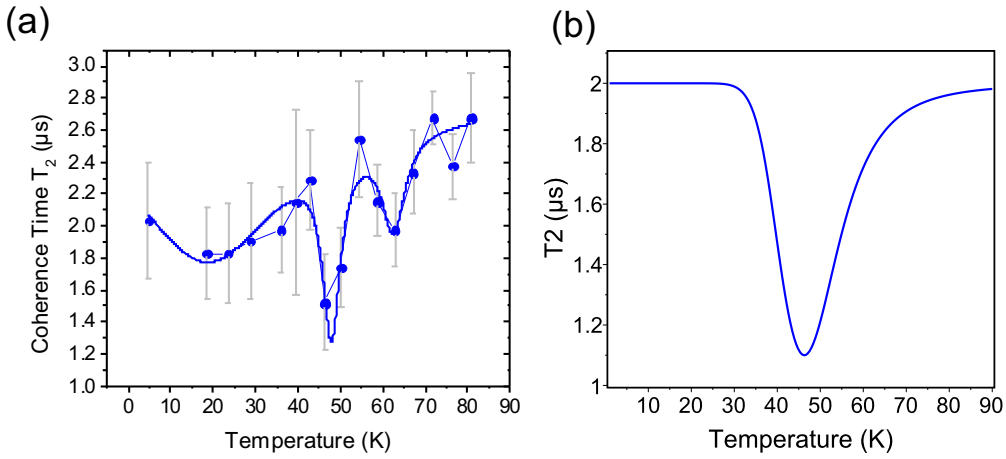

Figure 5.7: (a) Representative T_2 temperature dependence of a single NV center interacting with isolated molecules. (b) Simulated coherence time for an NV center coupling to a single molecule with $E_a = 43$ meV and $\sqrt{\langle B^2 \rangle} = 1.5$ MHz.

of the transition frequency can be expected between 4.7 K and 77 K. Experimentally we find this shift to be ~ 1 MHz for all NV centers studied, which is significantly smaller then the line broadening in the ensemble. This is explained by the larger implantation depth of the single NV centers with respect to the NV ensembles (5 keV compared 2.5 keV implantation energy) and the reduced ferritin coverage, such that the coupling strength between NV center and ferritin is reduced and consequently the line shift is smaller. This is consistent with the rather low coupling strength estimated from the T_2 measurements discussed above. The observed shift in the ODMR-spectra is furthermore influenced by intrinsic effects like the temperature dependent zero-field splitting or strain [184], which might cover the effect of the static ferritin magnetization.

A part of the studied NV centers, roughly 20%, show a pronounced broadening of the line shape, which is depicted in figure 5.8 (a). The majority of the investigated NV centers exhibited similar line shapes at 4.7 K and 77 K, as shown in figure 5.8 (b). The line broadening is probably related to one or a few nearby ferritin molecules with rather low anisotropy energies, such that the spin dynamics is not blocked at 4.7 K. Figure 5.7 (c) shows the simulated NV decoherence time T_2^* (corresponding to the inverse line width) for the interaction with molecules with distinct anisotropy barriers. For particles with larger energy barriers the spin noise in the detection bandwidth is comparable at 4.7 K and 77 K, such that a similar line shape in the ODMR-spectrum can be expected. For particles with lower anisotropy barrier the field fluctuations in the respective frequency range are strongly enhanced at 4.7 K. This fits our experimental observation that spectral broadening occurs only for a fraction of investigated NV centers. The

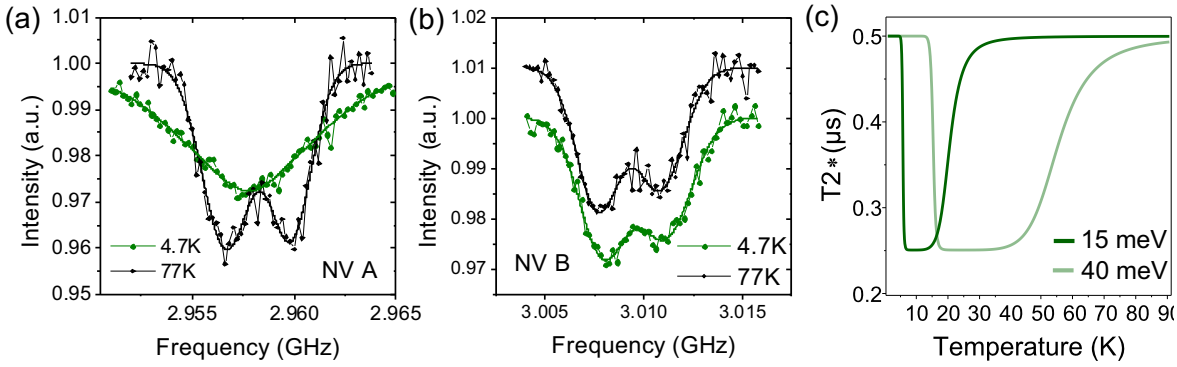

Figure 5.8: (a) and (b): Representative ODMR spectra of single NV centers at 77 K and 4.7 K. Roughly 20 % of the investigated NV centers exhibited low temperature line broadening as shown in (a), while the majority showed no pronounced change in line shape as seen in (b). (c) Calculated temperature dependence of T_2^* for an NV center coupling to ferritin molecules with large (E_a= 40 meV, light green) and small (E_a = 15 meV, dark green) anisotropy barrier.

corresponding upper limit for the anisotropy barrier of the detected ferritin core can be estimated to 15 meV, which is consistent with the expected spread of anisotropy energies in the sample.

Although the observed spectral broadening in the NV ensemble and for single NV centers appear very similar, it is noteworthy that the underlying mechanisms discussed above are rather different: while for single NV centers it is an effect exclusively arising from time averaging over the measurement period, the anisotropic broadening in the ensemble was assumed to be predominantly due to spatial averaging.

5.6 Conclusion

We studied the temperature dependent spin dynamics of ferritin proteins by using different ODMR-protocols with sensitivities in distinct frequency ranges. By investigating molecular ensembles, the (technique dependent) average blocking temperatures and consequently the mean anisotropy barrier could be obtained. The results are in satisfactory agreement with previously reported findings using Mößbauer spectroscopy and susceptibility measurements. In contrast to these widely used characterization techniques, the NV center sensing method features a much wider detection band width ranging from the GHz range down to (practically) DC. Furthermore, the extremely high sensitivity enables the investigation of single molecules, which has been realized so far only by SQUID magnetometry [185]. Our results on isolated ferritin molecules detected by

single NV centers revealed features which can most likely be attributed to individual molecules. To confirm these findings and carry out single molecule investigations in a more controlled and precise way, the scanning probe capability of our experimental setup has to be utilized. A systematic study of individual molecules or nanoparticles might elucidate further details of the spin structure of nanoscale magnetic systems, for example in the case of ferritin the presence of a proposed two-phase spin order in a core-shell geometry [22, 186].

Chapter 6

Outlook

The previous chapters 2 to 4 presented the operation principle, the design and the current performance of the scanning probe NV magnetometer. As demonstrated in chapter 5, the sensitivity and variety of sensing protocols of NV magnetometry in combination with the accessible low temperature already facilitates quantitative studies of molecular properties which cannot be readily obtained by other techniques. However, further development of the experimental setup and measurement protocols, capitalizing also on the precise scanning probe capabilities and the UHV conditions provided by the setup, will enable truly unprecedented experiments on the single spin level. This last chapter outlines in the first part possible improvements of the experimental apparatus that might help to overcome current technical limitations to the measurement performance. The second part briefly describes potential future experiments in the field of molecular spin imaging and spectroscopy.

6.1 Prospects for an Improved System Performance

The instrument performance can be significantly enhanced by further development and optimization of the different components. Especially the optical readout of the NV center, which is up to now suffering from the poor performance and throughput of the objective lens at low temperature, offers plenty of room for improvements. Another field for further development is the sample preparation, which can be optimized to make full use of the UHV conditions and its potential for atomically clean surfaces and well controlled measurement environments.

6.1.1 Enhancement of the Optical Spin Readout

As discussed in section 2.3.2, the sensitivity in spin sensing experiments depends on the total photon count rate per NV center and the ODMR contrast. Both parameters provide room for optimization: The photon count rate can be improved by increasing the collection efficiency by means of photonic structures, while the ODMR contrast can be significantly enhanced by performing resonant laser excitation of the NV center.

Increasing the optical collection efficiency by photonic structures

The typical photon count rate per NV center in a bulk diamond at 4.7 K is 20 - 30 kcts/s (see section 4.1). Higher quality air objective lenses at room temperature achieve approximately 100 kcts due to a more efficient aberration correction. However, the maximum photon emission rate of the NV center is by more than one order of magnitude higher. Many of the emitted photons are effectively trapped inside the diamond due to the high refractive index of diamond (n=2.4) and the resulting total internal reflection at the diamond/air (or diamond/vacuum) interface [187], see figure 6.1 (a). Therefore the typical photon collection efficiency for a NV center in a bulk diamond is only around 3% [188]. This limitation can be circumvented by the use of NV centers located within diamond nanocrystals small enough that the centers effectively emit into free space, leading to an up to 5 times higher photon collection. However, the spin properties of NV centers in nanodiamonds are strongly affected by surface defects resulting in a short coherence time [87], which makes them unsuitable for spin sensing applications.

An more favorable approach to overcome the total internal reflection while maintaining bulk-like spin properties is the use of a solid immersion lens, i.e. a hemispherical lens fabricated out of diamond. As schematically shown in figure 6.1 (b), all light rays emitted from the center of the SIL are normal to the diamond/air interface, such that no refraction occurs. Diamond SILs containing single NV centers in the center have been produced by two distinct approaches; one possibility is to machine a bulk diamond into a half-spherical shape with rather large diameter on the order of 1 mm [190]. Another approach is the fabrication of micrometer-sized SILs into bulk diamonds by means of focused ion beams [191, 192], resulting in structures as shown in figure 6.1 (d). The reported enhancement factors for the single NV count rate are similar in both approaches with typical values of 6 - 10 depending on the quality of the SIL and the numeric aperture of the collection optics.

Another interesting approach is embedding the NV centers in diamond nanopillars produced by top-down nanofabrication techniques [188, 193]. Such columns with ap-

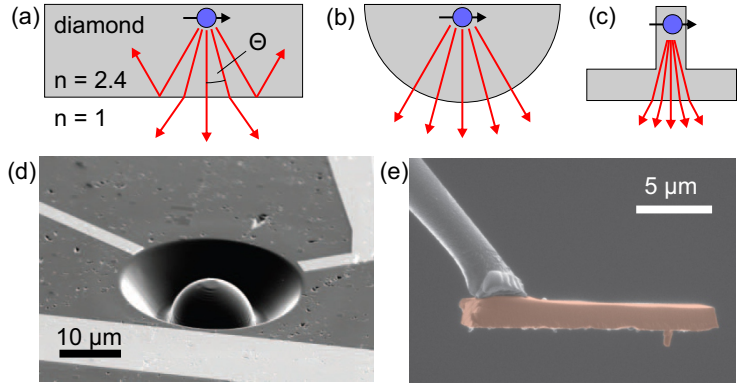

Figure 6.1: (a) Reduction of the effective numeric aperture due to refraction at the diamond surface. The critical angle for total internal reflection is $\Theta_c \approx 24.6°$. (b) Elimination of refraction in a solid immersion lens. (c) Waveguiding in diamond nanopillars. (d) Micro-fabricated diamond SIL from reference [189]. (e) Diamond nanopillar scanning probe from reference [49].

proximately 200 nm diameter and a length of 2 μm effectively act as photon waveguide directing the emitted light to the collection optics above or below the nanopillar (see figure 6.1 (c)). Experimentally, an enhancement factor of 10 for the single NV count rate was demonstrated [193]. Moreover, if the NV center is located sufficiently close to the nanopillar apex, these structures can be directly employed as scanning tips for scanning probe microscopy [49]. An electron micrograph of such an monolithic scanning NV sensor is shown 6.1 (e).

Samples containing diamond SILs or nanopillars as well as nanopillar scanning probes can be mounted in our experimental setup without further modifications to the instrument. Although the fabrication of such structures is still challenging, the enhancement in count rate and thus sensitivity makes it a promising approach for future experiments.

High Fidelity Readout by Resonant Excitation

Apart from the net count rate also the ODMR contrast has a strong impact on the magnetic sensitivity (see section 2.3.2). In our setup we demonstrated a contrast of 20 - 25 %, which is close to values typically achieved in room temperature setups. The difference can be attributed to an increased background count due to the poor performance of the objective lens at low temperature. Under cryogenic conditions however an alternative readout scheme based on resonant laser excitation with a potentially much higher spin contrast can be employed [189].

While at room temperature phonon-induced transitions within the ^3E excited state (consisting of the orbital doublet E_x and E_y, see section 2.1.2) prevent the observation of the fine structure, at low temperature spin-selective optical transitions can be resonantly driven [67]. This enables a high-fidelity read-out of the NV spin state: to probe for example the occupation of the optical ground state with m = ±1, the excitation laser can be tuned to the transition connecting this sub-level to the E_x excited state with primarily m=±1 character; the presence or absence of fluorescence reveals the spin state. Experimentally a fidelity of 93 % has been demonstrated [189]. In a similar manner also the spin state initialization can be considerably improved.

Using resonant laser excitation is experimentally more challenging than the so far employed off-resonant excitation by green light. Apart from the need for a tunable laser source also the spectral diffusion of shallow NV centers has to be considered, since photo-ionization of crystal defects can lead to fluctuating electric fields and therefore spectral jumps of the NV resonance. This issue requires additional experimental effort to ensure that measurements are performed on resonance (see reference [189] and its supplemental information).

Apart from the enhanced ODMR contrast, the reduced wavelength and the corresponding lower photon energy (1.95 eV at 637 nm compared to 2.33 eV at 532 nm) might be advantageous in terms of background fluorescence and photostability. The excitation of photoluminescence from contaminations or crystal defects is probably less effective at a longer wavelength, such that an improved signal-to-noise ratio in the NV read out can be expected. A similar argument holds for potential target molecules; since the absorbance is lower at decreased photon energies for most molecules, the issue of optical excitation and resulting photobleaching should be reduced. As discussed in section 6.2.1, the photostability was found to be a major obstacle in the investigations of organic radicals carried out so far.

6.1.2 UHV Sample Preparation

Although the system is designed for experiments under UHV conditions and measurements are routinely performed at a base pressure on the order of 10^{-10} mbar, the sample surfaces in the experiments so far exhibited still a high level of contamination and were far from being clean on the atomic scale. This is due to the fact that the samples were prepared under ambient conditions and introduced to the vacuum system without further in-situ cleaning procedures. Consequently the sample surfaces exhibit an adsorbate layer of water and other impurities arising from the exposure to air, residues from solvents employed in the wet-chemical cleaning procedure and possibly also contaminations

from the epoxy resin used for mounting the sample.

This contamination layer hinders high resolution experiments on single molecules in various ways: first, it strongly affects the stability and resolution of the AFM, which may preclude the identification of adsorbed target molecules via AFM topography and hampers precise positioning of the tip. Second, a contamination layer on the diamond surface may increase the minimum achievable distance between NV center and target spin and therefore reduce the coupling strength. Third, adsorbates can affect shallow NV centers by magnetic or electronic interactions; for example, charge transfer between the NV^- center and adsorbates may result in blinking in the NV fluorescence [194]. And fourth, background fluorescence from contaminations decreases the signal-to-noise ratio in the NV spin-state readout and thus reduces the sensitivity.

While atomically clean samples are routinely prepared in the field of UHV scanning probe microscopy by Ar-sputtering and annealing cycles, this treatment is obviously not suitable for diamond samples containing shallow NV centers. Nevertheless, annealing the samples under vacuum conditions to a sufficient temperature before the sample is transferred to the microscope head should remove a major part of the adsorbates. A first step into this direction was the integration of a simple resistive foil heater into the loadlock chamber which enabled heating the sample to roughly 130°C. However, tests did not show an improvement and revealed additional problems with contaminations arising presumably from the epoxy resin which increase at elevated temperature. To overcome this issue the sample holder design is currently revised to make it fully high temperature compatible by avoiding epoxy glue and the circuit board components. Furthermore an improved heating stage is developed which reaches higher temperatures (500-1000°C).

After cleaning, the second step in the *in-situ* sample preparation will be the controlled deposition of target molecules. For smaller molecules with sufficiently high vapor pressure, this can be achieved by thermal evaporation using the evaporator already mounted on the loadlock chamber. Other potential target systems, including large biomolecules like peptides and proteins as well as inorganic nanoparticles, can be deposited under UHV-conditions by electrospray ion beam deposition, for which there is a dedicated setup at our institute [195, 196]. Sample transfers between this machine and our system can be carried out without exposing the sample to air by using a so-called vacuum-suitcase, i.e. a small portable UHV-chamber which can be attached to both setups. This suitcase as well as the components necessary for the sample transfer at both machines are currently in the design phase and could be realized in the medium term.

If the *in-situ* sample preparation capabilities of the setup are extended as described

above, it will be useful to expand the vacuum system by a third chamber serving as fast-entry loadlock. The chamber currently serving as loadlock and preparation chamber could then be dedicated exclusively to the later task, which will facilitate maintaining UHV conditions in this section and therefore reduces the sample contamination.

6.2 Future Experiments

Chapter 5 demonstrated NV magnetic sensing of ferritin proteins, verifying that this approach outperforms established techniques like susceptibility measurements and Mößbauer spectroscopy in terms of measurement bandwidth and sensitivity. While the investigated ferritin molecules possessed a rather large magnetic moment on the order of 300 μ_B, the applied technique bears the potential to investigate target systems with much lower magnetic moment down to the nuclear spin level (see section 2.3). Working towards this goal, the next milestones will be the demonstration of single electron spin sensing and nuclear spin detection in molecular systems.

6.2.1 Single Spin ESR

With the current performance of the experimental apparatus (as demonstrated in section 4) and T_2 times of 10-20 μs for shallow NV centers in the available diamond samples, the currently achievable sensitivity should be sufficient for single electron spin detection in double resonance experiments. Thus, even without improving the system performance by the measures discussed above, the study of molecular systems like radicals or metal-organic compounds should be feasible. We currently explore different potential target species including the nitroxyl radical TEMPO (2,2,6,6-tetramethylpiperidinyloxy) [197], the radical PTM (polychlorotrimethylphenyl) [198] and copper phthalocyanine (CuPc) [23]. The target molecule is required to have an sufficiently long spin lifetime T_1 at low temperature, which should be longer than the coherence time of the NV center for sensitive double resonance experiments. Furthermore, the photophysical properties have to be considered. Since the laser intensity in the optical focus is on the order of 10^9 W/m^2, photo-induced reactions and photo-destruction is a severe problem for many molecular systems [199]. After depositing TEMPO or PTM on a diamond substrate, we observed an initially increased background fluorescence in combination with strong photobleaching, indicating that these molecules are indeed unstable in the excitation focus.

The above mentioned modifications of the experimental setup might help to overcome these limitations: an improved optical collection efficiency enables a lower excitation in-

tensity, while the lower photon energy used for resonant excitation of the NV center is expected to be less harmful for most molecules. Since the photo-induced reaction rate depend strongly on the chemical environment [199–201] and especially on the presence of oxygen [202], also an enhanced sample cleaning procedure might improve the photostability.

A stable molecular electron spin system would not only allow the demonstration of nanoscale single spin imaging, but also the investigation of its relaxation dynamics and its interaction with nearby nuclei. Furthermore it represents an intriguing model system to study mesoscopic quantum effects. One example is the observation of magnetization tunneling occurring in molecular spin systems with $S > 1/2$ and sufficient anisotropy barrier. Below the blocking temperature, the spin state can tunnel coherently between states with parallel or anti-parallel projections onto the anisotropy axis for certain values of the external magnetic field [203, 204]. This effect is usually studied by magnetization measurements on bulk samples, which yields only ensemble-averaged results and requires very low temperatures ($T < 4K$) due to the slow measurement. As demonstrated in section 5, NV magnetometry can probe spin dynamics at much faster timescales by appropriate sensing protocols, enabling the investigation of this effect in single molecules even at temperatures accessible in our setup.

6.2.2 Nanoscale NMR

The ultimate goal in nanoscale magnetometry is the detection of individual nuclear spins and therewith the ability to perform single spin NMR spectroscopy and imaging. Compared to the ESR experiments discussed in the previous section, such technique would be applicable to a much wider range of target systems, since most molecular systems host spin-bearing nuclei, while unpaired electron spins are relatively sparse. Furthermore, the photostability is of less concern due to the generally lower reactivity.

The detection of proton spins ensembles in organic molecules has recently been demonstrated with a sensitivity corresponding to $\sim 10^4$ protons in a $(5\text{nm})^3$ detection volume [14, 15]. To achieve a comparable sensitivity with our experimental setup, the current limitation due to the optical collection efficiency at low temperature has to be overcome, which could be realized by the measures discussed in 6.1.1. Further progress in the diamond synthesis and NV fabrication yielding longer coherence times for shallow NV centers would substantially enhance the sensing performance additionally.

While the recent experimental demonstrations relied on a static arrangement of NV sensor and target spins, our setup will enable a spatial mapping of the nuclear spin density by either scanning NV sensor and the target molecules with respect to each other,

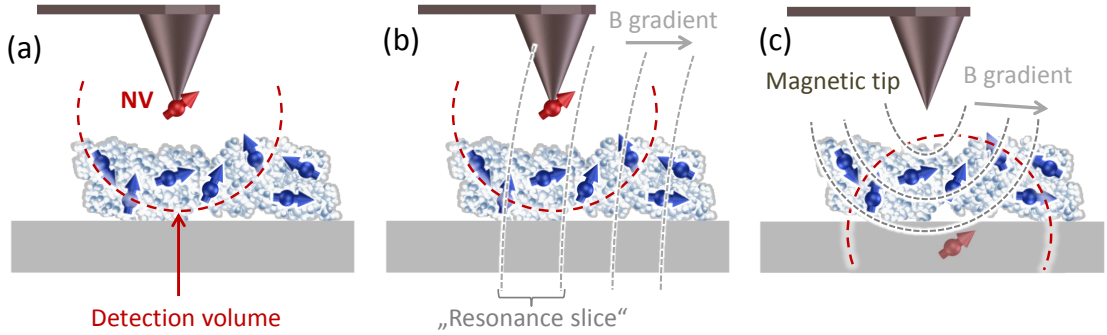

Figure 6.2: (a) Spin imaging in the scanning NV configuration; the spatial resolution is on the order of the sensor sample distance. Due to the high nuclear spin density in typical biomolecules, the detection of individual spins is precluded. (b) In the presence of a magnetic field gradient, only spins in a small region of the detection volume are precessing with a frequency within the detection bandwidth, resulting in a strongly enhanced spatial resolution. (c) The same principle can be realized with a stationary NV spin and a magnetic tip to create the field gradient.

or by employing the scanning field gradient technique (similar to the measurements in section 4.4). The different measurement configurations are depicted in figure 6.2. In the scanning NV configuration shown in (a), the spatial resolution is on the order of the sensor-sample distance and therewith limited to a few nanometer. This is sufficient to map the spin density within larger proteins with sizes above 10 nm and typical proton densities of $10^{22} - 10^{23}$ cm^{-3}. A substantially enhanced spatial resolution could be achieved by applying strong magnetic field gradients, which could be realized either by a magnetic tip or by magnetic nanostructures fabricated onto the sample. These two configurations are shown in 6.2 (b) and (c). The field gradient converts the high spectral resolution provided by dynamic decoupling protocols into a high spatial resolution, since nuclear spins in different locations have distinguishable precession frequencies (the same principle is used for tomography in clinical MRI machines). This results in a spatial resolution given by the detection bandwidth and the steepness of the field gradient. In MRFM experiments, gradients on the order of 10^6 T/m can be achieved by engineering magnetic nanostructures [205]; combined with an detection bandwidth of ~ 5 kHz for high order dynamic decoupling protocols, this yields a projected spatial resolution on the order of 0.1 nm [1]. Thus, three dimensional imaging and the spectroscopic investigation of individual nuclei within complex molecules might be feasible.

Appendix A

Abbreviations and Symbols

AFM	Atomic force microscopy
APD	Avalanche photodiode
AOM	Acousto-optical modulator
CPMG	Car-Purcell-Gill-Meiboom sequence
DD	Dynamic Decoupling
DEER	Double electron electron resonance
EPR	Electron paramagnetic resonance
ESR	Electron spin resonance
ESEEM	Electron spin echo envelope modulation
FID	Free induction decay
FPGA	Field programmable gate array
ISC	Inter-system crossing
LAC	Level anti-crossing
MRFM	Magnetic resonance force microscopy
MW	Microwave
NA	Numeric Aperture
NMR	Nuclear magnetic resonance
NV	Nitrogen vacancy center
ODMR	Optically detected magnetic resonance
PL	Photoluminescence
PSF	Point-spread function
RF	Radio frequency
SEDOR	Spin echo double resonance
SNR	Signal to noise ratio
SQUID	Superconducting quantum interference device

T_1	Longitudinal relaxation time
T_2	Transverse relaxation time
T_2^*	Decoherence Time
UHV	Ultra high vacuum
ZFS	Zero field splitting
ZPL	Zero phonon line

Appendix B

Acknowledgments

This project could not be realized without the contributions by various people, be it by scientific discussions, technical assistance or general support.

First of all I would like to express my gratitude to Prof. Klaus Kern and Prof. Jörg Wrachtrup for giving me the possibility to work in this joint project and to profit from the accumulated expertise and know-how in both research groups. I highly appreciate their continuous support throughout this project. I also thank Prof. Wunner for chairing the final exam.

My special thanks go to Markus Ternes and Friedemann Reinhard who supervised this project from the first designing stage to the final experiments and provided broad scientific and technical knowledge as well as a great deal of enthusiasm and optimism.

Wolfgang Stiepany contributed his expertise in the construction of low temperature UHV scanning probe setups, which was an invaluable help in the design and assembly stage of this project. I would like to thank furthermore Peter Andler, Andreas Koch and Marco Memmler for technical support on numerous occasions.

I highly appreciate the close collaboration with the former and current members of the diamond-AFM crew Marian Blankenhorn, Evangelos Fillis-Tsirakis, Lukas Schlipf and Tom White. Special thanks to Tom also for proofreading large parts of this manuscript.

I would like to thank all members of the department of Professor Kern at the Max Planck Institute as well as the members of Professor Wrachtrups group at the University of Stuttgart for the nice atmosphere and support in many respects. In particular I thank (in alphabetical order) Max Assig, Christian Dette, Rico Gutzler, Tobias Herden, Steffen Kahle, Christopher Kley, Sören Krotzky, Claudius Morchutt, Gordon Rinke, Daniel Rosenblatt, Carola Straßer and Benjamin Wurster for the great time we spent together at work, at conferences or at various non-scientific occasions... Tobias Staudacher,

Helmut Fedder, Matthias Niethammer and Rolf Reuter helped many times by preparing diamond samples, carrying out measurements or by technical suggestions.

During the construction and assembly of the experimental apparatus I profited from the excellent technical service groups at the Max-Planck Institut. My special thanks go to the technicians in the central workshop, who spend overall more than 1000 working hours for machining various components of the setup.

Finally I would like to thank my family for their unflagging support during all the years.

Bibliography

[1] J. M. Taylor, P. Cappellaro, L. Childress, L. Jiang, D. Budker, P. R. Hemmer, A. Yacoby, R. Walsworth, and M. D. Lukin, "High-sensitivity diamond magnetometer with nanoscale resolution," *Nature Physics*, vol. 4, pp. 810–816, Sept. 2008.

[2] B. M. Chernobrod and G. P. Berman, "Spin microscope based on optically detected magnetic resonance," *Journal of Applied Physics*, vol. 97, no. 1, p. 014903, 2005.

[3] C. L. Degen, "Scanning magnetic field microscope with a diamond single-spin sensor," *Applied Physics Letters*, vol. 92, no. 24, p. 243111, 2008.

[4] J. Cai, F. Jelezko, M. B. Plenio, and A. Retzker, "Diamond based single molecule magnetic resonance spectroscopy," *New Journal of Physics*, vol. 15, p. 11, Dec. 2013.

[5] V. S. Perunicic, L. T. Hall, D. A. Simpson, C. D. Hill, and L. C. L. Hollenberg, "Single molecule NMR detection and spectroscopy using single spins in diamond," *arXiv*, 2014.

[6] A. Schweiger and G. Jeschke, *Principles of pulse electron paramagnetic resonance*. Oxford University Press, 2005.

[7] M. H. Levitt, *Spin dynamics: basics of nuclear magnetic resonance*. John Wiley & Sons Ltd, 2nd ed., 2008.

[8] V. Acosta and P. Hemmer, "Nitrogen-vacancy centers: Physics and applications," *MRS Bulletin*, vol. 38, pp. 127–130, Feb. 2013.

[9] M. W. Doherty, N. B. Manson, P. Delaney, F. Jelezko, and L. C. L. Hollenberg, "The nitrogen-vacancy colour centre in diamond," *arXiv*, vol. 1302.3288v, pp. 1–101, 2013.

[10] S. Steinert, F. Ziem, L. T. Hall, A. Zappe, M. Schweikert, N. Götz, A. Aird, G. Balasubramanian, L. Hollenberg, and J. Wrachtrup, "Magnetic spin imaging under ambient conditions with sub-cellular resolution.," *Nature communications*, vol. 4, p. 1607, Jan. 2013.

[11] F. C. Ziem, N. S. Go, A. Zappe, and J. Wrachtrup, "Highly Sensitive Detection of Physiological Spins in a Micro fluidic Device," *Nano Letters*, vol. 13, pp. 4093–1098, 2013.

[12] B. Grotz, J. Beck, P. Neumann, B. Naydenov, R. Reuter, F. Reinhard, F. Jelezko, J. Wrachtrup, D. Schweinfurth, B. Sarkar, and P. Hemmer, "Sensing external spins with nitrogen-vacancy diamond," *New Journal of Physics*, vol. 13, p. 055004, May 2011.

[13] H. J. Mamin, M. H. Sherwood, and D. Rugar, "Detecting external electron spins using nitrogen-vacancy centers," *Physical Review B*, vol. 86, p. 195422, Nov. 2012.

[14] T. Staudacher, F. Shi, S. Pezzagna, J. Meijer, J. Du, C. A. Meriles, F. Reinhard, and J. Wrachtrup, "Nuclear magnetic resonance spectroscopy on a (5-nanometer)3 sample volume.," *Science*, vol. 339, pp. 561–3, Mar. 2013.

[15] H. J. Mamin, M. Kim, M. H. Sherwood, C. T. Rettner, K. Ohno, D. D. Awschalom, and D. Rugar, "Nanoscale nuclear magnetic resonance with a nitrogen-vacancy spin sensor.," *Science*, vol. 339, pp. 557–60, Mar. 2013.

[16] G. Balasubramanian, I. Y. Chan, R. Kolesov, M. Al-Hmoud, J. Tisler, C. Shin, C. Kim, A. Wojcik, P. R. Hemmer, A. Krueger, T. Hanke, A. Leitenstorfer, R. Bratschitsch, F. Jelezko, and J. Wrachtrup, "Nanoscale imaging magnetometry with diamond spins under ambient conditions.," *Nature*, vol. 455, pp. 648–51, Oct. 2008.

[17] L. Rondin, J.-P. Tetienne, P. Spinicelli, C. Dal Savio, K. Karrai, G. Dantelle, A. Thiaville, S. Rohart, J.-F. Roch, and V. Jacques, "Nanoscale magnetic field mapping with a single spin scanning probe magnetometer," *Applied Physics Letters*, vol. 100, no. 15, p. 153118, 2012.

[18] M. S. Grinolds, M. Warner, K. De Greve, Y. Dovzhenko, L. Thiel, R. L. Walsworth, S. Hong, P. Maletinsky, and A. Yacoby, "Subnanometre resolution in three-dimensional magnetic resonance imaging of individual dark spins," *Nature Nanotechnology*, pp. 1–6, Mar. 2014.

[19] E. R. Bauminger and L. Nowik, "Magnetism in ferritin," *Hyperfine interactions*, vol. 50, pp. 484–498, 1989.

[20] G. C. Papaefthymiou, "The Mössbauer and magnetic properties of ferritin cores.," *Biochimica et biophysica acta*, vol. 1800, pp. 886–97, Aug. 2010.

[21] D. E. Madsen, M. F. Hansen, J. Bendix, and S. Mø rup, "On the analysis of magnetization and Mössbauer data for ferritin.," *Nanotechnology*, vol. 19, p. 315712, Aug. 2008.

[22] E. Wajnberg, L. J. El-Jaick, M. P. Linhares, and D. M. Esquivel, "Ferromagnetic resonance of horse spleen ferritin: core blocking and surface ordering temperatures.," *Journal of magnetic resonance*, vol. 153, pp. 69–74, Nov. 2001.

[23] M. Warner, S. Din, I. S. Tupitsyn, G. W. Morley, A. M. Stoneham, J. A. Gardener, Z. Wu, A. J. Fisher, S. Heutz, C. W. M. Kay, and G. Aeppli, "Potential for spin-based information processing in a thin-film molecular semiconductor," *Nature*, vol. 503, pp. 504–508, Oct. 2013.

[24] S. A. Wolf, D. D. Awschalom, R. a. Buhrman, J. M. Daughton, S. von Molnár, M. L. Roukes, A. Y. Chtchelkanova, and D. M. Treger, "Spintronics: a spin-based electronics vision for the future.," *Science*, vol. 294, pp. 1488–95, Nov. 2001.

[25] I. Zutic, J. Fabian, and S. D. Sarma, "Spintronics : Fundamentals and applications," *Reviews of Modern Physics*, vol. 76, no. April, pp. 323–409, 2004.

[26] J. Fabian, A. Matos-Abiague, C. Ertler, P. Stano, and I. Zutic, "Semiconductor Spintronics," *arXiv*, vol. arXiv:0711, 2007.

[27] T. D. Ladd, F. Jelezko, R. Laflamme, Y. Nakamura, C. Monroe, and J. L. O'Brien, "Quantum computers," *Nature*, vol. 464, pp. 45–53, Mar. 2010.

[28] C. Kloeffel and D. Loss, "Prospects for Spin-Based Quantum Computing in Quantum Dots," *Annual Review of Condensed Matter Physics*, vol. 4, pp. 51–81, Apr. 2013.

[29] P. Glover and S. P. Mansfield, "Limits to magnetic resonance microscopy," *Reports on Progress in Physics*, vol. 65, pp. 1489–1511, Oct. 2002.

[30] H. Hopster and H. P. Oepen, eds., *Magnetic Microscopy of Nanostructures*. Springer-Verlag Berlin Heidelberg, 2005.

[31] C. Degen, "Microscopy with single spins," *Nature nanotechnology*, vol. 3, no. November, pp. 643–644, 2008.

[32] G. Boero, M. Demierre, P.-A. Besse, and R. Popovic, "Micro-Hall devices: performance, technologies and applications," *Sensors and Actuators A: Physical*, vol. 106, pp. 314–320, Sept. 2003.

[33] J. R. Kirtley, M. B. Ketchen, K. G. Stawiasz, J. Z. Sun, W. J. Gallagher, S. H. Blanton, and S. J. Wind, "High-resolution scanning SQUID microscope," *Applied Physics Letters*, vol. 66, no. 9, p. 1138, 1994.

[34] B. W. Gardner, J. C. Wynn, P. G. Björnsson, E. W. J. Straver, K. A. Moler, J. R. Kirtley, and M. B. Ketchen, "Scanning superconducting quantum interference device susceptometry," *Review of Scientific Instruments*, vol. 72, no. 5, p. 2361, 2001.

[35] M. E. Huber, N. C. Koshnick, H. Bluhm, L. J. Archuleta, T. Azua, P. G. Björnsson, B. W. Gardner, S. T. Halloran, E. A. Lucero, and K. A. Moler, "Gradiometric micro-SQUID susceptometer for scanning measurements of mesoscopic samples.," *The Review of scientific instruments*, vol. 79, p. 053704, May 2008.

[36] A. Finkler, Y. Segev, Y. Myasoedov, M. L. Rappaport, L. Ne'eman, D. Vasyukov, E. Zeldov, M. E. Huber, J. Martin, and A. Yacoby, "Self-aligned nanoscale SQUID on a tip.," *Nano letters*, vol. 10, pp. 1046–9, Mar. 2010.

[37] D. Vasyukov, Y. Anahory, L. Embon, D. Halbertal, J. Cuppens, L. Neeman, A. Finkler, Y. Segev, Y. Myasoedov, M. L. Rappaport, M. E. Huber, and E. Zeldov, "A scanning superconducting quantum interference device with single electron spin sensitivity.," *Nature nanotechnology*, vol. 8, pp. 639–44, Sept. 2013.

[38] H. Mamin, R. Budakian, B. Chui, and D. Rugar, "Detection and Manipulation of Statistical Polarization in Small Spin Ensembles," *Physical Review Letters*, vol. 91, p. 207604, Nov. 2003.

[39] D. Rugar, R. Budakian, H. J. Mamin, and B. W. Chui, "Single spin detection by magnetic resonance force microscopy.," *Nature*, vol. 430, pp. 329–32, July 2004.

[40] H. J. Mamin, T. H. Oosterkamp, M. Poggio, C. L. Degen, C. T. Rettner, and D. Rugar, "Isotope-selective detection and imaging of organic nanolayers.," *Nano letters*, vol. 9, pp. 3020–4, Aug. 2009.

[41] K. C. Fong, M. R. Herman, P. Banerjee, D. V. Pelekhov, and P. C. Hammel, "Spin lifetime in small ensembles of electron spins measured by magnetic resonance force microscopy," *Physical Review B*, vol. 84, p. 220405, Dec. 2011.

[42] B. K. Ofori-Okai, S. Pezzagna, K. Chang, M. Loretz, R. Schirhagl, Y. Tao, B. A. Moores, K. Groot-Berning, J. Meijer, and C. L. Degen, "Spin Properties of Very Shallow Nitrogen Vacancy Defects in Diamond," *Physical Review B*, vol. 86, Jan. 2012.

[43] M. S. Grinolds, S. Hong, P. Maletinsky, L. Luan, M. D. Lukin, R. L. Walsworth, and A. Yacoby, "Nanoscale magnetic imaging of a single electron spin under ambient conditions," *Nature Physics*, vol. 9, pp. 215–219, Sept. 2013.

[44] D. Drung, C. Aß mann, J. Beyer, A. Kirste, M. Peters, F. Ruede, and T. Schurig, "Highly Sensitive and Easy-to-Use SQUID Sensors," *IEEE Transcations on Applied Superconductivity*, vol. 17, no. 2, pp. 699–704, 2007.

[45] J. R. Kirtley and J. P. Wikswo, "Scanning SQUID Microscopy.," *Annual Review of Material Science*, vol. 29, pp. 117–148, May 1999.

[46] C. L. Degen, M. Poggio, H. J. Mamin, C. T. Rettner, and D. Rugar, "Nanoscale magnetic resonance imaging.," *Proceedings of the National Academy of Sciences of the United States of America*, vol. 106, pp. 1313–7, Feb. 2009.

[47] L. T. Hall, C. D. Hill, J. H. Cole, B. Städler, F. Caruso, P. Mulvaney, J. Wrachtrup, and L. C. L. Hollenberg, "Monitoring ion-channel function in real time through quantum decoherence.," *Proceedings of the National Academy of Sciences of the United States of America*, vol. 107, pp. 18777–82, Nov. 2010.

[48] J. Tisler, T. Oeckinghaus, R. J. Stöhr, R. Kolesov, R. Reuter, F. Reinhard, and J. Wrachtrup, "Single defect center scanning near-field optical microscopy on graphene.," *Nano letters*, vol. 13, p. 3965, Aug. 2013.

[49] P. Maletinsky, S. Hong, M. S. Grinolds, B. Hausmann, M. D. Lukin, R. L. Walsworth, M. Loncar, and a. Yacoby, "A robust scanning diamond sensor for nanoscale imaging with single nitrogen-vacancy centres.," *Nature nanotechnology*, vol. 7, pp. 320–4, May 2012.

[50] R. Sessoli, D. Gatteschi, A. Caneschi, and M. A. Novak, "Magnetic bistability in a metal-ion cluster," *Nature*, vol. 365, p. 141, 1993.

[51] H. Sato, S. E. Bottle, J. P. Blinco, A. S. Micallef, G. R. Eaton, and S. S. Eaton, "Electron spin-lattice relaxation of nitroxyl radicals in temperature ranges that span glassy solutions to low-viscosity liquids.," *Journal of magnetic resonance*, vol. 191, pp. 66–77, Mar. 2008.

[52] S. Morita, R. Wiesendanger, and E. Meyer, eds., *Noncontact Atomic Force Microscopy Vol.1.* Springer Verlag Berlin Heidelberg, 2002.

[53] L. Childress and R. Hanson, "Diamond NV centers for quantum computing and quantum networks," *MRS Bulletin*, vol. 38, pp. 134–138, Feb. 2013.

[54] S. Hong, M. S. Grinolds, L. M. Pham, D. Le Sage, L. Luan, R. L. Walsworth, and A. Yacoby, "Nanoscale magnetometry with NV centers in diamond," *MRS Bulletin*, vol. 38, pp. 155–161, Feb. 2013.

[55] Y. Mita, "Change of absorption spectra in type-Ib diamond with heavy neutron irradiation," *Physical Review B*, vol. 53, pp. 11360–11364, May 1996.

[56] M. V. Hauf, B. Grotz, B. Naydenov, M. Dankerl, S. Pezzagna, J. Meijer, F. Jelezko, J. Wrachtrup, M. Stutzmann, F. Reinhard, and J. A. Garrido, "Chemical control of the charge state of nitrogen-vacancy centers in diamond," *Physical Review B*, vol. 83, p. 081304, Feb. 2011.

[57] B. Grotz, M. V. Hauf, M. Dankerl, B. Naydenov, S. Pezzagna, J. Meijer, F. Jelezko, J. Wrachtrup, M. Stutzmann, F. Reinhard, and J. A. Garrido, "Charge state manipulation of qubits in diamond.," *Nature communications*, vol. 3, p. 729, Jan. 2012.

[58] N. Aslam, G. Waldherr, P. Neumann, F. Jelezko, and J. Wrachtrup, "Photo-induced ionization dynamics of the nitrogen vacancy defect in diamond investigated by single-shot charge state detection," *New Journal of Physics*, vol. 15, p. 013064, Jan. 2013.

[59] A. Lenef, S. C. Rand, and V. Wyk, "Electronic strucutre of the NV center in diamond: Theory," *Physical Review B*, vol. 53, no. 20, pp. 13441–13454, 1996.

[60] A. Gali, M. Fyta, and E. Kaxiras, "Ab initio supercell calculations on nitrogen-vacancy center in diamond: Electronic structure and hyperfine tensors," *Physical Review B*, vol. 77, p. 155206, Apr. 2008.

[61] J. R. Maze, A. Gali, E. Togan, Y. Chu, A. Trifonov, E. Kaxiras, and M. D. Lukin, "Properties of nitrogen-vacancy centers in diamond: the group theoretic approach," *New Journal of Physics*, vol. 13, p. 025025, Feb. 2011.

[62] M. W. Doherty, N. B. Manson, P. Delaney, and L. C. L. Hollenberg, "The negatively charged nitrogen-vacancy centre in diamond: the electronic solution," *New Journal of Physics*, vol. 13, p. 025019, Feb. 2011.

[63] M. W. Doherty, F. Dolde, H. Fedder, F. Jelezko, J. Wrachtrup, N. B. Manson, and L. C. L. Hollenberg, "Theory of the ground-state spin of the NV^- center in diamond," *Physical Review B*, vol. 85, p. 205203, May 2012.

[64] A. Batalov, V. Jacques, F. Kaiser, P. Siyushev, P. Neumann, L. Rogers, R. McMurtrie, N. Manson, F. Jelezko, and J. Wrachtrup, "Low Temperature Studies of the Excited-State Structure of Negatively Charged Nitrogen-Vacancy Color Centers in Diamond," *Physical Review Letters*, vol. 102, p. 195506, May 2009.

[65] a. Gali, T. Simon, and J. E. Lowther, "An ab initio study of local vibration modes of the nitrogen-vacancy center in diamond," *New Journal of Physics*, vol. 13, p. 025016, Feb. 2011.

[66] V. M. Acosta, *Optical Magnetometry with Nitrogen-Vacancy Centers in Diamond*. PhD thesis, University of California, Berkeley, 2011.

[67] P. Tamarat, N. B. Manson, J. P. Harrison, R. L. McMurtrie, a. Nizovtsev, C. Santori, R. G. Beausoleil, P. Neumann, T. Gaebel, F. Jelezko, P. Hemmer, and J. Wrachtrup, "Spin-flip and spin-conserving optical transitions of the nitrogen-vacancy centre in diamond," *New Journal of Physics*, vol. 10, p. 045004, Apr. 2008.

[68] E. Togan, Y. Chu, A. S. Trifonov, L. Jiang, J. Maze, L. Childress, M. V. G. Dutt, A. S. Sø rensen, P. R. Hemmer, A. S. Zibrov, and M. D. Lukin, "Quantum entanglement between an optical photon and a solid-state spin qubit.," *Nature*, vol. 466, pp. 730–4, Aug. 2010.

[69] C. G. Yale, B. B. Buckley, D. J. Christle, G. Burkard, F. J. Heremans, L. C. Bassettt, and D. D. Awschalom, "All-optical control of a solid-state spin using coherent dark states," *arXiv*, no. 1302.6638v2, 2013.

[70] L. J. Rogers, R. L. McMurtrie, M. J. Sellars, and N. B. Manson, "Time-averaging within the excited state of the nitrogen-vacancy centre in diamond," *New Journal of Physics*, vol. 11, p. 063007, June 2009.

[71] L. J. Rogers, S. Armstrong, M. J. Sellars, and N. B. Manson, "Infrared emission of the NV centre in diamond: Zeeman and uniaxial stress studies," *New Journal of Physics*, vol. 10, p. 103024, Oct. 2008.

[72] V. M. Acosta, A. Jarmola, L. J. Zipp, M. P. Ledbetter, E. Bauch, and D. Budker, "Broadband magnetometry by infrared-absorption detection of diamond NV centers and associated temperature dependence," *Proc. of SPIE*, vol. 7948, pp. 79480W–79480W–9, Feb. 2011.

[73] F. Jelezko and J. Wrachtrup, "Single defect centres in diamond: A review," *Physica Status Solidi (a)*, vol. 203, pp. 3207–3225, Oct. 2006.

[74] J. Harrison, M. Sellars, and N. Manson, "Measurement of the optically induced spin polarisation of N-V centres in diamond," *Diamond and Related Materials*, vol. 15, pp. 586–588, Apr. 2006.

[75] L. Robledo, H. Bernien, T. V. D. Sar, and R. Hanson, "Spin dynamics in the optical cycle of single nitrogen-vacancy centres in diamond," *New Journal of Physics*, vol. 13, p. 025013, Feb. 2011.

[76] P. Delaney, J. C. Greer, and J. A. Larsson, "Spin-polarization mechanisms of the nitrogen-vacancy center in diamond.," *Nano letters*, vol. 10, pp. 610–4, Feb. 2010.

[77] S. Felton, A. Edmonds, M. Newton, P. Martineau, D. Fisher, D. Twitchen, and J. Baker, "Hyperfine interaction in the ground state of the negatively charged nitrogen vacancy center in diamond," *Physical Review B*, vol. 79, p. 075203, Feb. 2009.

[78] X.-f. He, N. B. Manson, and P. T. H. Fisk, "Paramagnetic resonance of photoexcited N- V defects in diamond. I. Level anticrossing in the 3A ground state," *Physical Review B*, vol. 47, no. 14, pp. 8809–8815, 1993.

[79] J.-P. Tetienne, L. Rondin, P. Spinicelli, M. Chipaux, T. Debuisschert, J.-F. Roch, and V. Jacques, "Magnetic-field-dependent photodynamics of single NV defects in diamond: an application to qualitative all-optical magnetic imaging," *New Journal of Physics*, vol. 14, p. 103033, Oct. 2012.

[80] J. R. Rabeau, P. Reichart, G. Tamanyan, D. N. Jamieson, S. Prawer, F. Jelezko, T. Gaebel, I. Popa, M. Domhan, and J. Wrachtrup, "Implantation of labelled single nitrogen vacancy centers in diamond using ^{15}N," *Applied Physics Letters*, vol. 88, no. 2, p. 023113, 2006.

[81] D. A. Redman, S. Brown, S. R. H, and S. C. Rand, "Spin Dynamics and Electronic States of N-V Centers in Diamond by EPR and Four-Wave-Mixing Spectroscopy," *Physical Review Letters*, vol. 67, no. 24, pp. 3420–3423, 1991.

[82] S. Takahashi, R. Hanson, J. van Tol, M. Sherwin, and D. Awschalom, "Quenching Spin Decoherence in Diamond through Spin Bath Polarization," *Physical Review Letters*, vol. 101, p. 047601, July 2008.

[83] a. Jarmola, V. M. Acosta, K. Jensen, S. Chemerisov, and D. Budker, "Temperature- and Magnetic-Field-Dependent Longitudinal Spin Relaxation in Nitrogen-Vacancy Ensembles in Diamond," *Physical Review Letters*, vol. 108, p. 197601, May 2012.

[84] T. Yamamoto, T. Umeda, K. Watanabe, S. Onoda, M. L. Markham, D. J. Twitchen, B. Naydenov, L. P. McGuinness, T. Teraji, S. Koizumi, F. Dolde, H. Fedder, J. Honert, J. Wrachtrup, T. Ohshima, F. Jelezko, and J. Isoya, "Extending spin coherence times of diamond qubits by high-temperature annealing," *Physical Review B*, vol. 88, p. 075206, Aug. 2013.

[85] G. Balasubramanian, P. Neumann, D. Twitchen, M. Markham, R. Kolesov, N. Mizuochi, J. Isoya, J. Achard, J. Beck, J. Tissler, V. Jacques, P. R. Hemmer, F. Jelezko, and J. Wrachtrup, "Ultralong spin coherence time in isotopically engineered diamond.," *Nature materials*, vol. 8, pp. 383–7, May 2009.

[86] R. Hanson, V. V. Dobrovitski, A. E. Feiguin, O. Gywat, and D. D. Awschalom, "Coherent dynamics of a single spin interacting with an adjustable spin bath-Supplemental," *Science*, vol. 320, pp. 352–5, Apr. 2008.

[87] J. Tisler, G. Balasubramanian, B. Naydenov, R. Kolesov, B. Grotz, R. Reuter, J.-P. Boudou, P. a. Curmi, M. Sennour, A. Thorel, M. Börsch, K. Aulenbacher, R. Erdmann, P. R. Hemmer, F. Jelezko, and J. Wrachtrup, "Fluorescence and spin properties of defects in single digit nanodiamonds.," *ACS nano*, vol. 3, pp. 1959–65, July 2009.

[88] A. Laraoui, J. S. Hodges, and C. A. Meriles, "Nitrogen-Vacancy-Assisted Magnetometry of Paramagnetic Centers in an Individual Diamond Nanocrystal," *Nano Letters*, vol. 12, pp. 3477–3482, 2012.

[89] L. P. McGuinness, L. T. Hall, A. Stacey, D. A. Simpson, C. D. Hill, J. H. Cole, K. Ganesan, B. C. Gibson, S. Prawer, P. Mulvaney, F. Jelezko, J. Wrachtrup, R. E. Scholten, and L. C. L. Hollenberg, "Ambient nanoscale sensing with single spins using quantum decoherence," *New Journal of Physics*, vol. 15, p. 073042, July 2013.

[90] A. Tallaire, A. Collins, D. Charles, J. Achard, R. Sussmann, A. Gicquel, M. Newton, A. Edmonds, and R. Cruddace, "Characterisation of high-quality thick single-crystal diamond grown by CVD with a low nitrogen addition," *Diamond and Related Materials*, vol. 15, pp. 1700–1707, Oct. 2006.

[91] B. Naydenov, V. Richter, J. Beck, M. Steiner, P. Neumann, G. Balasubramanian, J. Achard, F. Jelezko, J. Wrachtrup, and R. Kalish, "Enhanced generation of single optically active spins in diamond by ion implantation," *Applied Physics Letters*, vol. 96, no. 16, p. 163108, 2010.

[92] S. Pezzagna, B. Naydenov, F. Jelezko, J. Wrachtrup, and J. Meijer, "Creation efficiency of nitrogen-vacancy centres in diamond," *New Journal of Physics*, vol. 12, p. 065017, June 2010.

[93] K. Ohno, F. Joseph Heremans, L. C. Bassett, B. a. Myers, D. M. Toyli, A. C. Bleszynski Jayich, C. J. Palmstrø m, and D. D. Awschalom, "Engineering shallow spins in diamond with nitrogen delta-doping," *Applied Physics Letters*, vol. 101, no. 8, p. 082413, 2012.

[94] A. Stacey, D. A. Simpson, T. J. Karle, B. C. Gibson, V. M. Acosta, Z. Huang, K. M. C. Fu, C. Santori, R. G. Beausoleil, L. P. McGuinness, K. Ganesan, S. Tomljenovic-Hanic, A. D. Greentree, and S. Prawer, "Near-surface spectrally stable nitrogen vacancy centres engineered in single crystal diamond.," *Advanced materials*, vol. 24, pp. 3333–8, July 2012.

[95] J. Schwartz, P. Michaelides, C. D. Weis, and T. Schenkel, "In situ optimization of co-implantation and substrate temperature conditions for nitrogen-vacancy center formation in single-crystal diamonds," *New Journal of Physics*, vol. 13, p. 035022, Mar. 2011.

[96] K. Ohashi, T. Rosskopf, H. Watanabe, M. Loretz, Y. Tao, R. Hauert, S. Tomizawa, T. Ishikawa, S. Shikata, C. L. Degen, and K. M. Itoh, "Negatively Charged Nitrogen-Vacancy Centers in a 5 nm Thin C12 Diamond Film," *Nano letters*, vol. 13, pp. 4733–4738, 2013.

[97] a. Dréau, M. Lesik, L. Rondin, P. Spinicelli, O. Arcizet, J.-F. Roch, and V. Jacques, "Avoiding power broadening in optically detected magnetic resonance of single NV defects for enhanced dc magnetic field sensitivity," *Physical Review B*, vol. 84, p. 195204, Nov. 2011.

[98] M. Steiner, P. Neumann, J. Beck, F. Jelezko, and J. Wrachtrup, "Universal enhancement of the optical readout fidelity of single electron spins at nitrogen-vacancy centers in diamond," *Physical Review B*, vol. 81, p. 035205, Jan. 2010.

[99] P. Neumann, *Towards a room temperature solid-state quantum processor - The nitrogen-vacancy center in diamond*. PhD thesis, University of Stuttgart, 2012.

[100] G.-Q. Liu, X.-Y. Pan, Z.-F. Jiang, N. Zhao, and R.-B. Liu, "Controllable effects of quantum fluctuations on spin free-induction decay at room temperature.," *Scientific reports*, vol. 2, p. 432, Jan. 2012.

[101] J. R. Maze, A. Dréau, V. Waselowski, H. Duarte, J.-F. Roch, and V. Jacques, "Free induction decay of single spins in diamond," *arXiv*, vol. 1206.4575v, 2012.

[102] L. Childress, M. V. Gurudev Dutt, J. M. Taylor, A. S. Zibrov, F. Jelezko, J. Wrachtrup, P. R. Hemmer, and M. D. Lukin, "Coherent dynamics of coupled electron and nuclear spin qubits in diamond.," *Science*, vol. 314, pp. 281–5, Oct. 2006.

[103] L. T. Hall, C. D. Hill, J. H. Cole, and L. C. L. Hollenberg, "Ultrasensitive diamond magnetometry using optimal dynamic decoupling," *Physical Review B*, vol. 82, p. 045208, July 2010.

[104] G. de Lange, Z. H. Wang, D. Ristè, V. V. Dobrovitski, and R. Hanson, "Universal dynamical decoupling of a single solid-state spin from a spin bath.," *Science*, vol. 330, pp. 60–3, Oct. 2010.

[105] L. M. Pham, N. Bar-Gill, C. Belthangady, D. Le Sage, P. Cappellaro, M. D. Lukin, a. Yacoby, and R. L. Walsworth, "Enhanced solid-state multispin metrology using dynamical decoupling," *Physical Review B*, vol. 86, p. 045214, July 2012.

[106] Z. H. Wang, G. de Lange, D. Ristè, R. Hanson, and V. V. Dobrovitski, "Comparison of dynamical decoupling protocols for a nitrogen-vacancy center in diamond," *arXiv*, vol. 1202.0462v, pp. 1–16, 2012.

[107] L. Cywiński, R. Lutchyn, C. Nave, and S. Das Sarma, "How to enhance dephasing time in superconducting qubits," *Physical Review B*, vol. 77, p. 174509, May 2008.

[108] F. Rempp, *Decoherence properties of the NV-center in diamond*. PhD thesis, Universität Stuttgart, 2011.

[109] N. Bar-Gill, L. M. Pham, C. Belthangady, D. Le Sage, P. Cappellaro, J. R. Maze, M. D. Lukin, A. Yacoby, and R. Walsworth, "Suppression of spin-bath dynamics for improved coherence of multi-spin-qubit systems.," *Nature communications*, vol. 3, p. 858, Jan. 2012.

[110] Z.-H. Wang and S. Takahashi, "Spin decoherence and electron spin bath noise of a nitrogen-vacancy center in diamond," *Physical Review B*, vol. 87, p. 115122, Mar. 2013.

[111] T. Gullion, S. Louis, and D. B. Baker, "New, Compensated Carr-Purcell Sequences," *Journal of Magnetic Resonance*, vol. 484, pp. 479–484, 1990.

[112] B. Naydenov, F. Dolde, L. T. Hall, C. Shin, H. Fedder, L. C. L. Hollenberg, F. Jelezko, and J. Wrachtrup, "Dynamical decoupling of a single-electron spin at room temperature," *Physical Review B*, vol. 83, p. 081201, Feb. 2011.

[113] R. D. Sousa, "Electron Spin as a Spectrometer of Nuclear-Spin Noise and Other Fluctuations," in *Electron Spin Resonance and Related Phenomena in Low-Dimensional Structures* (M. Fanciulli, ed.), vol. 220, pp. 183–220, Springer Verlag Berlin Heidelberg, 2009.

[114] J. R. Klauder and P. W. Anderson, "Spectral Diffusion in Spin Resonance Experiments," *Physical Review*, vol. 125, no. 3, pp. 912–932, 1962.

[115] A. Ermakova, G. Pramanik, U. Kaiser, T. Weil, H. C. Chang, L. P. Mcguinness, M. B. Plenio, B. Naydenov, and F. Jelezko, "Detection of a Few Metallo-Protein Molecules Using Color Centers in Nanodiamonds," *Nano Letters*, 2013.

[116] J.-P. Tetienne, T. Hingant, L. Rondin, a. Cavaillès, L. Mayer, G. Dantelle, T. Gacoin, J. Wrachtrup, J.-F. Roch, and V. Jacques, "Spin relaxometry of single nitrogen-vacancy defects in diamond nanocrystals for magnetic noise sensing," *Physical Review B*, vol. 87, p. 235436, June 2013.

[117] T. Rosskopf, A. Dussaux, K. Ohashi, M. Loretz, R. Schirhagl, H. Watanabe, S. Shikata, K. M. Itoh, and C. L. Degen, "On the surface paramagnetism of diamond," *arXiv*, vol. 1, p. 6, Nov. 2013.

[118] D. Budker and M. Romalis, "Optical magnetometry," *nature physics*, vol. 3, pp. 227–234, 2007.

[119] S. Kotler, N. Akerman, Y. Glickman, A. Keselman, and R. Ozeri, "Single-ion quantum lock-in amplifier.," *Nature*, vol. 473, pp. 61–5, May 2011.

[120] N. Zhao, J. Honert, B. Schmid, M. Klas, J. Isoya, M. Markham, D. Twitchen, F. Jelezko, R.-B. Liu, H. Fedder, and J. Wrachtrup, "Sensing single remote nuclear spins.," *Nature nanotechnology*, vol. 7, pp. 657–62, Oct. 2012.

[121] F. Shi, Q. Zhang, B. Naydenov, F. Jelezko, J. Du, F. Reinhard, and J. Wrachtrup, "Quantum logic readout and cooling of a single dark electron spin," *Physical Review B*, vol. 87, p. 195414, May 2013.

[122] M. Loretz, T. Rosskopf, and C. L. Degen, "Radio-frequency magnetometry using a single electron spin," *arXiv*, vol. 1210.1443v, pp. 2–5, 2012.

[123] R. Kassies, K. O. van der Werf, a. Lenferink, C. N. Hunter, J. D. Olsen, V. Subramaniam, and C. Otto, "Combined AFM and confocal fluorescence microscope for applications in bio-nanotechnology.," *Journal of microscopy*, vol. 217, pp. 109–16, Jan. 2005.

[124] A. W. Schell, G. Kewes, T. Schröder, J. Wolters, T. Aichele, and O. Benson, "A scanning probe-based pick-and-place procedure for assembly of integrated quantum optical hybrid devices.," *The Review of scientific instruments*, vol. 82, p. 073709, July 2011.

[125] M. Lucas and E. Riedo, "Invited review article: combining scanning probe microscopy with optical spectroscopy for applications in biology and materials science.," *The Review of scientific instruments*, vol. 83, p. 061101, June 2012.

[126] Nanonics Imaging Ltd., "CryoView 2000."

[127] P. M. Anger, *Entwicklung eines optischen Tieftemperatur-Raster-Nahfeld-Mikroskops*. PhD thesis, Universität Siegen, 2003.

[128] I. Gerhardt, *Scattering & Absorption of Light by a Single Molecule under a Sub-wavelength Aperture*. PhD thesis, ETH Zuerich, 2006.

[129] J. Lee, J. Chae, C. K. Kim, H. Kim, S. Oh, and Y. Kuk, "Versatile low-temperature atomic force microscope with in situ piezomotor controls, charge-coupled device vision, and tip-gated transport measurement capability," *Review of Scientific Instruments*, vol. 76, no. 9, p. 093701, 2005.

[130] P. Siyushev, V. Jacques, I. Aharonovich, F. Kaiser, T. Müller, L. Lombez, M. Atatüre, S. Castelletto, S. Prawer, F. Jelezko, and J. Wrachtrup, "Low-temperature optical characterization of a near-infrared single-photon emitter in nanodiamonds," *New Journal of Physics*, vol. 11, p. 113029, Nov. 2009.

[131] Y. Seo and W. Jhe, "Atomic force microscopy and spectroscopy," *Reports on Progress in Physics*, vol. 71, p. 016101, Jan. 2008.

[132] F. J. Giessibl, S. Hembacher, M. Herz, C. Schiller, and J. Mannhart, "Stability considerations and implementation of cantilevers allowing dynamic force microscopy with optimal resolution: the qPlus sensor," *Nanotechnology*, vol. 15, pp. S79–S86, Feb. 2004.

[133] R. Webb, "Confocal optical microscopy," *Reports on Progress in Physics*, vol. 59, pp. 427–471, 1996.

[134] F. J. Giessibl, "AFM ' s path to atomic resolution," *Materials today*, no. May, pp. 32–41, 2005.

[135] F. Giessibl, "Forces and frequency shifts in atomic-resolution dynamic-force microscopy," *Physical Review B*, vol. 56, no. 24, pp. 16010–16015, 1997.

[136] R. García and R. Perez, "Dynamic atomic force microscopy methods," *Surface Science Reports*, vol. 47, no. 6-8, pp. 197–301, 2002.

[137] S. Morita, F. Giessibl, and R. Wiesendanger, eds., *Noncontact Atomic Force Microscopy Vol.2*. Springer-Verlag Berlin Heidelberg, 2009.

[138] N. J. Watkins, J. P. Long, Z. H. Kafafi, and A. J. Mäkinen, "Fiber optic light collection system for scanning-tunneling-microscope-induced light emission.," *The Review of scientific instruments*, vol. 78, p. 053707, May 2007.

[139] J. G. Keizer, J. K. Garleff, and P. M. Koenraad, "Simple and efficient scanning tunneling luminescence detection at low-temperature.," *The Review of scientific instruments*, vol. 80, p. 123704, Dec. 2009.

[140] K. Kuhnke, A. Kabakchiev, W. Stiepany, F. Zinser, R. Vogelgesang, and K. Kern, "Versatile optical access to the tunnel gap in a low-temperature scanning tunneling microscope.," *The Review of scientific instruments*, vol. 81, p. 113102, Nov. 2010.

[141] G. Wrigge, *Coherent and Incoherent Light Scattering in the Resonance Fluorescence of a Single Molecule*. PhD thesis, ETH Zurich, 2008.

[142] S. Hoppe, G. Ctistis, J. J. Paggel, and P. Fumagalli, "Reflection scanning near-field optical microscopy in ultrahigh vacuum," *Review of Scientific Instruments*, vol. 76, no. 6, p. 063704, 2005.

[143] J. Steidtner and B. Pettinger, "High-resolution microscope for tip-enhanced optical processes in ultrahigh vacuum.," *The Review of scientific instruments*, vol. 78, p. 103104, Oct. 2007.

[144] M. A. Lieb, *Mikroskopie mit Parabolspiegeloptik*. PhD thesis, Universität Siegen, 2001.

[145] J. Ekin, *Experimental Techniques for Low-Temperature Measurements*. Oxford University Press, 2006.

[146] R. M. Waxler and G. W. Cleek, "Refractive indices of fused silica at low temperatures," *Journal of Rearch of the National Bureau of Standards*, vol. 75A, no. 4, pp. 279–281, 1971.

[147] R. Juskaitis, "Characterizing High Numerical Aperture Microscope Objective," in *Optical Imaging and Microscopy*, pp. 21–43, Springer, 2007.

[148] R. E. Fischer, B. Tadic-Galeb, and P. R. Yoder, *Optical System Design*. McGraw-Hill Companies, Inc., 2008.

[149] J. Stadler, C. Stanciu, C. Stupperich, and A. J. Meixner, "Tighter focusing with a parabolic mirror.," *Optics letters*, vol. 33, pp. 681–3, Apr. 2008.

[150] A. Drechsler, M. Lieb, C. Debus, a. Meixner, and G. Tarrach, "Confocal microscopy with a high numerical aperture parabolic mirror.," *Optics express*, vol. 9, pp. 637–44, Dec. 2001.

[151] M. Lieb and A. Meixner, "A high numerical aperture parabolic mirror as imaging device for confocal microscopy.," *Optics express*, vol. 8, pp. 458–74, Mar. 2001.

[152] G. Leuchs, K. Mantel, A. Berger, H. Konermann, M. Sondermann, U. Peschel, N. Lindlein, and J. Schwider, "Interferometric null test of a deep parabolic reflector generating a Hertzian dipole field.," *Applied optics*, vol. 47, pp. 5570–84, Oct. 2008.

[153] C. R. Ast, M. Assig, A. Ast, and K. Kern, "Design criteria for scanning tunneling microscopes to reduce the response to external mechanical disturbances.," *The Review of scientific instruments*, vol. 79, p. 093704, Sept. 2008.

[154] Deutsches Kupferinstitut e.V., "Werkstoff-Datenblatt CW453K," 2013.

[155] T. Herden, *Design and Construction of a Q-Sensor AFM/STM for Low Temperatures*. PhD thesis, University of Constance, 2010.

[156] Präzisions Glas & Optik GmbH, "Datasheet macor ceramic," 2013.

[157] PI Ceramic GmbH, "Datasheet Piezoceramic Materials," 2013.

[158] EBL Products Inc, "Datasheet PZT ceramics," 2013.

[159] W. Haynes, "Handbook of Chemistry and Physics," 2013.

[160] G. Mariotto, M. D. Angelo, and I. V. Shvets, "Dynamic behavior of a piezowalker , inertial and frictional configurations," *Review of Scientific Instruments*, vol. 70, no. September, pp. 3651–3655, 1999.

[161] C. Debus, M. A. Lieb, A. Drechsler, and A. J. Meixner, "Probing highly confined optical fields in the focal region of a high NA parabolic mirror with subwavelength spatial resolution.," *Journal of microscopy*, vol. 210, pp. 203–8, June 2003.

[162] F. Grazioso, B. R. Patton, and J. M. Smith, "A high stability beam-scanning confocal optical microscope for low temperature operation.," *The Review of scientific instruments*, vol. 81, p. 093705, Sept. 2010.

[163] F. Jelezko, T. Gaebel, I. Popa, A. Gruber, and J. Wrachtrup, "Observation of Coherent Oscillations in a Single Electron Spin," *Physical Review Letters*, vol. 92, p. 076401, Feb. 2004.

[164] W. B. Mims, "Envelope Modulation in Spin-Echo Experiments," *Physical Review B*, vol. 5, no. 7, pp. 2409–2419, 1972.

[165] G. de Lange, T. van der Sar, M. Blok, Z.-H. Wang, V. Dobrovitski, and R. Hanson, "Controlling the quantum dynamics of a mesoscopic spin bath in diamond.," *Scientific reports*, vol. 2, p. 382, Jan. 2012.

[166] T. Akiyama, N. F. de Rooij, U. Staufer, M. Detterbeck, D. Braendlin, S. Waldmeier, and M. Scheidiger, "Implementation and characterization of a quartz tuning fork based probe consisted of discrete resonators for dynamic mode atomic force microscopy," *The Review of scientific instruments*, vol. 81, p. 063706, June 2010.

[167] W. Haiss, D. Lackey, J. K. Sass, and K. H. Besocke, "Atomic resolution scanning tunneling microscopy images of Au(111) surfaces in air and polar organic solvents," *The Journal of Chemical Physics*, vol. 95, no. 3, p. 2193, 1991.

[168] K. Uosaki, Y. Shen, and T. Kondo, "Preparation of a Highly Ordered Au (111) Phase on a Polycrystalline Gold Substrate by Vacuum Deposition and Its Characterization by XRD, GISXRD, STWAFM, and Electrochemical Measurements," *Journal of Physical Chemistry*, vol. 99, pp. 14117–14122, 1995.

[169] M. S. Grinolds, P. Maletinsky, S. Hong, M. D. Lukin, R. L. Walsworth, and A. Yacoby, "Quantum control of proximal spins using nanoscale magnetic resonance imaging," *Nature Physics*, vol. 7, pp. 687–692, May 2011.

[170] W. Wall, J. Karpick, and B. Bartole, "Temperature dependence of the vibronic spectrum and fluorescence lifetime of YAG: Cr3+," *Journal of Physics C: Solid State Physics*, vol. 4, p. 3258, 1971.

[171] M. Marceddu, M. Manca, P. C. Ricci, and A. Anedda, "The temperature dependence of Cr3+:YAG zero-phonon lines.," *Journal of physics. Condensed matter : an Institute of Physics journal*, vol. 24, p. 135401, Apr. 2012.

[172] J. He and D. R. Clarke, "Polarization Dependence of the Cr 3 + R-Line Fluorescence from Sapphire and Its Application to Crystal Orientation and Piezospectroscopic Measurement," *Journal of the American Ceramic Society*, vol. 80, no. 1, pp. 69–78, 1997.

[173] R. B. Frankel, G. C. Papaefthymiou, and G. D. Watt, "Variation of superparamagnetic properties with iron loading in mammalian ferritin," *Hyperfine interactions*, vol. 66, pp. 71–82, 1991.

[174] J. G. E. Harris, J. E. Grimaldi, D. D. Awschalom, A. Chiolero, and D. Loss, "Excess Spin and the Dynamics of Antiferromagnetic Ferritin," *arXiv*, vol. 2, no. 1, pp. 1–4, 2008.

[175] S. Gider, D. D. Awschalom, T. Douglas, S. Mann, and M. Chaparala, "Classical and quantum magnetic phenomena in natural and artificial ferritin proteins.," *Science*, vol. 268, pp. 77–80, Apr. 1995.

[176] S. H. Kilcoyne and R. Cywinski, "Ferritin : a model superparamagnet," *Journal of Magnetism and Magnetic Materials*, vol. 144, pp. 1466–1467, 1995.

[177] M. C. Linder, "Mobilization of stored iron in mammals: a review.," *Nutrients*, vol. 5, pp. 4022–50, Oct. 2013.

[178] M. Uchida, S. Kang, C. Reichhardt, K. Harlen, and T. Douglas, "The ferritin superfamily: Supramolecular templates for materials synthesis.," *Biochimica et biophysica acta*, vol. 1800, pp. 834–45, Aug. 2010.

[179] C. Gilles, P. Bonville, H. Rakoto, J. Broto, K. Wong, and S. Mann, "Magnetic hysteresis and superantiferromagnetism in ferritin nanoparticles," *Journal of Magnetism and Magnetic Materials*, vol. 241, pp. 430–440, Mar. 2002.

[180] W. F. Brown, "Thermal Fluctuations of a Single-Domain Particle," *Physical Review*, vol. 130, no. 5, 1963.

[181] J. L. Dormann, L. D. Chimie, D. Matiere, U. Pierre, and P. Jussieu, " Magnetic relaxation in fine particle systems," in *Advances in Chemical Physics XCVIII*, vol. XCVIII, pp. 283–494, 1997.

[182] S. Mø rup, D. E. Madsen, C. Frandsen, C. R. H. Bahl, and M. F. Hansen, "Experimental and theoretical studies of nanoparticles of antiferromagnetic materials," *Journal of Physics: Condensed Matter*, vol. 19, p. 213202, May 2007.

[183] D. P. E. Dickson, N. M. K. Reid, C. Hunt, H. D. Williams, M. El-Hilo, and K. O Grady, "Determination of f0 for fine magnetic particles," *Journal of Magnetism and Magnetic Materials*, vol. 125, pp. 345–350, 1993.

[184] V. M. Acosta, E. Bauch, M. P. Ledbetter, a. Waxman, L.-S. Bouchard, and D. Budker, "Temperature Dependence of the Nitrogen-Vacancy Magnetic Resonance in Diamond," *Physical Review Letters*, vol. 104, p. 070801, Feb. 2010.

[185] P. F. Vohralik and S. K. H. Lam, "NanoSQUID detection of magnetization from ferritin nanoparticles," *Superconductor Science and Technology*, vol. 22, p. 064007, June 2009.

[186] R. A. Brooks, J. Vymazal, R. B. Goldfarb, J. W. M. Bulte, and P. Aisen, "Relaxometry and Magnetometry of Ferritin," *Magn. Reson. Med.*, vol. 40, no. 2, p. 227, 1998.

[187] K. Beha, H. Fedder, M. Wolfer, M. C. Becker, P. Siyushev, M. Jamali, A. Batalov, C. Hinz, J. Hees, L. Kirste, H. Obloh, E. Gheeraert, B. Naydenov, I. Jakobi, F. Dolde, S. Pezzagna, D. Twittchen, M. Markham, D. Dregely, H. Giessen, J. Meijer, F. Jelezko, C. E. Nebel, R. Bratschitsch, A. Leitenstorfer, and J. Wrachtrup, "Diamond nanophotonics.," *Beilstein journal of nanotechnology*, vol. 3, pp. 895–908, Jan. 2012.

[188] B. J. Hausmann, M. Khan, Y. Zhang, T. M. Babinec, K. Martinick, M. McCutcheon, P. R. Hemmer, and M. Lončar, "Fabrication of diamond nanowires for quantum information processing applications," *Diamond and Related Materials*, vol. 19, pp. 621–629, May 2010.

[189] L. Robledo, L. Childress, H. Bernien, B. Hensen, P. F. a. Alkemade, and R. Hanson, "High-fidelity projective read-out of a solid-state spin quantum register.," *Nature*, vol. 477, pp. 574–8, Sept. 2011.

[190] P. Siyushev, F. Kaiser, V. Jacques, I. Gerhardt, S. Bischof, H. Fedder, J. Dodson, M. Markham, D. Twitchen, F. Jelezko, and J. Wrachtrup, "Monolithic diamond optics for single photon detection.," *Applied physics letters*, vol. 97, p. 241902, Dec. 2010.

[191] J. P. Hadden, J. P. Harrison, A. C. Stanley-Clarke, L. Marseglia, Y.-L. D. Ho, B. R. Patton, J. L. O'Brien, and J. G. Rarity, "Strongly enhanced photon collection from diamond defect centers under microfabricated integrated solid immersion lenses," *Applied Physics Letters*, vol. 97, no. 24, p. 241901, 2010.

[192] L. Marseglia, J. P. Hadden, A. C. Stanley-Clarke, J. P. Harrison, B. Patton, Y.-L. D. Ho, B. Naydenov, F. Jelezko, J. Meijer, P. R. Dolan, J. M. Smith, J. G. Rarity, and J. L. O'Brien, "Nanofabricated solid immersion lenses registered to single emitters in diamond," *Applied Physics Letters*, vol. 98, no. 13, p. 133107, 2011.

[193] T. M. Babinec, B. J. M. Hausmann, M. Khan, Y. Zhang, J. R. Maze, P. R. Hemmer, and M. Loncar, "A diamond nanowire single-photon source.," *Nature nanotechnology*, vol. 5, pp. 195–9, Mar. 2010.

[194] C. Bradac, T. Gaebel, N. Naidoo, M. J. Sellars, J. Twamley, L. J. Brown, A. S. Barnard, T. Plakhotnik, A. V. Zvyagin, and J. R. Rabeau, "Observation and control of blinking nitrogen-vacancy centres in discrete nanodiamonds.," *Nature nanotechnology*, vol. 5, pp. 345–9, May 2010.

[195] S. Rauschenbach, F. L. Stadler, E. Lunedei, N. Malinowski, S. Koltsov, G. Costantini, and K. Kern, "Electrospray ion beam deposition of clusters and biomolecules.," *Small*, vol. 2, pp. 540–7, Apr. 2006.

[196] S. Rauschenbach, R. Vogelgesang, N. Malinowski, J. W. Gerlach, M. Benyoucef, G. Costantini, Z. Deng, N. Thontasen, and K. Kern, "Electrospray ion beam deposition: soft-landing and fragmentation of functional molecules at solid surfaces.," *ACS nano*, vol. 3, pp. 2901–10, Oct. 2009.

[197] J. F. W. Keana, "Newer Aspects of the Synthesis and Chemistry of Nitroxide Spin Labels," *Chemical Reviews*, vol. 78, no. 1, pp. 37–64, 1978.

[198] M. Ballester, J. Riera, J. Castatier, C. Badfa, and J. M. Monsó, "Inert Carbon Free Radicals. I. Perchlorotriphenylmethyl and Perchlorotriphenylmethyl Radical Series," *Journal of the American Chemical Society*, vol. 93, no. 9, pp. 2215–2225, 1971.

[199] L. A. Deschenes and D. A. Vanden Bout, "Single molecule photobleaching : increasing photon yield and survival time through suppression of two-step photolysis," *Chemical Physics Letters*, vol. 365, pp. 387–395, 2002.

[200] J. Widengren and R. Rigler, "Mechanisms of photobleaching investigated by fluorescence correlation spectroscopy," *Bioimaging*, vol. 4, pp. 149–157, Sept. 1996.

[201] R. Zondervan, F. Kulzer, M. a. Kol'chenk, and M. Orrit, "Photobleaching of Rhodamine 6G in Poly(vinyl alcohol) at the Ensemble and Single-Molecule Levels," *The Journal of Physical Chemistry A*, vol. 108, pp. 1657–1665, Mar. 2004.

[202] Y. Lill and B. Hecht, "Single dye molecules in an oxygen-depleted environment as photostable organic triggered single-photon sources," *Applied Physics Letters*, vol. 84, no. 10, p. 1665, 2004.

[203] L. Thomas, F. Lionti, R. Ballou, D. Gatteschi, R. Sessoli, and B. Barbara, "Macroscopic quantum tunnelling of magnetization in a single crystal nanomagnet," *Nature*, vol. 383, pp. 145–147, 1996.

[204] J. Friedman, M. Sarachik, J. Tejada, and R. Ziolo, "Macroscopic measurement of resonant magnetization tunneling in high-spin molecules.," *Physical review letters*, vol. 76, pp. 3830–3833, May 1996.

[205] M. Poggio and C. L. Degen, "Force-detected nuclear magnetic resonance: recent advances and future challenges.," *Nanotechnology*, vol. 21, p. 342001, Aug. 2010.